UNIVERSITÉ LAVAL

A quality control tool for HDR prostate brachytherapy based on patient-specific geometry and stochastic frontier analysis

Mémoire

Reza Moosavi Askari

Maîtrise en physique - avec mémoire
Maître ès sciences (M. Sc.)

Québec, Canada

© Reza Moosavi Askari, 2019

A quality control tool for HDR prostate brachytherapy based on patient-specific geometry and stochastic frontier analysis

Mémoire

Reza Moosavi Askari

Sous la direction de:

Luc Beaulieu, directeur de recherche
Louis Archambault, codirecteur de recherche
Éric Poulin, codirecteur de recherche

Résumé

Cette étude porte sur le développement d'un outil de contrôle qualité basé sur l'expérience, dérivé du concept de frontière stochastique en économie et s'appuyant sur des connaissances géométriques spécifiques au patient pour améliorer la qualité des traitements de curiethérapie à haut débit de dose pour le cancer de la prostate. Cent plans cliniques de curiethérapie à haut débit de dose de la prostate ont été utilisés dans cette étude, dans laquelle l'échographie transrectale était la seule modalité d'imagerie. Une fraction unique de 15 Gy a était prescrite à tous ces patients. Un algorithme de recuit simulé de planification inverse a été appliqué pour réaliser tous les plans et Oncentra Prostate a été employé comme système d'imagerie et de planification du traitement en temps réel. Les recommandations relatives aux paramètres de dose de la société américaine de curiethérapie pour la cible et les organes à risque ont été suivies. Les relations entre les paramètres géométriques et les paramètres dosimétriques d'intérêt sont examinées. Les paramètres géométriques sont liés aux dimensions anatomiques des patients et ceux associés aux cathéters. Pour déterminer les paramètres géométriques dominants dans un modèle de frontière stochastique donné, les relations monotones entre les paramètres géométriques et les paramètres dosimétriques d'intérêt sont mesurées avec une approche non paramétrique, à savoir le coefficient de corrélation de Spearman. Ensuite, une recherche de force brute est effectuée pour un modèle donné dans lequel différents modèles, incluant toutes les combinaisons possibles des paramètres géométriques dominantes, sont optimisés. L'optimisation est accomplie en utilisant une méthode de vraisemblance maximale implémentée dans le progiciel de calcul statistique R, avec son algorithme de recuit simulée généralisée. Le test du rapport de vraisemblance et sa valeur-p correspondante sont utilisés pour comparer la signification statistique de l'ajout de nouveaux paramètres géométriques aux modèles. Un modèle de production pour la cible et un modèle de coût pour chacun des organes à risque sont développés pour le traitement par curiethérapie à haut débit de dose guidé par l'échographie transrectale. De plus, pour valider si chacun des modèles développés est universel, nous l'appliquons à une autre catégorie de traitement de la curiethérapie à haut débit de dose, dans laquelle la tomodensitométrie était utilisée comme modalité d'imagerie plutôt que de l'échographie transrectale. Ainsi, une nouvelle cohorte de cent plans cliniques curiethérapie à haut débit de dose guidés par la tomodensitométrie est prise en compte. Un modèle de frontière stochastique de production pour la cible et trois modèles de coût pour les organes à risque basés sur la tomodensitométrie sont développés. Enfin, les modèles intégrés de la tomodensitométrie et de l'échographie transrectale sont comparés.

Abstract

This thesis focuses on developing an experience-based quality control (QC) tool, derived from the concept of stochastic frontier (SF) analysis in economics and based on patient-specific geometric knowledge to improve the quality of the high-dose-rate brachytherapy (HDR-BT) treatment for prostate cancer. One hundred clinical HDR prostate BT plans, using the transrectal ultrasound (TRUS) as the only imaging modality, all treated with a single fraction of 15 Gy, and made using Inverse Planning Simulated Annealing (IPSA) algorithm, are studied. Also, Oncentra Prostate system is employed as the real-time 3D prostate imaging and treatment planning system. American Brachytherapy Society dose parameter recommendations for target and organs at risk (OARs) were followed. Relationships between all the different geometric parameters (GPs) and the four dosimetric parameters (DPs) V100 of the prostate, V75 of the bladder and rectum, and D10 of the urethra were examined. Geometric information of the patients and catheters are considered as different GPs. To find the dominant GPs in a given SF model, monotonic relationships between the GPs and DPs of interest are measured using a nonparametric approach: the Spearman correlation coefficient. Then, to determine the optimal SF model for each of the target production SF, and the OARs cost SF models, brute-force searches are performed. Different SF models including all the possible combinations of the dominant GPs in the SF model under study are optimized. Optimization is done using a maximum likelihood method implemented in the statistical computing package R, along with its Generalized Simulated Annealing algorithm. The likelihood ratio test and its corresponding p-value are used to compare the statistical significance of adding new GPs to SF models. A production SF (PSF) model for the target, and a cost SF (CSF) model for each of the bladder, rectum, and urethra are developed for TRUS-guided HDR-BT treatment. The difference between the dose value of a plan obtained by IPSA and the one predicted by an SF model is explored. Additionally, to verify if each of the models developed for the TRUS-guided category of the HDR-BT treatment for prostate is universal, we apply it on another category of HDR-BT treatment, in which computed tomography (CT) was used as the imaging modality. So, a different cohort of one hundred clinical CT-guided HDR-BT plans is taken into consideration. A target production SF and three OARs cost SF models are developed for the CT-based plans. Subsequently, the built-in SF models for the TRUS-based and CT-based plans are compared.

Contents

List of Tables

List of Figures

List of Acronyms

Acronyms

2D	*Two Dimensional*
3D	*Three Dimensional*
ABS	*American Brachytherapy Society*
BT	*Brachytherapy*
CAPCA	*Canadian Association of Provincial Cancer Agencies*
CI	*Coverage Index*
CPQR	*Canadian Partnership for Quality Radiotherapy*
CT	*Computed Tomography*
CTV	*Clinical Target Volume*
CSF	*Cost Stochastic Frontier*
DHI	*Relative Dose Homogeneity Index*
DNR	*Dose Non-uniformity Ratio*
DP	*Dosimetric Parameter*
DVH	*Dose-Volume Histogram*
EBRT	*External Beam Radiation Therapy*
EI	*External Volume Index*
GenSA	*Generalized Simulated Annealing*
GP	*Geometric Parameter*
GTV	*Gross Tumor Volume*
HDR	*High-Dose-Rate*
HDR-BT	*High-Dose-Rate Brachytherapy*
HD	*Hausdorff Distance*
HIPO	*Hybrid Inverse Planning Optimization*
ICRU	*International Commision on Radiation Units & Measurements*
IMRT	*Intensity Modulated Radiation Therapy*
IP	*Inverse Planning*

IPSA *Inverse Planning Simulated Annealing*
KBP *Knowledge-Based Planning*
LDR *Low-Dose-Rate*
LDR-BT *Low-Dose-Rate Brachytherapy*
Linac *Linear Accelerator*
LCGP *Linear Combination of Geometric Parameters*
LL *Log-Likelihood*
LRT *Likelihood Ratio Test*
LOESS *locally estimated scatterplot smoothing*
MLL *Maximum log-Likelihood*
MLC *MultiLeaf Collimator*
MLL *Maximum Log-Likelihood*
NIST *National Institute of Standards and Technology*
NT *Normal Tissue*
NTCP *Normal Tissue Complication Probability*
OARs *Organs At Risk*
OcB *Oncentra Brachy*
OcP *Oncentra Prostate*
ODI *Overdose Index*
PDF *Probability Density Function*
PDR-BT *Pulsed-Dose-Rate Brachytherapy*
PSDL *Primary Standards Dosimetry Laboratory*
PSF *Production Stochastic Frontier*
PTV *Planning Target Volume*
QA *Quality Assurance*
QARSAC *Quality Assurance and Radiation Safety Advisory Committee*
QC *Quality Control*
ROI *Region of Interest*
RT *Radiotherapy*
RTOG *Radiation Therapy Oncology Group*
SA *Simulated Annealing*
SF *Stochastic Frontier*
SCC *Spearman Correlation Coefficent*
TCP *Tumor Control Probability*
TPS *Treatment Planning Systems*
TRUS *TRansrectal UltraSound*

US *UltraSound*

VOIs *Volumes Of Interest*

Introduction

Cancer is the second leading cause of death worldwide. According to the 2018 special report published by the Canadian Cancer Society (1), cancer is the leading cause of death in Canada. Nearly one in two Canadians is anticipated to be diagnosed with cancer during their lifetime, and about one in four will die. What is that disease exactly? Cancer is a collection of diseases in which the cells of the body start to divide uncontrollably, resulting in a malignant growth or tumor. One of the most frequently diagnosed cancers among Canadian men is prostate cancer, which is the third leading cause of death from cancer among males in Canada. The prostate is a gland situated in front of the rectum, between the bladder and the penis, with the urethra passing through the center of the prostate. One in seven Canadian men will be diagnosed with prostate cancer during their lifetime. Based on the estimation reported by the Canadian Cancer Society in 2017, a daily average of 58 Canadian men was diagnosed with prostate cancer, and 11 died. Those statistics shed light on the importance of performing research in the realm of prostate cancer treatment in order to save and increase the quality of life of people fighting against the disease.

Since the discoveries of radioactivity by Henri Becquerel in 1896 and of radium nearly two years later by Marie Curie, Man's life has been influenced to a great extent by practical applications of radioactivity in many aspects including but not limited to industry, nuclear power, and medicine.

Depending on the type, the site, and the stage of cancer, there are some possible treatments such as surgery, chemotherapy, and radiation therapy. Radiation therapy can be categorized into two principal modalities: external-beam radiation therapy (EBRT) and internal radiation therapy, namely brachytherapy (BT). As opposed to the EBRT, in which the source of the radiation is outside the patient, in BT the radioactive sources (i.e., seeds) are inserted inside the body, directly into the tumor (2). An advantage of BT compared to EBRT is that most of the radiation dose released by a BT seed is in its vicinity. Also, in BT, the radiation does not need to pass through healthy tissues in order to reach the target, which in turn reduces the risk of damaging healthy tissues. Consequently, a localized dose is offered by the dosimetric distribution of BT compared to EBRT (3). There is undeniable evidence from practices in many clinical sites pointing to the advantages of applying modern BT in treating cancers such as prostate (4), cervix (5), breast (6) and head and neck (7). That is owing to the advancement of BT over the past decade along with the development of a number of technologies such as afterloading technology (8), computer-assisted treatment planning (9, 10, 11), transrectal

ultrasound (TRUS)-guided implants (12), image-guided adaptive brachytherapy (13, 14), and quantitative dosimetry (9). Extensive reviews (15, 16, 17, 18) and books (10, 11, 19, 20) are discussing these advances.

There are two techniques for clinically localized prostate radiotherapy: the first is the permanent implantation of radioactive seeds in the cancerous tissues, and the second is the temporary implantation of the seeds, by which the seeds are inserted and then removed after releasing the required dose (21). Based on the definitions of the International Commission on Radiation Units & Measurements (ICRU), BT treatments can be different depending on the rate at which the dose is delivered (i.e., dose rate). A dose rate ranges between 0.4 and 2 Gy/h is referred to as low-dose-rate brachytherapy (LDR-BT), between 2 Gy/h and 12 Gy/h is known as the medium dose rate brachytherapy (MDR-BT), and at 12 Gy/h or more is called high-dose-rate brachytherapy (HDR-BT). Additionally, in pulsed-dose-rate brachytherapy (PDR-BT), the dose is delivered in a large number of small fractions with short intervals (22). In LDR-BT for prostate cancer (23), seeds such as iodine-125 (^{125}I) (24) and palladium-103 (^{103}Pd) (25) are placed permanently in the prostate. However, in the case of HDR-BT for prostate cancer, high-energy radionuclides such as Iridium-192 (^{192}Ir) (26, 27, 28) are temporarily placed at the predetermined positions in the prostate (3).

BT boost refers to a treatment in which BT is used in combination with EBRT (29). Although LDR-BT or HDR-BT monotherapy can be used as a treatment option for patients showing low risk and intermediate risk of prostate cancer (30, 31), BT boost is a treatment option for patients at high risk of the disease (32, 33, 34). In the case of LDR-BT boost, the implant is usually inserted after EBRT is delivered (35). However, in HDR-BT boost (36, 37), EBRT can be delivered before, along with, or after BT (29).

Brachytherapy for Prostate Cancer

LDR vs HDR brachytherapy for prostate cancer

The application of a TRUS-guided remote afterloading system was suggested to deliver a high dose of radiation to the prostate while minimizing the dose received by the OARs (i.e., bladder and rectum). Additionally, this approach was proposed to tackle some limitations of the TRUS-guided LDR-BT, such as the strong dependence on the radiation oncologist for precisely place the seeds in the prostate, the difficulty of modifying the seeds after their insertion, and the variability of dosimetry between implants (29, 33).

During an HDR-BT procedure, which is performed in a shielded operating room, a radiation oncologist inserts catheters through the perineum directly into the prostate. After the catheters are positioned inside the prostate, a 3D image set is acquired to precisely contour the shape of the prostate, urethra, bladder, and rectum for treatment planning (38). It is important to acknowledge that the CT scanning

overestimates the contoured volumes as compared to the MRI and TRUS (39, 40). The CT-based volumes are proven to be larger, approximately 50%, compared with the TRUS-based volumes (39). However, studies have shown that specific prostate volumes can be obtained using both MRI and TRUS imaging modalities (40, 41, 42, 43). Fig. 0.1 shows an afterloader, which is a system that automatically deploys and retracts an HDR seed along a catheter at specified positions and time. By using an afterloader, the HDR seed can be remotely controlled to be stopped at pre-established positions (dwell positions) for a pre-planned time frame (dwell time).

Note that the HDR-BT treatments can be delivered directly after treatment planning, and there is no need to change the position of the patient when using a 3D ultrasound planning system. However, when utilizing CT planning, variations in the position of some catheters about their planned positions can occur because the patient needs to be transferred, sometimes to a different room, to acquire CT images (44, 45, 46). Even if the possibility to acquire CT images in the same operating room, the patient's legs must always be lowered for image acquisition. Catheter displacement between planning and treatment delivery, and the corresponding dosimetric impact, in the treatment of prostate cancer patients, has been discussed in several studies (47, 48, 49). However, by using TRUS technique, not only as the guidance but also for planning, there is no need to displace the patient. Therefore, the catheter displacement is minimized (50). That is one of the best benefits of employing TRUS in HDR-BT rather than CT scanning through the pelvic region. Fig. 0.2 represents the dose absorption

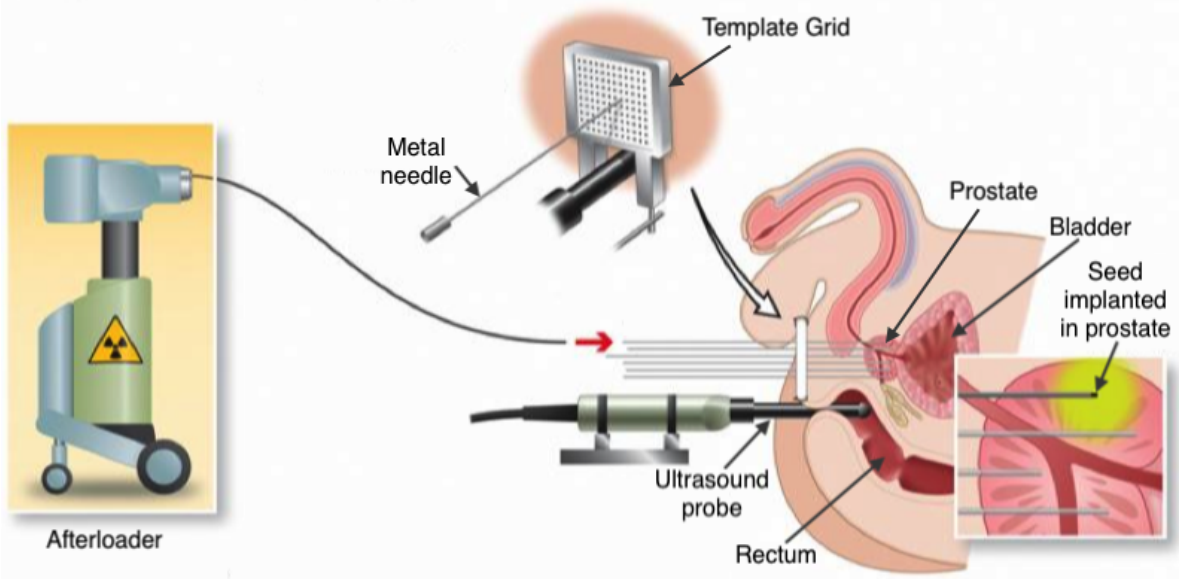

Figure 0.1 – Transrectal Ultrasound (TRUS) probe placed in the rectum and a template grid located at the skin between the anus and scrotum used to guide the insertion of metal needles into the prostate. An HDR seed is remotely directed via a thin cable from an afterloader and traveled inside the needles (51).

in water as a function of distance from a point source in Log scale, in which the dose is normalized to 100% at a distance of 1 cm. The dose associated with HDR-BT with the radioactive seed ^{192}Ir

is shown in blue, and the dose associated with the LDR-BT with ^{103}Pd and LDR-BT with ^{103}I are illustrated in light and dark green respectively. Getting further away from the source leads the dose to drop quickly in both LDR- and HDR-BT, and less than 10% of the dose is delivered to the tissues further than 4 cm away. The high-energy HDR-BT deviates a little from the inverse square ($1/r^2$) law. However, the LDR-BT with two low-energy seeds shows more absorption at a shorter range than the HDR-BT (29). Additionally, in the case of LDR-BT, the precise deployment of seeds is strongly

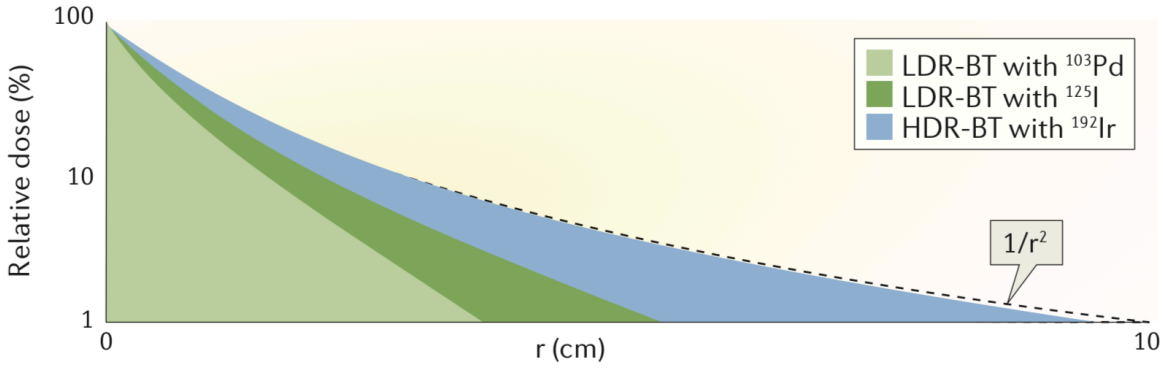

Figure 0.2 – Log scale distribution of dose in water as a function of the distance from a point source associated with three isotopes, ^{103}Pd, ^{125}I and ^{192}Ir, used in BT for prostate cancer. The LDR-BT with ^{103}Pd and ^{125}I respectively shown in light and dark green, and the HDR-BT with ^{192}Ir in blue (29).

.

dependent on the expertise of the operator. Also, once the seeds are deposited in the prostate, their positions cannot be adjusted (29, 33). Note that after delivering an HDR-BT treatment, no radioactive seeds remained inside the patient, and therefore, there is no radiation exposure for the hospital staff nor the people around the patient.

The current water-based BT dose calculation in the BT dose planning systems are performed based on the formalism of the Task Group No.43 (TG-43) protocol (52, 53) of the American Association of Physicists in Medicine (AAPM). Additional to the AAPM TG-43 dosimetry formalism (52), the 2004 update (TG-43U1) (53), the 2007 Supplement (TG-43U1S1) (54), and the 2017 Supplement 2 (TG-43U1S2) (55) are used in BT dose calculation. The AAPM TG-43 formalism will be discussed in 1.1.2.

The advantages of using HDR-BT treatment for prostate cancer, are, but not limited to: the precise implantation, which can be extended to comprise the seminal vesicles and extracapsular disease, owing to the application of image-guided catheter placement (56, 57, 58, 59); the minimized target and OARs motions (3, 38); the possibility to individualize the source positions throughout the extent of the prostate in reference to a determined planning target volume and OARs (38, 60); the highly conformal dose delivery provided by the inverse planning dose distribution optimisation (38, 61); the application of high doses per fraction as a biological dose advantage for tumors with a low alpha beta ratio (62, 63); no source preparation time for performing stepping source temporary BT, low dependency on the operator, and a good radiation protection for the treatment staff (21, 29, 64); low risk of severe

side effects for the patient; and a favourably cost-effective technique because of the possibility of using a single source for a large number of patients (65) by a multipurpose equipment. Therefore, using HDR-BT for the treatment of prostate cancer provides us with the most state-of-the-art method to deliver a high dose of radiation to the target while minimizing the dose to the OARs such as the bladder, rectum, and urethra (66, 67, 3). Consequently, the focus of this work is on the HDR-BT utilized as a curative treatment for patients with localized prostate cancer.

Brachytherapy Target Delineation

The detailed information regarding HDR-BT for prostate is accessible from American Brachytherapy Society (ABS) consensus guidelines (68, 69). The gross tumor volume (GTV) is the location and extent of the malignant growth, as shown in Fig. 0.3. In other words, GTV is defined as what can be observed, palpated or imaged, which comprises the primary tumor and the developed lymph nodes, or distant metastases according to physical examination and imaging. Therefore, the GTV is a purely biological concept (70). The clinical target volume (CTV), as illustrated in Fig. 0.3, is composed of GTV and a margin to consider the sub-clinical disease extension, which must be eliminated. The CTV, like GTV, is a purely biological concept (70). In order to achieve the goal of the therapy, which is cure or palliation, the CTV volume has to be treated sufficiently.

The Planning Target Volume (PTV) is a geometrical concept utilized for treatment planning. The PTV comprises the CTV as well as an extra margin to take into account the net effect of all the possible geometrical variations and inaccuracies such as any setup error, organ movement, and patient movement. By defining PTV, one ensures that the prescribed dose is indeed absorbed in the CTV. Fig. 0.4(a) represents the PTV (in purple), which is the CTV (in light blue) plus a typical expansion of 0.5 cm to 1.0 cm (71). That expansion is required in EBRT due to possible differences in patient positioning on the linac table and prostate movement caused by changes in the adjacent organs. In order to cover PTV in EBRT, the radiation beam has to go through the soft tissues of the pelvis. However, in the case of BT, as illustrated in Fig. 0.4(b) and (c), since a setup error is rare, the extension of CTV to define PTV can usually be minimized. Consequently, in BT, CTV is equivalent to PTV. However, there are some exceptions, for example, ultra-focal HDR treatment, in which only a target lesion or subvolume of the prostate is being treated (72). As shown in Fig. 0.4(b), in LDR-BT, the LDR seeds are permanently placed in the target, which in turn results in the dose cloud covering the CTV. So, movements of an organ or a patient following the insertion of the seeds are allowed. In HDR-BT, as shown in Fig. 0.4(c), the needles, which are positioned in the target during the temporary implant, fix the prostate in place to avoid its movement in the course of transferring the seed to the defined dwell positions using an afterloading system. Note that the position of the catheters in the HDR-BT for prostate can be shifted between the planning and treatment delivery stages. So, it is highly recommended to verify internal catheter positions immediately before any HDR prostate BT treatment delivery (73, 44).

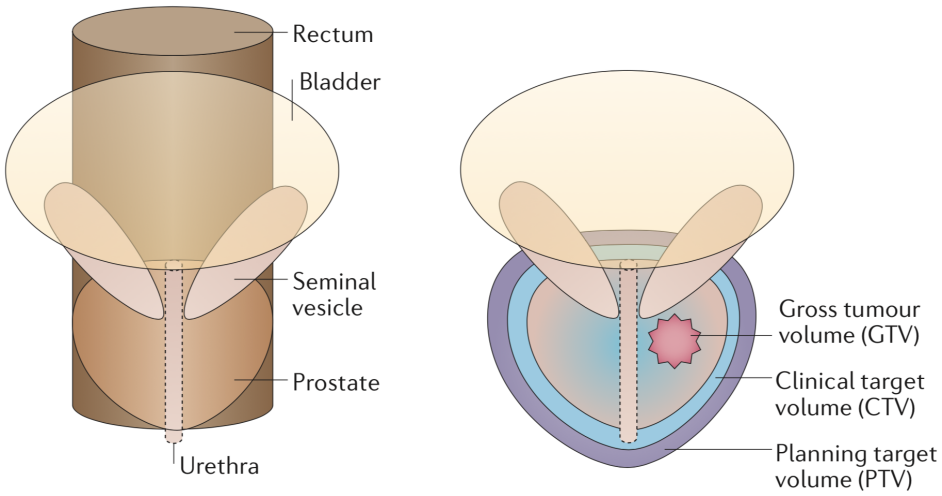

Figure 0.3 – On the left, an anteroposterior illustration of the target and main organs at risk. On the right, the gross tumor volume (GTV) in red, the clinical target volume (CTV) in light blue, and the planning target volume (PTV) in purple (29).

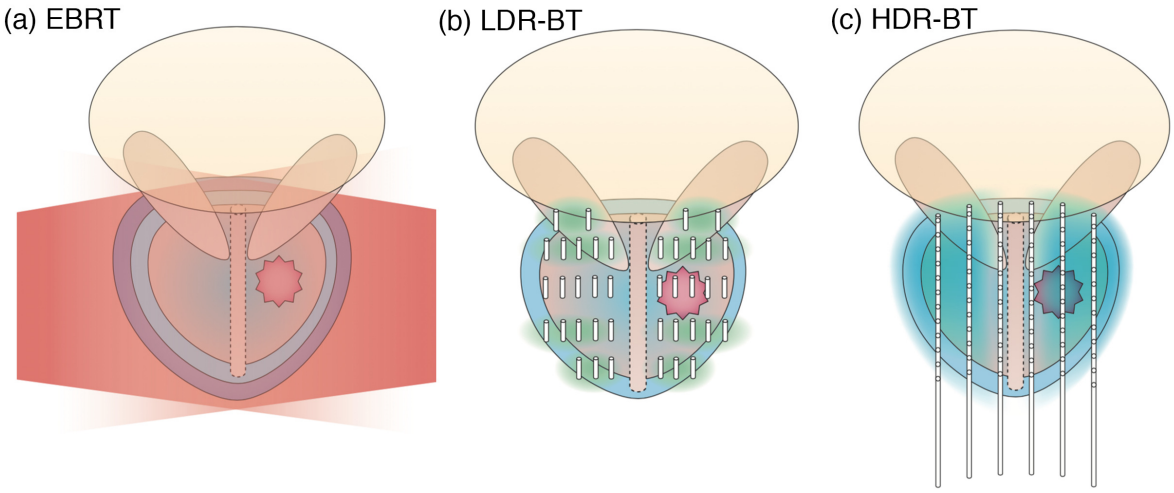

Figure 0.4 – In EBRT(a), the PTV, which is the CTV plus an expansion, shown in purple, is contoured for the prostate by going through some soft tissues. For both BT, LDR in (b) and HDR in (c), contouring the PTV as an expansion to the CTV is not needed. In (b), the LDR seeds are shown as small cylinders deposited in the CTV, which deliver the prescribed dose (green cloud) to the CTV. In (c), an HDR seed visits all the dwell positions represented as circles within the needles placed in the prostate, for predefined dwell times in order to deliver the prescribed dose (blue cloud) (29).

Problematics

Quality assurance (QA) in radiotherapy (RT) is defined as "all procedures that ensure consistency of the medical prescription, and safe fulfillment of that prescription, as regards to the dose to the target volume, together with minimal dose to normal tissue, minimal exposure of personnel and adequate patient monitoring aimed at determining the end result of treatment" (74). Thus, a QA has to deal with all aspects of the appropriate delivery of RT, such as programmatic organization, the qualifications of the staff included in RT, the optimal performance of the equipment used in the planning and treatment stages, procedures and policies, supervising the incidents, and providing the reports (75). Almost every RT program in Canada is utilizing the current version of Quality Assurance Guidelines for Canadian Radiation Treatment Programs (75).

The Canadian Partnership for Quality Radiotherapy (CPQR) along with the Quality Assurance and Radiation Safety Advisory Committee (QARSAC) tackled a comprehensive review of the previous CAPCA Standards produced by the Canadian Association of Provincial Cancer Agencies (76). The result was a suite of documents, named technical quality control (QC) guidelines, which guide the safe and consistent utilization of RT equipment and technologies in Canada.

Despite many studies performed to achieve a full quantification of the decision-making procedure for the RT treatment plan evaluation, judgments on the degree of the quality of a plan are, yet, subjective and can demonstrate variability among the planners with different planning experiences and preferences, even if their clinical treatment objectives are the same (77). The principal challenge in the QC of a BT treatment, as of an EBRT, is to obtain a balance between target-coverage and OAR-sparing. OARs sparing evaluation has been a very difficult task, notably because of the complication in clinical objectives, the distinctive variations in patients' anatomies, insufficient quantitative metrics to judge whether a BT plan is optimal or not, and the subjectivity and corresponding experience of the experts involved in the planning procedure (77, 78, 79).

An important number of problems should be discussed when judging the quality of a treatment plan. First, there are uncertainties on the current dose-response knowledge. These uncertainties occur when a global knowledge needs to be translated to the institutional level in order to standardize the treatment quality. Some of the challenges in producing general dose-response recommendations for different RT treatment sites are: the consistency for the delineation of clinical target volumes (CTVs) and OARs, as well as for attaining the results; the great complexity in assessing the real dose delivered to the patient; and the relationship between the delivery systems and procedures used in different clinics and their corresponding total results (77). Consequently, there are cases in which people involved in RT treatment planning are unable to obtain the required trade-offs between the normal tissue complication probability (NTCP) and tumor control probability (TCP) when applying general dose-response recommendations. In these cases, planners are compelled to rely on their judgments, which in turn yields variations in treatments and results (77). The American Brachytherapy Society (ABS) dose parameter

recommendations for target and OARs are usually followed for a given patient in a BT treatment (80). Nevertheless, regardless of the planner's experience, a procedure that depends on the subjective and qualitative evaluation of OARs sparing will frequently encounter two potential pitfalls. First, in some patients for whom further sparing of OARs is attainable, it is possible that treatment planners do not put in extra effort to yield a dose distribution that spares those OARs beyond the standard objective. Falling into that pitfall will result in under sparing the OARs (78). Second, there are some unfavorable clinical cases in which the geometry of patients makes it nearly impossible for the treatment planner to fulfill one or more clinical objectives without impermissible loss of another clinical objective. In order to tackle these unfavorable cases, treatment planners might spend too much inefficient time and effort trying to achieve the clinical objectives (78). The second problem is related to the uncertainty caused by the rapid pace of adopting new technological developments in the RT field (81). Some examples of new technologies used in RT are: the different forms of intensity-modulated radiation therapy (IMRT) (82, 83); computer-assisted treatment planning (10, 11); using TRUS for image-guided implants (12); image-guided adaptive brachytherapy (14, 84). When new RT technologies and new methodologies are introduced, the professionals who start using these technologies are the ones who develop protocols, and subsequently, provide them to other users. However, not only those procedures usually lag behind the rapidly developing technologies, but also one needs to take the learning curves of staff into account (77).

There are many individuals performing treatment planning each with different experiences, which are not necessarily related to the same treatment planning system (TPS) nor the same objectives. However, professionals in the RT field can share knowledge only in the boundary of their experience with those that have utilized almost the same TPS, dose delivery devices, and clinical objectives (78). Nevertheless, even under those circumstances, comparing the quality of treatment plans have continued to be challenging. This challenge is because dose optimality is dependent on the anatomy of an individual patient. Considering the increase in the number of patients using BT treatment for prostate cancer and the augmentation of the complexity of the treatments, the necessity for QA in BT has become apparent. So far, the basis for QC comparison has been dependent on the clinical experience and results on a patient, and, relatively, on the subjective experience of the physicians, medical physicists, and dosimetrists involved in the planning process (77).

The third problem to mention is related to human errors. The lack of experience and inefficiency of the planners to attain optimal solutions acts negatively with the previously mentioned challenge of obtaining a trade-off between NCTP and TCP. Therefore, in the absence of quantitative benchmarks, a conclusion of optimality cannot be promised. Hence, the clinical experts involved in the treatment planning should be not only more attentive to their judgment errors, but also the technical errors (77).

Goal of this Research Project

The goal of this research project was to develop an experience-based QC tool derived from the stochastic frontier analysis concept and based on patient-specific geometric knowledge to improve the quality of planning for TRUS-guided HDR-BT treatment. The idea was to analyze the treatment plans of previously treated patients in order to develop models that could predict target and OARs doses of future treatment plans as a function of patient-specific geometries.

In this study, we used one hundred clinical HDR prostate BT plans, in which TRUS is the only imaging modality, to develop the TRUS-based stochastic frontiers. The Oncentra Prostate (OcP) system (Elekta Brachytherapy, Veenendaal, The Netherlands) was employed as a TPS and for real-time 3D prostate imaging. The Inverse Planning Simulated Annealing (IPSA) algorithm was used to optimize all the treatment plans in this study (85, 86, 87). All the patients were treated with a single fraction of 15 Gy. ABS dose parameter recommendations for the target and OARs were followed. We developed a TRUS-based production stochastic frontier (PSF) model for the target. Additionally, we developed a TRUS-based cost stochastic frontier (CSF) model for each of the bladder, rectum, and urethra.

Furthermore, we used a different cohort comprising one hundred clinical cases of CT-based HDR-BT treatment plans for prostate cancer to develop CT-based target PSF, as well as a CT-based bladder, rectum, and urethra CSF model. Note that all the patients in this cohort were treated with a single fraction of 15Gy. Also, the treatments of these patients were optimized using the IPSA on Oncentra Brachy TPS (Elekta-Brachy). To develop these CT-based PSF and CSF models, we evaluated the values of the dosimetric parameter (DPs) and the geometric parameters (GPs) based on the data of the one hundred new CT-based plans.

To develop these experienced-based models for the target PSF and OARs CSF, we utilized a model in economics, known as stochastic frontier analysis (SFA). SFA is a mathematical model, which was initially introduced in economics to evaluate the technical inefficiency of producers in respect of an optimal frontier (88, 89). We employed SFA to optimize the output in terms of inputs, and subsequently, to determine a frontier. In the case of BT treatment planning, we utilized the SFA to optimize the dose as the output in terms of the geometric parameters as the inputs.

We examined the relationships between GPs and DP of interest. We took into account the DPs including the dose V100 to the target, V75 to the bladder, V75 to the rectum, and D10 to the urethra. Furthermore, we considered the GPs related to the geometry of patients. These patient-related GPs comprise the volume of the target, the volume of the OARs (i.e., bladder, rectum, and urethra), and the Hausdorff distance (HD) between the target and OARs. Moreover, we considered the GPs related to the implanted catheters. These catheter-related GPs include the ratio of number of inserted catheters and the maximum surface of the prostate, the ratio of area enclosing all the inserted catheters and the maximum surface of the prostate, the average distance between all the catheters and the minimum

distance between the active points of the catheters placed in the lowest portion of the prostate and their closest points on the midplane and full length of the rectum.

Note that, as opposed to the planning tools developed by using Knowledge-Based Planning (KBP), the frontiers developed by SF analysis are not penalized by bringing in the non-optimized plans. The assumption is that the degradation of the quality of a plan with respect to an optimal frontier results from two error components. The first error component is associated with factors that are uncontrollable by treatment planners such as the geometry of the target, the geometry of the OARs, and the geometry between the target and OARs. That random error component, which captures the effects of statistical noise, can increase or decrease the productivity of a plan, and shift it above or below its PSF. The second error component is related to controllable factors in the process of treatment planning such as the efficiency and competency of clinicians taking part in the planning. That second error component, which includes the influence of technical inefficiency, has a negative effect on the dose to the OARs.

Additionally, in order to establish if each of the TRUS-based SF models is universal, we individually verified the application of each of the target PSF, and bladder, rectum, and urethra CSF models on another category of HDR-BT treatment plans for prostate cancer. The imaging modality used in this cohort is CT rather than TRUS. The goal was to verify that the SF models can be adopted to other imaging modalities. We used a different cohort including one hundred CT-based clinical HDR-BT treatment plans for prostate cancer to develop a CT-based target PSF, and a bladder, rectum, and urethra CSF models. Finally, we compared the developed CT-based target PSF to its corresponding TRUS-based PSF. We carried out the same comparison between each of the developed CT-based bladder, rectum, and urethra CSFs and their corresponding TRUS-based CSFs.

As a result, using our QC tool including all the developed SF models enables planners to predict, before the treatment planning, the possible trade-off between the target coverage and OARs sparing. Therefore, planners avoid OARs under sparing or wasting time and effort trying to obtain impossible dose objectives. Consequently, the quality of the HDR-BT treatment plans will be improved.

Outline of this Thesis

In this work, first, the procedure for BT treatment of the prostate was briefly discussed and the two imaging modalities used in the implantation and reconstruction steps, namely CT and TRUS, are compared. Then, the dosimetry, planning and dose optimization of HDR-BT treatment for prostate are introduced. Also, since all the treatment plans in this work are optimized by using the Inverse Planning Simulated Annealing (IPSA) algorithm, IPSA will briefly reviewed.

Subsequently, an overview of the theory of stochastic frontier analysis is discussed as a basis for understanding the results of our experience-based QC tool developed for improving the quality of

planning for TRUS-guided HDR-BT treatments by considering the patient-specific geometric knowledge. Since the PSF and CSF models used here were developed based on the geometric information of patients treated with HDR-BT, the process of data collection and evaluation applied in this research project were outlined. Also, the DPs and GPs taken into consideration to develop the SF models were detailed. Then, the optimization using the MLL method implemented in the statistical computing package R, as well as its Generalized Simulated Annealing (GenSA) algorithm were described. In order to compare the statistical significance of adding a new GP to an SF model, the LRT and its p-value were employed.

Afterward, a nonparametric approach, called the Spearman correlation coefficient (SCC), was used to measure the monotonic relationships between the GPs and DPs of interest, to assess the importance of incorporating each of the GPs into a given SF model, and, accordingly, to find the dominant GPs. Additionally, a systematic approach, namely the brute-force search, was applied in order to consider all the possible combinations of the chosen GPs for each of the target PSF model, as well as the bladder, rectum, and urethra CSFs, and to optimize the associated SF models. Then, the optimal target PSF and OARs CSF models developed based on TRUS-based HDR-BT plans were presented.

Finally, to demonstrate that each of the SF models developed for the TRUS-based HDR-BT treatment is universal, the models were tested on the CT-based HDR prostate BT. Therefore, one hundred clinical HDR prostate BT plans, in which CT was implemented as the imaging modality rather than TRUS, were used to calculate a target PSF and three OARs CSF models. Subsequently, each built-in CT-based PSF or CSF model is compared with its corresponding TRUS-based SF model.

Chapter 1

Theoretical Overview

1.1 HDR Brachytherapy Treatment for Prostate Cancer

Generally speaking, HDR-BT treatment for prostate cancer includes: placing the catheters in the target using imaging as guidance; acquiring images while the catheters are in position; reconstructing the catheters, as well as contouring the target and OARs (i.e., bladder, rectum, and urethra) on the TPS; optimization of the dwell time in order to obtain the required dosimetric constraints; performing quality assurance, for example second controlling of the catheter positions and the plan; and delivering the treatment plan to the patient (50). Significant advancements of imaging in BT in the last decades has risen from the advancements in volumetric imaging such as magnetic resonance imaging (MRI), computed tomography (CT), and transrectal ultrasound (TRUS). In the past, there were situations in which the geometry of applicators was used to prescribe the treatment and to show the dose distribution. Due to the recent developments in the 3D imaging, patient-specific anatomy images are employed to optimize and represent the dose distribution (2). Note that the focus of this research project is on the TRUS-based category of the HDR-BT treatment for prostate cancer. Furthermore, we verify if the developed TRUS-based SF models are universal and can perform well for another category of the HDR-BT for prostate cancer. Therefore, the TRUS-based target PSF model, as well as the bladder, rectum, and urethra CSF models are compared to their corresponding CT-based models. Thus, in the following section, these two 3D imaging modalities in BT, CT, and TRUS are discussed.

1.1.1 Imaging Modalities in HDR Brachytherapy for Prostate Cancer

In HDR-BT for prostate, a radioactive source, usually ^{192}Ir, is used to irradiate the prostate through interstitial catheters, placed within the prostate gland. Note that there are significantly high dose gradients of 20%/mm at 1cm from the source channel for ^{192}Ir (90). Therefore, the precise positioning of catheters is important. Furthermore, the correct delineation of the prostate and OARs an HDR-BT treatment for prostate as well as the precise reconstruction of the catheter positioning (i.e., 2 mm by

GEC-ESTRO and 1 mm by AAPM) is essential. Catheters are usually positioned within the prostate under TRUS imaging guidance. MRI or CT imaging modalities have been, also, reported as guidance for catheter insertion (91, 92). For the planning, MRI, TRUS, or CT can be used while the catheters are in position. As stated before, CT has the advantage of the high visibility of the inserted catheters. However, using CT as the imaging modality in an HDR-BT brings the risk of catheter displacement. That is due to the need to change the patient position (e.g., lowering of legs) or to transfer the patient to a different room to perform CT imaging (50). In 2001, intraoperative US was reported to be used in HDR treatment planning (61). Later on, the application of CT in treatment planning became popular due to its improvements, for example in the 3D visualization of the implanted catheters (93). Additionally, cone-beam CT (CBCT) was reported to be used to measure the catheter displacement between CT planning and treatment (94). CBCT was also used, along with TRUS, in the intraoperative setting for BT treatment planning (95).

Moreover, MRI has been employed as guidance for HDR catheters insertion and treatment planning. As compared to CT or US imaging, MRI provides better contrast for different soft tissues in visualizing male pelvic anatomy and prostate cancer. By using MRI images, a better depiction of the tumor and OARs, hence more conformal dose distributions of target volumes can be achieved. Additionally, the dose to OARs and the corresponding toxicity can be minimized. No radiation exposure for the patient or staff is associated with MRI imaging. Furthermore, MRI allows determining the relative position between MRI-compatible BT needles and the surrounding anatomy (96). However, as compared to CT-based and TRUS-based planning methods, MRI can be more time consuming and much more expensive (92).

1.1.1.1 Computed Tomography (CT)

Previous to the development of a more efficient TRUS-only workflow, CT was the imaging modality that was being routinely employed in HDR-BT planning.

Along with the 3D visualization of the anatomy, CT allows the possibility to define the required contours for the target and OARs. Furthermore, CT allows distinction between the bone and high-density material (97). Moreover, CT can be used as the main imaging modality in reconstructing the implants in interstitial BT for head and neck (98), breast (99), as well as the post-planning of seed implants in the prostate (100).

Fig. 1.1 shows a CT-based HDR-BT for prostate, in which the intraoperative TRUS imaging is used as guidance to insert the catheters (needles) within the prostate gland. Afterward, treatment planning is performed, in which a radiation treatment plan is generated based on CT images. However, acquiring CT images for planning requires repositioning the patient in the supine position rather than in the lithotomy position. Additionally, in some institutions, the patient needs to be transferred to another room or department to acquire CT images and then back to the BT treatment room. The repositioning

and the corresponding swelling during patient setup for the acquisition of the CT images yield shifts in needle positions in CT-based HDR-BT treatment for prostate cancer. Mean shifts of 11 mm was reported for needles positioning that occurred between the CT-based planning for single fraction HDR-BT treatment plans (94). This study showed more than 20 mm of inferior shifts for over 10% of the implanted needles. Therefore, evaluation, as well as correction, of any catheter displacement after the optimization process and before the final delivery of the treatment plan are important (94). Fig. 1.2(A) represents an example of the CT-based planning with a highly conformal dose delivery to the prostate. However, Fig. 1.2(B) shows that neglecting the inferior catheter displacement can lead to a critical inaccuracy in dose delivery, such as underdosing of the target and overdosing of the urethra (50).

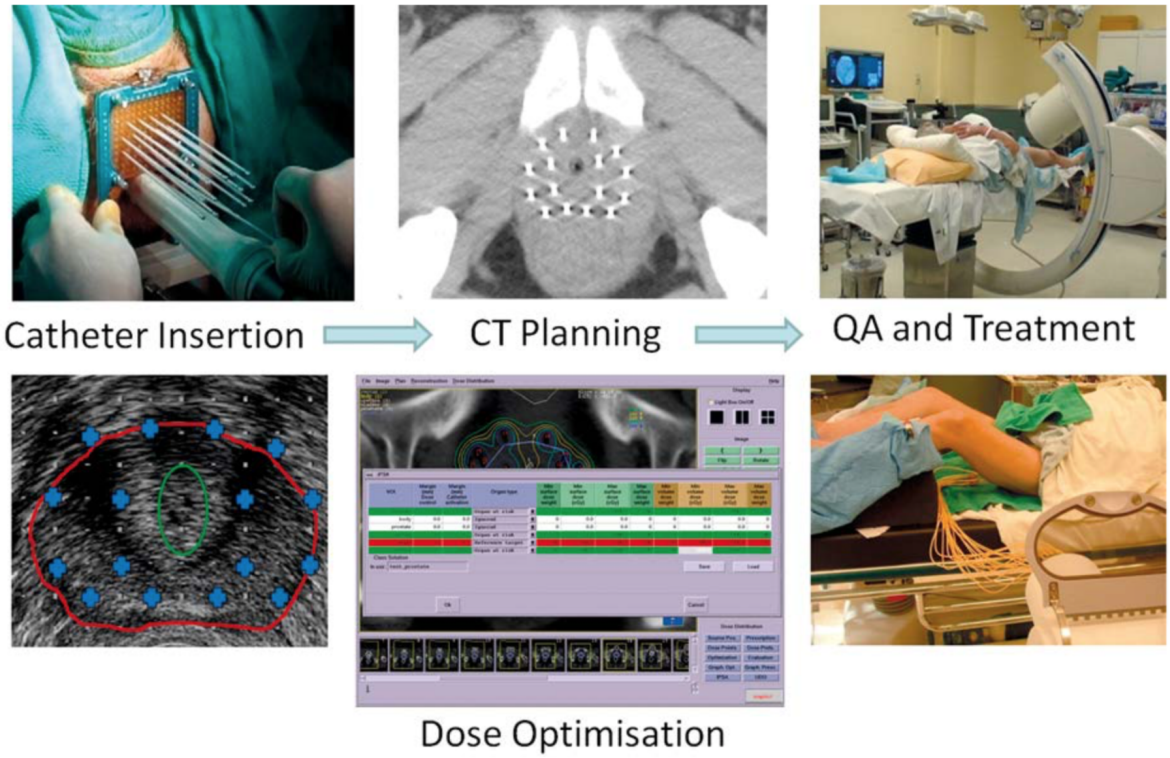

Figure 1.1 – In a CT-based HDR-BT treatment for prostate cancer, catheters are inserted using TRUS imaging modality as the guidance. In order to acquire CT images for planning, the patient legs are lowered, or, in some clinics, the patient is transferred to a different room. After the plan optimization, and before delivering the treatment plan to the patient, corrections for any catheter displacement caused by the changes in the position of the patient is needed. For that reason, quality assurance (QA) in CT-based planning is significant (50).

Furthermore, delineation of the prostate volume in CT images is challenging due to the poor soft-tissue contrast between the prostate and the tissues around it, i.e. its background. The challenge of CT segmentation for the prostate is, also, ascribed to the uncertainty in the delineation of the prostate base and apex using CT images. An inaccurate localization of the prostate in HDR-BT could result in delivering a high dose of radiation to the surrounding normal tissues, such as rectum and bladder. Additionally, the inaccuracy in prostate contouring could give rise to undertreating the tumor within

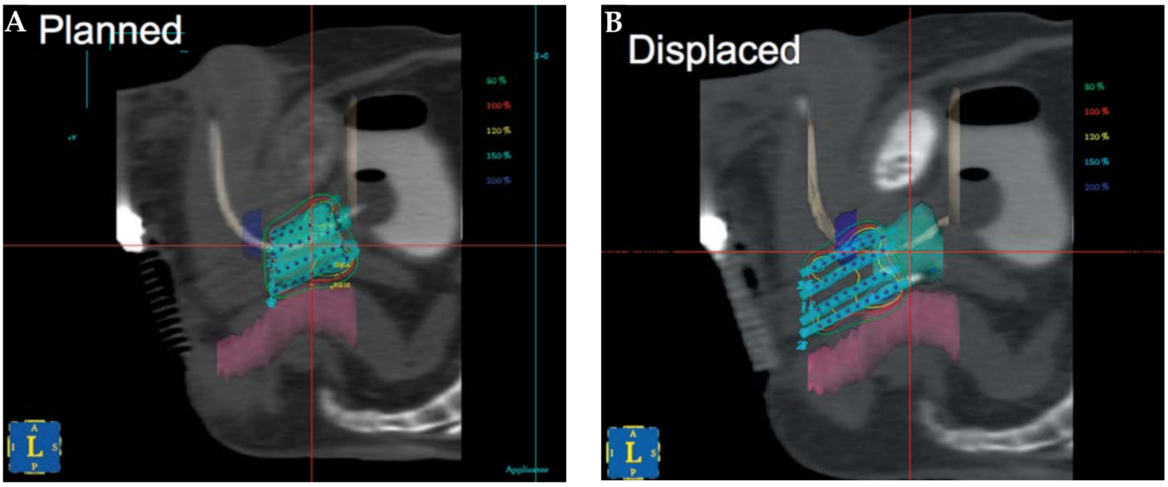

Figure 1.2 – A comparison between two CT-based plannings for prostate HDR-BT: one with a highly conformal dose delivery (A); the other with target underdosing and urethra overdosing due to unspecified inferior catheter displacement (B). (50).

the prostate, hence to a poor treatment result. (101). The existence of lack of consistency, hence variations, in contouring the prostate using CT-based images was reported among physicians (102). Furthermore, it was shown that CT consistently, overestimated the prostate volume by approximately 50% as compared to TRUS (39). In another study, the prostate volume defined based on CT images was reported to be, on average, 32% bigger (range 5%-63%) than the volume defined based on MRI (103). In recent years, investigations have been conducted to introduce new methods that can improve CT prostate segmentation. These methods include, for example, model-based registration-based (104), classification-based (105, 106, 107), and model-based methods (108, 109). Most of these methods are based on the texture and appearance of the prostate on CT images. Also, in HDR-BT for prostate, the CT images are acquired following the insertion of the catheters. Therefore, the texture and appearance of the prostate can be smeared by, for example, the artifacts caused by metal catheters on CT images. Consequently, these methods might not perform well for the prostate HDR-BT implementation (101). Note that flexible catheters can be used in HDR-BT rather than the rigid metal catheters (steel or titanium). Flexible catheters are disposable and more comfortable for the patient if they must be left in position. However, rigid catheters require to be re-sterilized, have a larger dead space at the tip, and are prone to produce more imaging artifact (50).

Finally, taking into account the existed challenges in CT-based HDR-BT for prostate, such as the precise contouring of prostate based on CT images, TRUS and MRI are suggested as superior imaging modalities in terms of prostate contour than CT (102, 41, 110). Studies comparing prostate volume measured using TRUS and MRI have shown that MRI and TRUS prostate volume estimates agree nearly with the prostate volume based on pathological analysis (42, 111). So, although MRI is a more precise technique in ascertaining the prostate volume, TRUS is more efficient, economical, noninvasive, and almost as precise as MRI.

1.1.1.2 Transrectal Ultrasound (TRUS)

Ultrasound (US) is a clinical imaging modality, in which high-frequency sound waves, usually in the range of 1 and 20 MHz, are used. Transducers, generally a piezoelectric crystal, are used to produce the sound waves and to receive the echoes. By applying an electric current to the crystal, hence changing its thickness quickly, sound waves are produced. These generated sound waves are refracted and reflected in the tissue, and their echoes are received by the transducer. Subsequently, the deformations in the crystal coming from the reflected waves are changed into an electrical potential, and also detected, by the transducer. An array of US transducers send sound waves in different directions, which are received after. In other words, the transducers are in brightness (B-) mode. A 2D image plan can be computed based on the detected signals. Each pixel in this 2D image plane gives the amplitude of the reflected signal from that position. A 3D reconstruction can be carried out after scanning a volume by longitudinal movement of the US probe or utilizing a fan-like scan while rotating the probe in the rectum. In 3D ultrasound imaging for brachytherapy of prostate, a standard TRUS probe mounted on a motorized stepper unit with precise encoders can be used to obtain a full 3D image reconstruction from the oversampling of overlapping 2D images. After, the obtained dataset can be represented any arbitrary planes with no image degradation (2).

The clinical implementation of US as the imaging modality benefits from its multiple advantages such as the low cost; easy handling; dynamic real-time "live" imaging; no ionizing radiation exposure; high soft-tissue contrast, and high flexibility (2). The US has been successfully applied to position applicator and dose planning for prostate (112), anal (113), and cervix (114) cancers. The catheters positioning in BT treatment for some sites, such as breast (115), head and neck (116), and skin (117), can be carried out under the US guidance (59).

TRUS continues to be the gold-standard imaging modality for prostate HDR-BT (118). TRUS provides an excellent view of the prostate gland (50, 118). Furthermore, TRUS apparatus is less expensive, and smaller, compared to CT and MRI, and it is often widely available in many clinics. TRUS equipment has been integrated into clinical TPSs, such as Oncentra TPS (Elekta Brachytherapy, Veenendaal, The Netherlands), for both LDR- and HDR-BT for the prostate. Owing to the TRUS imaging, a quick, cost-effective, and precise determination of needle implantation in BT is plausible (119, 38). By using TRUS, not only the real-time positioning of the needles (tip) is allowed in 3D, but also identification of the target and OARs is feasible. It has been shown that using only TRUS, catheter insertion, planning, and treatment delivery in the HDR-BT for prostate can be to be finalized in shorter than 90 minutes (50).

In a TRUS-only workflow, the entire procedure, including catheter insertion, implant reconstruction, and treatment planning, is performed under TRUS guidance. Fig. 1.3 shows a TRUS-based technique in which TRUS imaging is used to intraoperatively visualize the insertion of the catheters within the prostate gland. In addition to catheter insertion, dose optimization and treatment delivery can be conducted under TRUS guidance without removing the probe or changing the patient position. By

taking advantages of the TRUS-based images acquired with catheters in place, it is possible to perform real-time planning in a shielded operating room with the patient still under general anesthesia and the US probe in position (inside the rectum). As a result, the risk of catheter displacement caused by the changes in patient position can be neglected, and the planned dosimetry is that delivered (50). After acquiring TRUS images for planning, the dose optimization is performed. During the optimization step, the dwell times are optimized such that the dosimetric constraints are met. Some centers, such as CHU de Québec–Université Laval, use the inverse planning simulated annealing (IPSA) to perform optimization of the treatment plans for HDR-BT for the prostate cancer (85, 120). The description of the dose constraints are included in the inverse planning (IP), and simulated annealing (SA) acts as the optimization engine. IPSA will be discussed in details in 1.1.4. Additionally, dose constraints are provided by the American Brachytherapy Society (ABS) on the target and OARs (68).

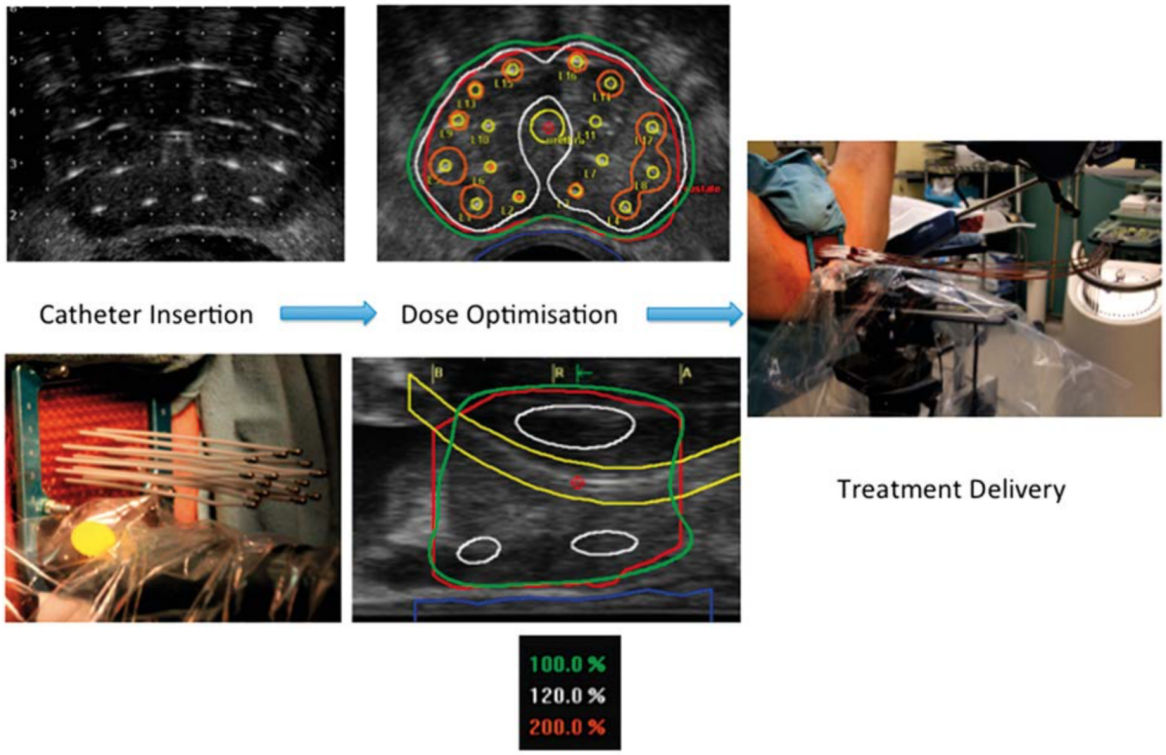

Figure 1.3 – In a TRUS-only workflow for HDR-BT for prostate, the insertion of catheters, optimization of the dwell times, and delivering the treatment are performed under TRUS guidance, with no need for removing the US probe or changing the position of the patient (50).

In the past, the application of the TRUS for planning was complicated for treatments such as the single fraction HDR-BT treatment for prostate cancer. Exact reconstruction of the catheters is substantial for these treatments (121, 122). These complications were related to, for instance, the shadowing of needles' tips, offsets in position caused by bright echoes, and offsets in longitudinal position. Nowadays, however, these deviations are corrected using the following technique (122, 2, 123). For example, the craniocaudal shifts, which was linked to yield shadowing of the needles, can be corrected by measuring the residual needle length adjacent to the template (122). Also, to obtain a precise

spatial identification, the position offsets resulting from the bright echoes, which were shown to be related to the wall of needles rather than their centers, can be corrected. Consequently, TRUS-based imaging can be applied in a single fraction HDR-BT treatment with variations of $\lesssim 2\%$ as compared to CT-based imaging (2, 123).

1.1.2 Brachytherapy TG-43 Dosimetry

A dose calculation formalism for BT treatments, the TG-43 (52), was introduced by the AAPM. Information on the distribution of the absorbed dose in the water surrounding a BT source is provided by TG-43 formalism. Furthermore, in TG-43, the influences of the detailed geometry of a BT source is taken into consideration. Also, the specific design of each BT source is accounted for in the dose-rate constants and other dosimetric parameters applied in the TG-43 formalism (53). As shown in Fig. 1.4, in TG-43 BT dosimetry formalism, the source dose distribution is assumed to be cylindrically symmetric. A polar coordinate system is used with its origin at the center of radioactivity of the BT source. Dose distributions at the point $P(r,\theta)$ are calculated near the source with radial distance r and polar angle θ. r is the distance from the center of the radioactivity of the BT source to the calculation point $P(r,\theta)$. θ is the angle in reference to the long axis of the source (z axis). The selected reference point, $P(r_0,\theta_0)$, is placed on the source transverse plane at a distance of 1 cm from its center, that is $r_0 = 1$ cm and $\theta_0 = 90^\circ$. Also, L represents the active length of the source, and t is the source thickness. β is the angle subtended by active source with respect to the point $P(r,\theta)$, and is given by $\beta = \theta_2 - \theta_1$ (52).

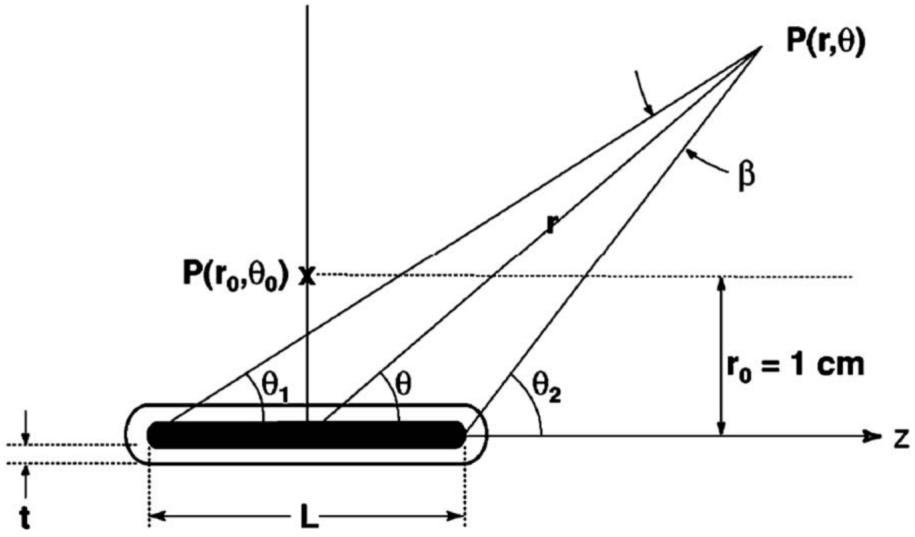

Figure 1.4 – Graphical representation of the geometry used for the TG-43 brachytherapy dose calculation formalism (52).

The 1D or 2D equations to calculate dose rate are provided, respectively, in Eqs.1.1 and 1.2 (11):

$$\dot{D}(r) = S_K \cdot \Lambda \cdot \left(\frac{r_0}{r}\right)^2 \cdot g_P(r) \cdot \phi_{an}(r), \tag{1.1}$$

$$\dot{D}(r,\theta) = S_K \cdot \Lambda \cdot \left(\frac{G_L(r,\theta)}{G_L(r_0,\theta_0)}\right) \cdot g_L(r) \cdot F(r,\theta), \tag{1.2}$$

where the corresponding dosimetry parameters are described in the following. For an extensive description concerning these dosimetry parameters, the reader is refereed to the original AAPM TG-43 article (52), as well as its 2004 update (TG-43U1) (53).

Air-kerma strength, S_K, is a measure of BT source strength and has the units of U=cGy cm^2 h^{-1}. The air-kerma strength is ascertained for specific sources (124). Note that the value of S_K should be traceable to a primary standards dosimetry laboratory (PSDL) such as the National Institute of Standards and Technology (NIST) (125).

Dose rate constant, Λ, is described as the dose rate to water in full scatter condition at a distance of 1 cm on the transverse axis of a, unit air kerma strength, source placed in a water phantom. Dose rate constant has units of cGy h^{-1} U^{-1} and is given as $\Lambda = \dot{D}(r_0,\theta_0)/S_K$. That is, the other dosimetry parameters in Eq.1.2 have values equal to unity at $P(r_0,\theta_0)$ (52). So, by using Λ, the kerma rate in air can be converted to dose rate in water at the reference point $P(r_0,\theta_0)$.

Geometry function, $G(r,\theta)$, deals with the relative dose variations caused only by the spatial distribution of activity inside the BT source, disregarding photon absorption and scattering in the source structure (52). The objective of the geometry function in the clinical BT dose calculation is to enhance the precision of the dose rate estimations by interpolation from data tabulated at discrete points (53). In the case of 1D formalism, which is generally applied in TPSs for LDR low-energy photon-emitting BT using sources such as ^{125}I, the geometry function adopts the simple form of a point-source (i.e., inverse-square approximation). Nevertheless, in the case of 2D formalism, which is generally employed in HDR-BT with high-energy photon-emitting sources such as ^{192}Ir, the distribution of radiation emissions is approximated as a line-segment with length L. The geometry function for the point- and line-source approximations are provided in the Eq.1.3 and 1.4, respectively (53):

$$G_P(r,\theta) = r^{-2} \quad \text{point-source approximation}, \tag{1.3}$$

$$G_L(r,\theta) = \begin{cases} \beta/Lr\sin\theta & \text{if } \theta \neq 0^\circ \\ (r^2 - L^2/4)^{-1} & \text{if } \theta = 0^\circ \end{cases} \quad \text{line-source approximation} \tag{1.4}$$

Radial dose function, $g(r)$, deals with dose fall-off on the transverse plane because of the effects of absorption and scatter in the medium along the transverse axis of the BT source. That is, omitting the dose fall-off included by the geometry function (53). The radial dose function in the case of a point

source is given by $g_P(r) = \dot{D}(r)/\dot{D}(r_0) \cdot (r/r_0)^2$. However, in the case of a line-source, the radial dose function is provided by $g_L(r) = \dot{D}(r,\theta_0)/\dot{D}(r_0,\theta_0) \cdot G_L(r_0,\theta_0)/G_L(r,\theta_0)$ (11).

Anisotropy function, $\phi_{an}(r)$ in Eq.1.1 or $F(r,\theta)$ in Eq.1.2, is used to calculate the dose rate in the transverse plane where dose anisotropy due to the BT sources becomes relevant. In other words, the anisotropy function accounts for the anisotropy of dose distribution around the BT source. This includes the effects of absorption and scatter just in the medium (52).

Then, as given in Eq.1.5, the total dose of each point i in the volume of interest can be obtained by summing the dose contributions related to all the positions j of the source (dwell positions) in all the inserted catheters. For these dwell positions, the stopping time of the source (dwell time) in positions j, t_j, are taken into account. Also, the radioactive decay during irradiation is not considered in Eq.1.5. That is because the treatment time is considered much smaller than the half-life of a BT source in an HDR-BT treatment.

$$D_i = \sum_j \dot{D}(r_{ij},\theta_{ij})\, t_j \tag{1.5}$$

Based on the introduction of the AAPM TG-43 protocol, notable developments in safety, as well as the dosimetric accuracy, of BT treatments have been reported. As a result of using that formalism, developments in the standardization of both dose-calculation techniques and dose-rate distributions in the clinical application of BT have been obtained. For instance, in some BT sources, differences of about 17% were reported between the dose-rate distributions used in the past and those suggested by TG-43 (53). The AAPM TG-43 (52), the 2004 update (TG-43U1) (53), the 2007 supplement (TG-43U1S1) (54), and the 2017 Supplement 2 (TG-43U1S2) (55) have been employed as the basis for BT dose calculation approach in several TPSs.

The TG-43 dosimetry formalism depends on the superposition of single-source dose distributions, which are determined in a liquid water phantom with a fixed volume for radiation scattering (11). Assuming that water is the only medium surrounding the source, the BT source applicators and patient's tissues are not taken into consideration in the AAPM TG-43 formalism. Despite that simplification, the TG-43 approach is still in practice in clinical HDR-BT. That is, firstly, because that photon attenuation and scatter build-up in the patient-specific geometry is usually a second-order effect in respect to the decrease in dose by the inverse-square law (i.e., inversely proportional to the square of the distance from the BT source). Secondly, current methods have been successfully employed long enough to yield much empirical knowledge (2, 16, 19, 20). In recent years, there has been growing interest in methods, such as model-based dose calculation algorithms to be used in clinical BT, that can account for non-water heterogeneities based on patient-specific information provided by 3D images. AAPM report of the Task Group 186 (TG-186) provides a detailed introduction, as well as a review, for these algorithms for BT dose calculations (126). For prostate HDR, TG43 fall within 2% of TG186 thus being a representative case where TG43 approximation is good (127).

1.1.3 Planing and Dose Optimization of an HDR Brachytherapy for Prostate Cancer

The Oncentra Prostate (OcP) TPS (Elekta Brachytherapy, Veneedal, The Netherlands) (128) is used in TRUS-based HDR-BT treatments for the prostate at CHU de Québec–Université Laval. OcP is a real-time intraoperative 3D US, fully integrated for prostate BT (doing both LDR and HDR). In order to acquire the TRUS images, a standard tracked probe stepper unit and a compatible segmentation software are included in the OcP TPS. An image volume reconstructed from sagittal images is used to segment the prostate and adjacent organs. TRUS guidance is used to accurately show the positioning of the implanted catheters within the prostate and to visualize the adjacent OARs. Additionally, using TRUS provides the specification of an optimal plan during the implantation step. Therefore, TRUS allows to carry out the first treatment while the patient is still in the operating room. Consequently, the number of steps in an HDR-BT treatment and the corresponding complexity is reduced. Furthermore, the optimal dose conformity and dose homogeneity are attained. Fig. 1.5(b) shows the 3D real-time reconstruction of the target, OARs, catheters, and source dwell positions obtained by OcP TPS. Also, the isodose distributions for the anatomy-based dose optimization by inverse planning simulated annealing (IPSA) are illustrated respectively in Fig. 1.5(a), (c), and (d) in coronal, axial, and sagittal views, respectively.

The objective of dose optimization in BT, in general, is to produce treatment plans such that a sufficiently high dose of radiation can be delivered to the target while sparing the normal tissues and the neighboring OARs. The optimization problem, which can be addressed using optimization algorithms (86, 85, 129), comprises obtaining the best possible values for the variables associated with the mode of BT under study. *Variables* are defined as the quantities that can be changed using an optimization algorithm. *Parameters* are described as the settings of the algorithm. Then, the quantities that are required to be optimized are known as *objectives*. Moreover, the quantities that represent which combination of variable settings are not permitted is described by *constraints* (2).

Generally, two methods are known for dose optimization in BT: forward (direct); and inverse (indirect) methods. Forward optimization methods are the conventional planning method in which a trial and error approach is applied. First, the parameters judged to be optimal are determined, and subsequently, the dosimetric result is calculated and represented. In other words, planners directly control the variables of the treatment plan in order to adjust the dose distribution. Forwards methods are usually used when the target volumes are defined based on the implanted volumes. As an example, when the regions of interest are not determined, and catheter reconstruction for a volume implant must be done based on the radiographs (2). Inverse methods, however, are the planning method in which the dose objectives for the target volume and OARs, along with factors of importance (i.e., weights) for each of them, are determined. Then, an optimization program is used to determine the treatment parameters. By using the optimization algorithms, the variables of a treatment plan are automatically changed to modify the dose distribution with respect to an "*a priori*" specified dose distribution. The inverse methods are usually applied when the contours associated with the target and OARs of an implant can

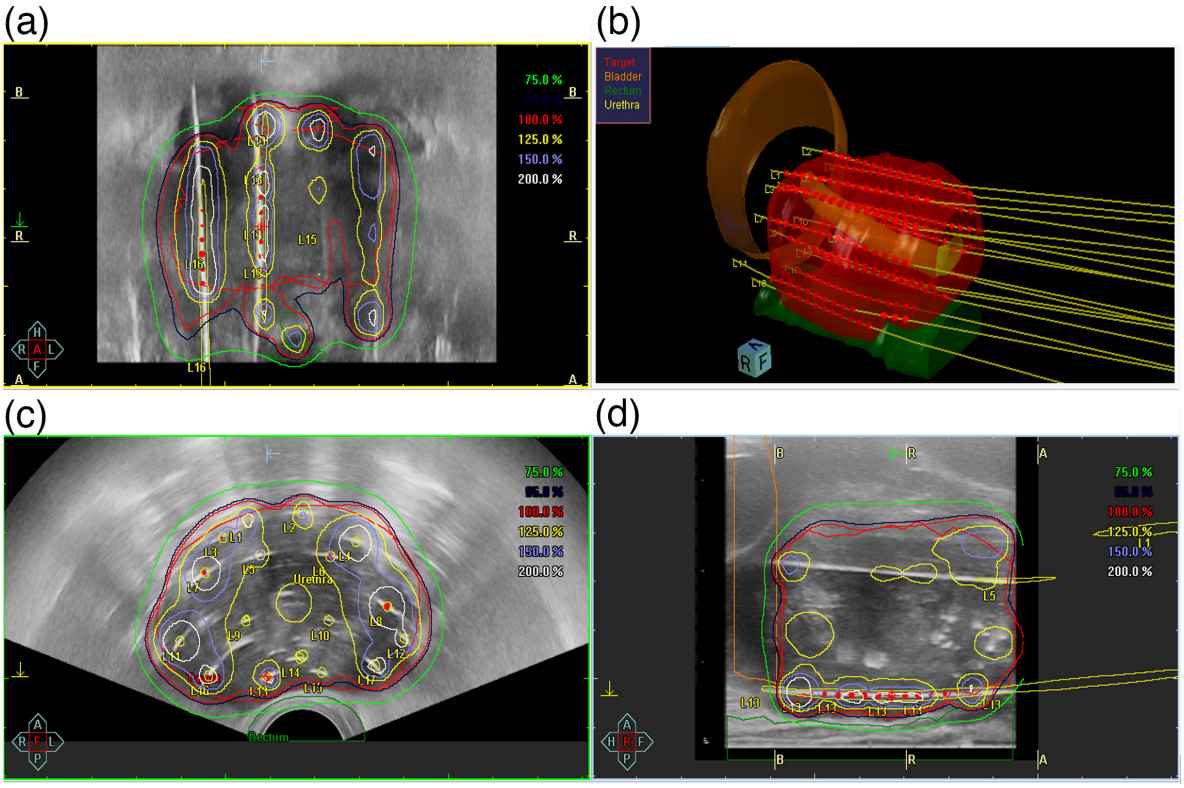

Figure 1.5 – Real-time TRUS-based treatment planning. In (b), the 3D reconstruction of the prostate volume (in red), bladder (in brown), rectum (in green), urethra (in yellow), catheters inserted within the prostate (in yellow lines), and the source dwell positions (in red circles) represented by the OcP TPS. In (a), the coronal, in (c), the axial, and in (d), the sagittal view of the acquired TRUS images are given, along with the corresponding isodose distributions provided by the IPSA dose optimization. The colors representing isodose distributions are green=75%, dark blue=95%, red=100% , yellow=125%, purple=150% , and white=200% .

be acquired using 3D imaging modalities including MRI, CT, and US (2). In the TPS OcP (Elekta, Veneedal, The Netherlands), the inverse planning by simulated annealing (IPSA) and hybrid inverse planning optimization (HIPO) are used software packages built based on inverse optimization methods (86, 87). The optimization algorithms that are based on IPSA (85, 120) and HIPO (130) optimize a total objective function, which is the sum of multiple objective functions. Then, the violation of the upper and lower dose limits in the target and OARs is linearly penalized by each of these objective functions (131). Since IPSA and HIPO methods are appropriate to present "class solutions", they are envisioned as "*a priori*" methods. Class solutions are the solutions that are obtained by employing standard values for dose limits. Note that, since each patient is different, and hence the standard values are rarely precisely correct, patient-specific modifications are needed. That applies mainly in BT treatment planning due to the discrepancy between the conclusive acceptance ROI brought into play by the physicians and the optimization objectives developed and used by the optimization algorithms (2). Additionally, the TPS takes advantage of a postimplant optimization algorithm utilizing an inverse dose-volume histogram-based optimization, DVHO, algorithm. By using DVHO method, the

planner, first, directly define the dose objectives on dose-volume histograms (DVHs) (132). Then, DVHO iteratively minimizes the volume receiving a dose lower than f_L and higher than f_H associated with the target (CTV), the volume receiving a dose higher than f_H for the OARs while taking into account to produce DVHs close to clinical objectives.

In a study, a comparison was performed between the three dose and catheter optimization algorithms for prostate HDR-BT (i.e., IPSA, DVHO, and HIPO). All of these dose optimization engines have demonstrated the capability to provide clinical solutions resulting in nearly similar dosimetric outcomes (132). Nevertheless, IPSA and HIPO were reported to be quicker, less sensitive to catheter placement, and result in a better dose ($D10$) to the urethra as compared to the DVHO. By using IPSA, an optimized plan can be generated under a minute. Additionally, IPSA allows producing plans with great target coverage, low radiation dose to OARs and high dose homogeneity (133, 134). The outcomes of the extensive use of IPSA in clinics were proved its effectiveness (85, 132, 135). A great interest has been given to the development and the application of IPSA, especially in the BT treatment for prostate (86). Note that the clinical HDR-BT treatment plans for prostate used in this research study were all made using IPSA algorithm. Here, IPSA will be discussed.

1.1.4 Inverse Planning Simulated Annealing (IPSA)

IPSA is considered as an anatomy-based algorithm, which optimizes the dwell times using simulated annealing algorithm (136). IPSA was developed for BT application by Lessard and Pouliot (85). IPSA consists of inverse planning (IP), which is an anatomy-based optimization, and simulated annealing (SA), which is a stochastic optimization tool. IP defines the problem in the space of the clinical objectives, including the contour volumes and the dose objectives. The contour volumes consist of targets, OARs, and other potentially necessary volumes. The dose objectives include determining the dose minimum, dose maximum, weights, surface, and volume. By using the SA algorithm, the dwell positions and dwell times are optimized, hence the optimal solution. Consequently, the best treatment plan with respect to the predetermined objectives is obtained.

In order to designate the clinical objectives, in general, one needs to integrate the definitions of the regions of interest (ROIs) with the corresponding dose objectives. The ROIs usually designates the target and the OARs. However, to manage the dose in specific areas in some clinical plans, other ROIs, such as the boost, applicators, and margins, must be designated. After contouring the ROIs, many dose points are automatically generated for each ROI. The dose at each of these points is used to assess a relative penalty in relation to the predetermined dose objectives. Fig. 1.6 represents an example for the dose constraints, in which the dose objectives are exhibited by a dose-penalty graphs. In Fig. 1.6(a), the acceptable range for the dose to target is determined by the inferior limit, the minimum dose (D_{Min}), and the superior limit, the maximum dose (D_{Max}). The D_{Min} limit assures that the minimum dose is covered, and the D_{Max} limit restricts overdose areas. As illustrated in Fig. 1.6(b), the D_{Min} limit is not usually needed for an OAR, but the D_{Max} limit must be established. Simply said,

the optimization process is based on the determination of the D_{Min} and D_{Max} for each of the target and OARs as well as their corresponding weights.

When the dose decreases below the D_{Min} limit, or increases above the D_{Max} limit, the penalty augments at the rates of M_{Min} and M_{Max}, respectively. By modifying M_{Min} and M_{Max} limits, relative importance (i.e., weight) between structures can be set. After setting the dose constraints, the dwell time combination having the smallest penalty value is found by IPSA using the SA algorithm. After the target volumes are delineated and the cost function associated with the dose constraints are established, the IP is run to specify the active dwell positions and to evaluate the dwell times to satisfy the dose constraints (137). The penalty associated with each ROI is a sum of the penalties related to the

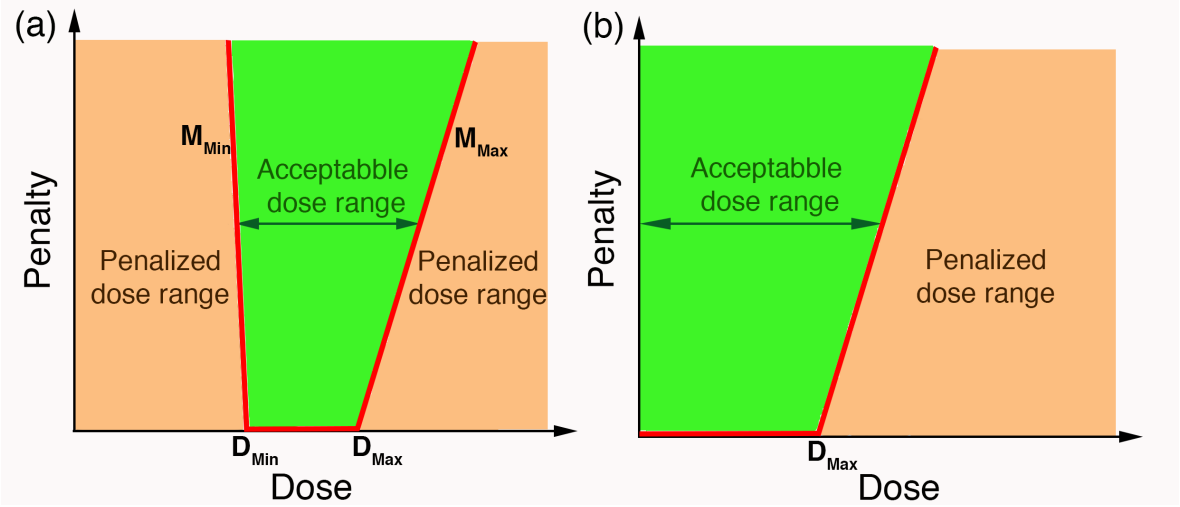

Figure 1.6 – Dose-penalty graphics representing the dose objectives for the target (a) and OARs (b) (138). For the target (a), the lower and upper ranges of acceptable doses are shown by D_{Min} and D_{Max}, respectively. M_{Min} and M_{Max} denote the slope of penalty function for contravening, respectively, the minimum and the maximum dose constraints. For the OARs (b), D_{Min} is rarely needed, and only D_{Max} is set.

dose points at the surface and the points within the volume:

$$P_{ROI} = \sum \text{surface} + \sum \text{volume}. \tag{1.6}$$

The cost function, CF, is the sum of all the penalties related to each dose point for all the ROIs and is given by

$$CF = P_{Prostate} + P_{Bladder} + P_{Rectum} + P_{Urethra} + P_{Boost}, \tag{1.7}$$

where P_x is the penalty for the structure x. Finally, the optimal solution is obtained by finding the minimum value of the cost function. The advantages of IPSA optimization are, but not limited to: taking into account the patient's anatomy, obtaining an optimal dose at the target volume, protecting the OARs, the possibility of controlling the overdosed regions (boost or Dominant Intraprostatic Lesion) based on a biopsy or imaging, having real-time dosimetry in the operating room, and the availability for a fast process (138).

1.1.5 Evaluation of a Brachytherapy Treatment Plan for Prostate Cancer

Definition of the quality of a treatment plan between various physicians and organizations is different (2). If the tumor control probability (TCP) and the normal tissue control probability (NTCP) could have been predicted, the quality of a plan could have objectively been evaluated. Moreover, these objectively evaluated plan quality would have been sufficiently accurate and reliable (15). However, these TCP and NTCP predictions are based on radiobiological modeling. Also, the advancement in the field of radiobiological modeling does not allow yet such precise and reliable predictions (139). Therefore, the TCP and NTCP cannot be used clinically for performing dose optimization using TPSs. Here, criteria that are used for treatment plan evaluation such as isodoses, Dose-Volume Histograms, and dosimetric indices are discussed.

Isodose curves, lines that join points of equal dose, can be used for qualitative evaluation of a plan. These isodose curves can be applied to evaluate treatment plans along with an individual plane or over a number of planes in the patient. The plan can be evaluated by visually examining the isodoses slice per slice. Also, isodoses can be mapped in 3D. Then, the resulting isosurface can be put on a 3D display to represent surface renderings of the target and/or OARs. However, using such displays can neither indicate the distance between the isosurface and the anatomical volume nor obtain quantitative volume information (140).

Quantitative analysis of a treatment plan in BT can be performed based on quality indices such as the Coverage Index (CI), the External Volume Index (EI), the Relative Dose Homogeneity Index (DHI), and the Dose Non-uniformity Ratio (DNR). CI is defined as "the fraction of the target volume that receives a dose equal to or greater than the reference dose (Dref)", $\mathrm{CI} = \mathrm{TV_{Dref}}/\mathrm{TV}$ (141). Another index, EI, is defined as "the ratio of the volume of normal tissue that receives a dose equal or greater than the reference dose to the target volume", EI=$\mathrm{NTV_{Dref}}/\mathrm{TV}$ (141). The next index, DHI, is discussed as "the ratio of the target volume that receives a dose in the range of 1.0 to 1.5 times of the reference dose to the volume of the target that receives a dose equal or larger than the reference dose" (141), $\mathrm{DHI} = [\mathrm{TV_{Dref}} - \mathrm{TV_{1.5\ Dref}}]/\mathrm{TV_{Dref}}$. Subsequently, DNR is defined as the ratio of the target volume which receives a dose equal to or greater than 1.5 times of the reference dose to the volume of the target which receives a dose equal to or greater than the reference dose, $\mathrm{DNR} = \mathrm{TV_{1.5Dref}}/\mathrm{TV_{Dref}}$ (141, 142).

Dose-Volume Histogram (DVH) is a powerful tool for the quantitative evaluation of a treatment plan. DVH is a histogram by which radiation dose is related to the tissue volume. DVH summarizes the information included in the 3D dose distribution and represents the dose received by the volumes, and not by the points (140). Two types of DVH are usually applied. These are the direct DVHs, and the cumulative, also called integral, DVHs. The direct DVHs, also called the differential DVHs, are produced by, first, summing the number of voxels with an average dose within a certain range. Subsequently, the corresponding volume, or more commonly the percentage of the total volume, of an organ is represented with respect to the dose. Based only on the differential DVHs, however, it

is not possible to give a direct answer to questions regarding the quantity of the target coverage by the 95% isodose line. To answer such questions, one needs to evaluate the area under the curve for all the dose levels higher than 95% of the prescription dose. Therefore, cumulative DVHs are more commonly used. The volumes of the target or OARs receiving at least the given dose are calculated in order to plot the cumulative DVHs. Then, this volume in absolute, or more commonly in percentage, is plotted as a function of the dose. Consequently, DVHs allow a quick analysis of the target covering and degree of the sparing of the OARs. Additionally, the quality indices discussed before can be extracted utilizing the DVHs. The volume receiving at least an x percentage of the prescription dose, Vx, and the dose received by an x percentage of the volume, D_x can be obtained. Using DVHs for plan evaluation has advantages such as allowing for the evaluation of volume coverage and overdoses, better judgment on the quality of a plan, the possibility of comparing different plans, as well as being independent of the person responsible for plan evaluation. However, the main disadvantage of DVHs is that the whole anatomical dose distribution is condensed into numbers and percentages data when calculating DVHs.

The dosimetry indices are used, dependent on the treated site, for the BT plan evaluation. In the case of HDR-BT treatment for prostate, the prescription dose must cover more than 95% of the contoured target volume, and at most 1cc of the rectum and bladder should receive 75% of the dose. These dosimetry indices, mostly empirical, come from working groups and research protocols in the form of, for example, AAPM Task Groups. Treatment plan validation in BT is performed using the recommendations provided by the American Brachytherapy Society (ABS) on the target covering and optimization of the dose received by OARs (68). According to the ABS recommendations, V100 > 90%, which indicates the objective of delivering the prescription dose to at least 90% of the CTV. In the case of the OARs, the ABS recommends V75B < 1 cm^3 and V75R < 1 cm^3 for the bladder and rectum, respectively. That means that the volume of the bladder and rectum receiving 75% of the prescription dose should be kept lower than $1cm^3$. Also, in the case of the urethra, the volume of the organ receiving 125% of the prescription dose should be kept lower than $1cm^3$, that is V125U < 1 cm^3 (68). It should be noted that at CHU de Québec–Université Laval, V125 in urethra should be zero. Therefore, ABS recommends a minimal coverage of 90% of CTV while respecting the minimization of the dose on the OARs. Furthermore, Radiation Therapy Oncology Group, RTOG 0924, provides recommendations for dosimetric indices (143).

1.2 Stochastic Frontier Analysis

1.2.1 Frontiers

Multi-objective optimization problems are the ones in which the optimization of more than one objective function is required (144, 145). In these problems, one needs to take optimal decisions while taking into account the trade-offs between two or more conflicting objectives. These problem requir-

ing multi-objective optimization appear, for example, in the business world. Any company desiring to produce a product, henceforth called a producer, is not typically very successful in dealing with these optimization problems. That is because producers are not all technically efficient. Technically inefficient producers are those who fail to employ the minimum needed inputs to produce the chosen output using the available technology. Additionally, even if these producers are technically efficient, they are not all cost-efficient. In other words, they do not assign their inputs in a cost-effective way, given the input prices in hand. Thus, they fail to obtain the minimized expenses needed to produce the desired output to be produced.

In order to avoid these failures in optimization problems, it is necessary to move away from employing traditional functions in the production and cost analyses and to go towards frontiers. A production frontier specifies the minimum input bundles needed to produce the maximum output, or the maximum output producible with a variety of input bundles while considering a fixed technology. Technically efficient producers are defined as these performing on their production frontier, whereas technically inefficient producers are under that production frontier. Furthermore, a cost frontier identifies the minimum expense essential to produce a given bundle of outputs, while taking into account the prices of the utilized inputs and the technology at hand. Cost efficient producers are those functioning on their cost frontier, and cost inefficient producers are functioning above that cost frontier (146).

When functions to analyze the behavior of a producer are reformulated to frontiers, then the symmetrically distributed error terms with zero expectations are not relevant anymore. Due to an unexpectedly favorable operating environment, there is a chance that a producer will find himself above the deterministic kernel of an estimated production frontier or below an estimated cost frontier. However, it is significantly more likely that a producer appears under an estimated production frontier or above a cost frontier. That is because, first of all, if the environmental effects are assumed to be random, then the occurrence of an unfavorable operating environment is as likely as a favorable one. Second of all, a producer might fail to optimize any of the production or cost optimization problems. As a result, error terms related to frontiers are not only comprised of a traditional symmetric random-noise component but also of a new one-sided inefficiency component. Therefore, the error terms corresponding to frontiers are known as "*composed error*" (i.e., two-component error) terms, which are not symmetric and do not have zero expectations. In the case of a production frontier, the error terms are negatively skewed and have negative expectations, whereas, for cost frontiers, the error terms are positively skewed and have positive expectations.

Owing to random variations in the operating environment, the production frontier and cost frontier in the previously mentioned reformulation are stochastic. Also, as a result of various types of inefficiency, deviations from these stochastic frontiers are one-sided. In this field of work, referred to as stochastic frontier analysis, the one-sided error components are introduced to catch the effects of inefficiencies, and to account for the econometric contribution in the production and cost frontier estimations.

1.2.2 Stochastic Frontier Analysis

The stochastic frontier (SF) analysis was initially proposed in economic science by two similar papers in 1977 first by Meeusen and Van den Broeck (88), and a month later by Aigner, Lovell and Schmidt (89). These two papers, and shortly after a third paper by Battese and Corra (1977) shared the "*composed error*" structure, and provided a production frontier model. Their models account for random shocks on the output that is not controllable by producers, as well as the technical inefficiency. The SF model can be expressed as

$$y_i = f(x_i;\beta) + \varepsilon_i,\ i = 1,...,N \tag{1.8}$$

where x_i is a vector of inputs, and y_i is a vector of output, for a firm i. Note that in the optimization of the plans in this work, the inputs are the geometric parameters (GPs) of the patients and the output are their dosimetric parameters (DPs) of interest. Additionally, the production frontier is defined for the DP V100 of the prostate. Furthermore, the cost functions are determined for the DPs such as V75 of the bladder, V75 of the rectum, and D10 of the urethra. Also, β in Eq.1.8 is a vector of technological parameters to be ascertained. In this study, β defines the weights on the GPs of the patients. The "*composed error*" term, ε_i, for the production frontier model is given by

$$\varepsilon_i = v_i - u_i,\ i = 1,...,N \tag{1.9}$$

where i represents the firm, or in our study, the plan. The first error component, v_i, accounts for the impacts of statistical noise, or symmetric disturbance. It corresponds to uncontrollable factors in a company that can affect its productivity. For example, the price of raw materials, the temperature, or chance. In the context of our research, that random term includes all random variables that can affect the sparing of the OAR, positively or negatively. Since that error component can increase or decrease productivity, it can shift the company above or below its production frontier, respectively. Therefore, as shown in Fig. 1.7(a), the error term associated with the random errors follows a symmetric standard, normal (i.e., two-sided), distribution (147). Furthermore, v_i describes a degradation with a stochastic origin.

The second error term given in Eq.1.9, u_i, deals with the effects of technical inefficiency. u_i corresponds to the controllable factors in a company, for instance, the expertise of the employees, that can influence its productivity. Within the framework of our research, u_i can be associated with the efficiency of the treatment planner, as well as the competency of the medical physicists and the oncologist. That error component only reduces the productivity of a company. Thus, it follows an asymmetric half normal (i.e., one-sided) distribution (147). In our work, the inefficiency term affects the dose to the OARs negatively. On another note, u_i is the degradation with a deterministic origin.

Note that the normal (N)-half normal (N^+) model is utilized to describe the degradation, in which the corresponding distributional assumptions are $v \sim N(0,\sigma_v^2)$ and $u \sim N^+(0,\sigma_u^2)$. v and u are distributed independently of each other and of the regressors (146) .

As $u_i \geq 0$, the error term ε_i in Eq.1.9 is asymmetric. Beside that, u_i is supposed to be distributed independently of v_i. As demonstrated in Fig. 1.7(b), a case with u_i following a positively truncated normal distribution ($u \sim N^{+}(0, \sigma_u^2)$) is studied. If u_i=0, Eq.1.9 converts to $\varepsilon_i = v_i$. The error term is symmetric, and the data shows no sign of technical inefficiency. However, if $u_i > 0$, Eq.1.9 is negatively skewed, and the data contains technical inefficiency. In Fig. 1.7(c), the superposition of

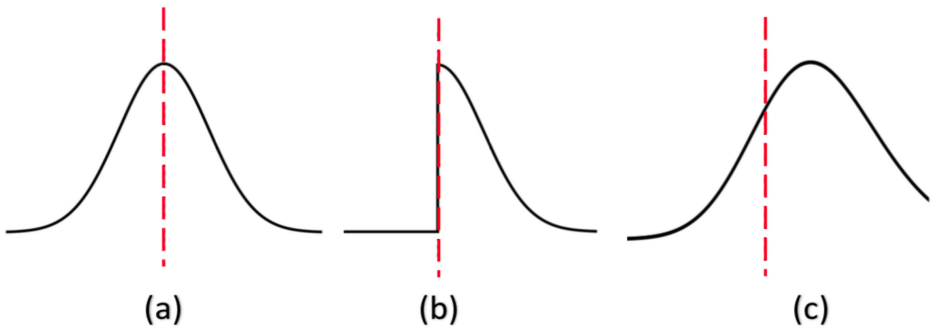

Figure 1.7 – Graphical representation of the superposition of the two components of the composed error term. A random error component in (a) combined with the error component related to technical inefficiency in (b) created a composed error term in (c). The red dashed lines represent the corresponding frontiers.

the two, previously stated, distributions: the normal distribution and the positively truncated normal distribution is exhibited. That superposition is given by

$$g(\varepsilon_i) = \frac{2}{\sigma} \cdot f^*\left(\frac{-\varepsilon_i}{\sigma}; 0; 1\right) \cdot \left[1 - F^*\left(\frac{-\varepsilon_i \lambda}{\sigma}; 0; 1\right)\right], \tag{1.10}$$

where $f^*(\cdot)$ is the standard normal density function, and $F^*(\cdot)$ is the cumulative distribution function of the standard normal density function. In addition, $\sigma^2 = \sigma_u^2 + \sigma_v^2$, where σ is the width of the distribution. Furthermore, $\lambda = \sigma_u/\sigma_v$ represents the asymmetry of the distribution. Having that in mind, λ can be seen as a measure of the relative variability of the two sources of error that can tell apart a company from the others. If $\lambda^2 \to 0$, then $\sigma_v^2 \to \infty$ and/or $\sigma_u^2 \to 0$. In that case, the dominant error component in evaluating ε would be the symmetric degradation, whereby Eq.1.10 takes on the form of the density of a $N(0, \sigma^2)$ random variable. Therefore, the frontier is a simple regression. However, in case that $\lambda^2 \to \infty$, $\sigma_v^2 \to 0$, the one-sided error component would be the dominant source of random variation. in that scenario, the degradation is of deterministic origin, the frontier has a deterministic characteristic. Then, Eq. 1.10 takes on the form of a negatively truncated normal distribution, hence an absolute frontier (89).

It is to be noted that the density $g(\varepsilon_i)$ in Eq.1.10 is asymmetric around zero. The corresponding expectation and variance of that density is provided, respectively, by

$$\begin{aligned} E(\varepsilon) &= E(u) = -\frac{\sqrt{2}}{\sqrt{\pi}}\sigma_u, \\ V(\varepsilon) &= V(u) + V(v) = \left(\frac{\pi - 2}{\pi}\right)\sigma_u^2 + \sigma_v^2. \end{aligned} \tag{1.11}$$

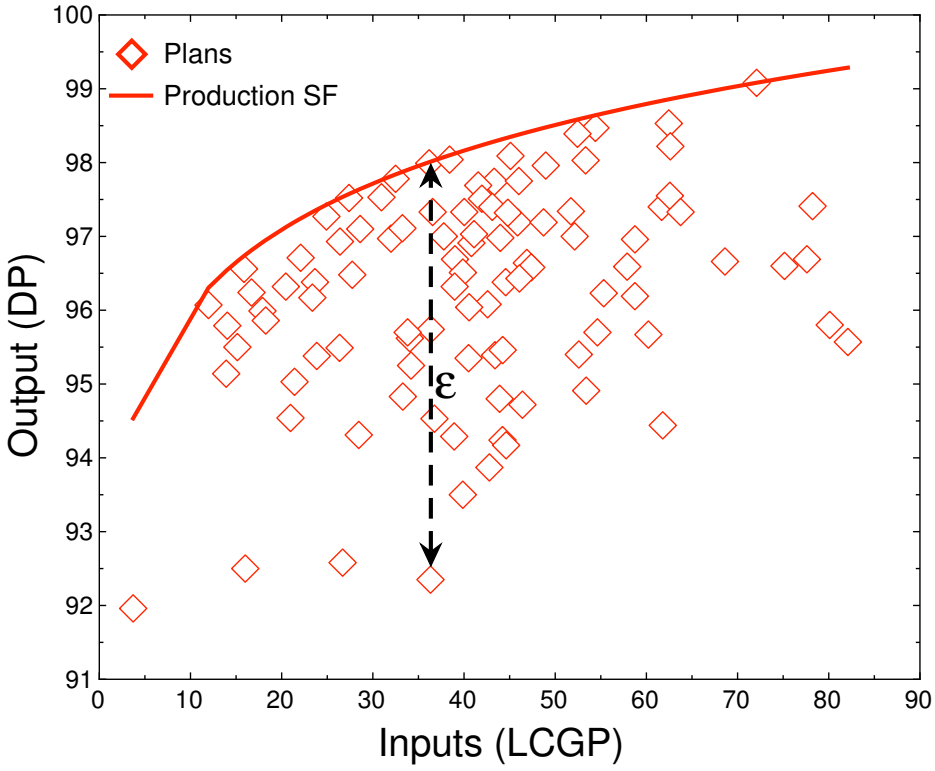

Figure 1.8 – Illustration of a production stochastic frontier (solid line) developed for a number of clinical HDR-BT treatment plans (empty diamonds) for prostate cancer. The output, the dosimetric parameter (DP) of interest, is shown as a function of the inputs. The inputs are the linear combination of all the geometric parameters (LCGP). ε (dashed line) provides the difference between each plan and the frontier.

Additionally, in order to obtain the equations for cost frontier, one can simply substitute ε by $-\varepsilon$ in Eq.1.10, and Eq.1.11. Also, the error term associated with a cost frontier is obtained by changing the sign in Eq.1.9 such that $\varepsilon_i = v_i + u_i$.

In economics, the most commonly used analytical form of the function $f(\cdot)$ in Eq.1.8 is perhaps the Cobb-Douglas function (148). Not only the Cobb-Douglas form has been employed several times in different areas in economics, but it has also found its place in other fields such as frontier production functions (149). To discuss the Cobb-Douglas function, suppose a situation in which we are dealing with a single good with only two inputs: the total number of person-hours worked in a period of time, L, and the real value of all equipment, K. In that simple case, the Cobb and Douglas function is given by $Y = AL^{\gamma}K^{\beta}$, where Y is the total production, A is the total input productivity. Also, γ and β are the output elasticities of K and L, denoting the measures of the output responsiveness to a change in the either K or L levels used in production. In situations where the corresponding models comprise more than two goods, the Cobb-Douglas function needs to be generalized, which is given by

$$f(x) = A\prod_{i=1}^{n} x_i^{\alpha_i}. \tag{1.12}$$

In Eq.1.12, A is the efficiency parameters ($A > 0$), n is the total number of goods, $x_1, \cdots, x_n$ are the quantities of goods consumed, produced, etc, and α_i is an elasticity parameter for good i ($\alpha_i \in \Re$) (148).

Additionally, the Cobb-Douglas function can be simplified to a linear relationship. That is $x_1, \cdots, x_n$ in Eq.1.12 can be substituted by the linear combination of all the geometric parameters (LCGP) of interest. Therefore, Eq.1.12 can be simplified to

$$f(x_i, \beta) = a_0 + a_1 \ln \sum_{i=1}^{n} \beta_i x_i, \tag{1.13}$$

where f(·) is the output, x_i are the inputs. β_i is the weight over the geometric parameter i. Also, a_0 and a_1 are the model coefficients (146). For the sake of an easier visualization of the results in a 2D graphic, Eq.1.13 was transformed to its simplified form in Eq.1.12. Furthermore, the maximum likelihood technique coupled with simulated annealing can be exploited in the optimization procedure to obtain the parameters associated with the frontier under study.

SFA has been used before in our research group for radiation therapy treatment planning. The results of these efforts on the application of SFA in RT planning have been published recently in two peer-reviewed manuscripts (150, 151). In the first publication by Angelika Kroshko et al. (150), SFA was utilized to build a predictive model of dosimetric features from GPs associated with patient anatomical information. In that study, a group of patients who were treated in the past for prostate cancer using the volumetric modulated arc therapy (VMAT) was investigated retrospectively. Seven GPs were taken into account to study the relationship between the OARs (i.e., the bladder and the rectum) and the planning volume (PTV). Also, 37 DPs were examined for the bladder and the rectum. SFA was used to assess the minimum achievable dose to the bladder and the rectum based on the GPs. The maximum likelihood estimation technique was exploited to determine the optimum stochastic frontiers minimizing the dose to the bladder and the rectum. In the second publication by Paul Edimo et al. (151), SFA method was used to develop patient-specific unbiased quality control models for dose prediction for CT-based HDR-BT plans for prostate cancer. To build those models, CT-based HDR-BT plans for prostate cancer were used, in which the patients were treated using a single fraction of 15 Gy preceded by EBRT. Moreover, IPSA algorithm in the Oncentra TPS (Elekta—Brachy, Veenendaal, The Netherlands) was employed to perform the optimization process of DPs of BT boost treatment of those patients. Relationships between eight GPs and four DPs, V100 (CTV), V75 (bladder and rectum), and D10 (urethra), were studied. The maximum likelihood technique was utilized to estimate the model parameters using a Generalized Simulated Annealing (GenSA) algorithm implemented in R statistic package. Here, in this research study, we also use the maximum likelihood implemented in the statistical computing package R (152), as well as its GenSA algorithm (153) in optimization of prostate HDR-BT plans, which will be discussed here.

1.2.3 Maximum Likelihood for Optimization

To describe the likelihood function, suppose a random variable, X, with its probability density being dependent on some unknown parameter θ. The objective is to come up with a point estimator $u(X)$ such that $u(x_1,x_2,\cdots,x_n)$ is a good point estimate of θ. $x_1,x_2,\cdots x_n$ are the observed values of the random variable. A good estimate of θ is the value of θ that maximizes the likelihood of obtaining the observed data. That is the maximum likelihood method. In practice, if the probability density function of each X_i in the random sample is given by $f(x_i;\theta)$, then the joint probability density of X is provided by

$$P(X) = f(x_1;\theta)\cdot f(x_2;\theta)\cdots f(x_n;\theta), \tag{1.14}$$

where the equality is due to having a random sample and hence the independency of the X_is. Consequently, the likelihood function, $L(\theta;\varepsilon)$, is given by

$$L(\theta;\varepsilon) = \prod_{i=1}^{n} f(x_i;\theta),\ \varepsilon = [x_1,x_2,\cdots,x_n] \tag{1.15}$$

Given that L is maximal at the point where the observations x_i are more probable, the values of the parameters maximizing that function need to be found. To be brief, one must first choose a model with one or more unknown parameters for a set of data. Then, the maximum likelihood measurements aim to maximize the likelihood function, hence to maximize the agreement between the model and the data. In practice, the logarithm of the L function is used to obtain the value of the parameters maximizing that function. That is due to the complexity in differentiating the products of n parts in Eq. 1.15. Therefore, the log-likelihood, $\mathscr{L}$, is given by

$$\mathscr{L} = \ln\left(L(\theta;\varepsilon)\right) = \sum_{i=1}^{n} \ln f(x_i;\theta). \tag{1.16}$$

By substituting $f(x_i;\theta)$ in Eq.1.16 with its equivalent given in Eq.1.10, the $\mathscr{L}$ function, applicable in the stochastic frontier model, is obtained as

$$\mathscr{L} = \sum_{i=1}^{n} \ln\left(\frac{2}{\sigma}\cdot f^*\left(\frac{-\varepsilon_i}{\sigma};0;1\right)\cdot\left[1-F^*\left(\frac{-\varepsilon_i\lambda}{\sigma};0;1\right)\right]\right). \tag{1.17}$$

As will be discussed in 2.4, the optimization of the SF models are performed using the maximum likelihood, or equivalently log-likelihood (MLL) implemented in R as well as its GenSA algorithm. Additionally, in order to obtain physically meaningful results for the optimization of the parameters associated with the stochastic frontier model under study, physical constraints such as $\sigma_u \geq 0$ and $\sigma_v \geq 0$ need to be imposed. Also, since different linear combinations of the geometric parameters are possible, a tool to ascertain the appropriate model generating the optimal stochastic frontier with the minimum number of parameter is required. That is done by means of the likelihood (or equivalently log-likelihood) ratio test (LRT) (154). LRT reveals how many times more likely the data is controlled by one model rather than the other model. The two competing statistical models are usually referred

to as the null model (i.e., the simple model) and the alternative model (i.e., the general model). The null model is the one having fewer parameters ($n-i$ parameters) as compared to the alternative model (n parameters). Then,

$$\begin{aligned} D &= 2\left[\ln\left(L_{alt}(\theta)\right) - \ln\left(L_{null}(\theta)\right)\right], \\ &= -2\ln\left(\frac{L_{null}(\theta)}{L_{alt}(\theta)}\right), \end{aligned} \tag{1.18}$$

where $L_{null}(\theta)$ is the maximum log-likelihood (MLL) of the null model, $L_{alt}(\theta)$ is the MLL of the alternative model, and $L_{null}(\theta)/L_{alt}(\theta)$ is the ratio of the two MLLs. Wilks (1938) (155) demonstrated that as size of the sample approaches infinity ($n \to \infty$), the D for a nested model (i.e., the model that is the subset of another model) will takes, asymptotically, the form of a chi-squared distribution with df degrees of freedom, assuming that the null model is true. Degrees of freedom, here, is defined as the difference between the number of the free parameters of the alternative model and the null model, $df_{alt} - df_{null}$. The MLL ratio can be computed for the data associated with a large range of models. The ratio in Eq.1.18 is compared with the chi-squared value of the determined statistical significance in order to obtain an approximate statistical test. Statistical significance is used to find out whether the null model should be selected or rejected. Significance level (α) is the probability of rejecting the null model, given that the null model is true. Additionally, p-value (p) is defined as the probability of getting a result at least as extreme as that observed, given that the null model is true. If the p-value associated with a result is less than the pre-determined significance level, $p < \alpha$, then that observed result is statistically significant, and the null model should be rejected. Drawing data from a sample, there is always the chance of obtaining a result only due to a sampling error. On the other hand, when the p-value of a result is equal to or larger than the chosen significance level, the result denotes the characteristics of the entire sample; thus, the null model should be kept. In literature, the significance level is usually set to $\alpha = 0.05$ (or smaller). Alternatively stated, when drawing data from a sample, the rejection region consists of 5% (or smaller) of the sampling distribution (154).

In this work, a large number of models comprising a variety of possible combinations of GPs are studied. Different models are compared: the null model having less GPs and the alternative model with more GPs. Every two competing models are independently fitted to the corresponding data, and their associated MLL values are evaluated. Then, to establish whether or not the fit obtained based on the alternate model is significantly better than the one for the null model, the probability or p-value associated with the difference given in Eq.1.18 is calculated. Because the null model is a specific case of an alternative model, the probability distribution of the MLL ratio statistic can be assessed, approximately, as the chi-squared distribution with df degrees of freedom. df is the difference between the number of GPs in the alternative and null models. Having set the significance level $\alpha = 0.05$, in case of p-value< 0.05, the null model should be rejected. Conversely, if p-value> 0.05, the alternative model is rejected. Consequently, it is determined which model, the null or alternative, should be opted for the data under study. Following the same procedure, a PSF model for the target and a CSF model for each of the bladder, rectum, and urethra is developed. It is to be noted that an enormous

number of SF models for each of the production functions or cost functions are possible each with a different number and/or kind of the GPs. However, to ensure to not include GPs with an insignificant effect on the DP of interest, and in turn, to save effort and time by avoiding excess computations, the dominant GPs need to be found for each of the target PSF, and the bladder, rectum, and urethra CSF models. On that account, a nonparametric approach, namely the Spearman correlation coefficient, can be exploited to measure the monotonic relationships between the GPs and each DP of interest. In the following section, the Spearman correlation coefficient will be concisely studied.

1.3 Spearman Correlation Coefficient Method

To measure the strength and the direction of a relationship between two variables, in our case a GP and the DP of interest, a bivariate analysis called correlation is used. Methods such as Pearson's correlation (156) are satisfactory to measure the relationship between variables only in data-sets showing a strong linear relationship. In order to avoid falling into these limited methods, a nonparametric approach is needed. This nonparametric approach should not assume a particular probability distribution. Therefore, the Spearman correlation coefficient (SCC), also called Spearman rho, can be used (157). SCC is a nonparametric measure of the statistical dependence between the rankings of two variables (rank correlation). As opposed to Pearson correlation, normality is not required, hence the Spearman correlation is considered as a nonparametric statistic. Measuring the monotonic relationship between variables yield SCC to be more reliable than other methods even if that relationship is not strongly linear. Fig. 1.9(c) and (d) represents a non-monotonic relationship between two variables in the two examples. However, Figs. 1.9 (a) and (b) (158) show a monotonic relationship, in which by increasing the magnitude of one variable, the magnitude of the other variable increases (Fig. 1.9 (a)) or decreases (Figs. 1.9 (b)). In other words, in a monotonic relationship, a dependent variable is always decreasing or increasing (whether linear or not) as its independent variable increases. Therefore, the variables tend to move in the same relative direction, but not necessarily at a constant rate. Consequently, the monotonicity is less restrictive than that of a linear relationship. Furthermore, due to limiting the outlier to the value of its rank, the Spearman correlation is less sensitive to strong outliers as opposed to the Pearson correlation.

As mentioned above, the SCC measures the strength and direction of the monotonic relationship between two ranked variables. In cases when each of the two variables is a perfect monotone function of the other variable, even if their relationship is not linear, a perfect SCC equal to $+1$ or -1 is obtained. The direction of the relationship between the independent variable and the dependent variable is discerned by the signs $\pm$ of the SCC. An increasing and a decreasing monotonic trend between two variables yields a positive and negative SCC, respectively. A correlation coefficient equal to 0 signifies the absence of correlation between the two variables under study. Put it briefly, the SCC, r_s, is constrained as $-1 \leq r_s \leq +1$. Furthermore, suppose a number of observations (i.e., n). In order to obtain r_s, the n raw scores X_i and Y_i are converted to ranks $\mathrm{rg}X_i$, $\mathrm{rg}Y_i$. Since the SCC can be expressed

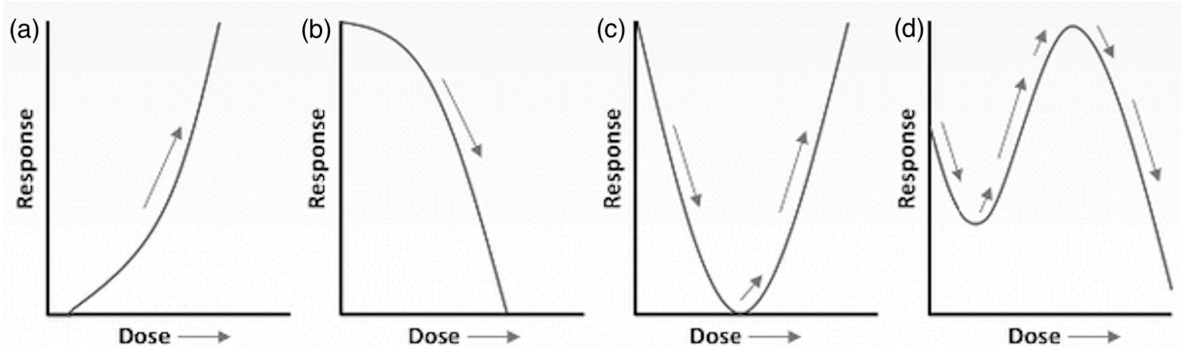

Figure 1.9 – Examples of monotonic relationships between two variables in which as one variable increases the other variable either increases (a) or decreases (b). Examples of non-monotonic relationships are presented in (c) and (d) (158).

as the Pearson correlation coefficient but applied to the ranked variable (ρ_{rg_X,rg_Y}), r_s can be given by (157)

$$r_s = \rho_{rg_X,rg_Y} = \frac{cov(rg_X, rg_Y)}{\sigma_{rg_X}\sigma_{rg_Y}}, \tag{1.19}$$

where $cov(rg_X, rg_Y)$ is the covariance, and σ_{rg_X} and σ_{rg_Y} are the standard deviations of the rank variables.

In case of dealing with data with no ties, i.e. when all n ranks are distinct integers, the SCC can be evaluated using the following formula:

$$r_s = 1 - \frac{6\sum d_i^2}{n(n^2-1)}, \tag{1.20}$$

where n is the number of observations, and $d_i = rg(X_i) - rg(Y_i)$ is the difference between the two ranks of each observation.

Chapter 2

Materials and Methods

2.1 Data Collection and Evaluation

To construct the models and to develop the CTV and OARs frontiers, a sample set consisting of 100 patients were used. Patients were all treated with HDR-BT prostate cancer in CHU de Québec–Université Laval. All patients were prescribed a single fraction of 15 Gy. Moreover, the IPSA optimizer, implemented in the Oncentra Prostate (OcP) TPS, was employed to perform the dose optimization for the patients. By using the OcP TPS, the dosimetric parameters (DPs) of interest were extracted for the CTV and the OARs, as will be discussed in section 2.2. The DPs were obtained based on the clinical contours for CTV and OARs saved in OcP. Additionally, four geometric parameters (GPs), volumes of the contoured structures (one CTV and three OARs), were extracted from OcP.

To extract the DPs of interest as well as the volumes of the contoured structures from the OcP TPS, the DICOM files of all the patients were manually imported into OcP. RTSTRUCT stores contour information. Note that the optimization contours such as "couv" and "evit" of some patients were not considered in our study since their purpose is only to help the inverse optimizations to have the best covering of the CTV and the least dose at OARs. Moreover, the "Bladder-Neck" contour is not taken into account as a parameter in this study because the guidelines for this organ is not known, and hence the associated contour is not included in the clinical optimization process.

The RTPLAN files stock information related to the inserted catheters and the radioactive source that was employed. Furthermore, the data associated with the dose of the CTV and OARs and the associated isodoses is stored in the RTDOSE. The "Dose Evaluation" tool was used to calculate the DVH of a selected RTPLAN. Further, the number of sampling points in the DVH Calculation settings was increased to 20,000 points to improve the precision of DVH. RTSTRUCT and RTPLAN will be needed by our QC tool and exported to it.

A software called "3D Slicer" was used to evaluate 95% confidence interval, max and mean of Hausdorff distances, as will be discussed in 2.3.2. 3D Slicer is an open source software with numerous

powerful plug-in for image-guided therapy research (159). Additionally, the GPs of the ratio of the number of catheters and maximum surface of the prostate, the ratio of the area enclosing all the catheters and maximum surface of the prostate, the average distance between all the catheters, and the minimum distance between the active points of the lowest catheters and their closest points on the midplane and also full length of the rectum were calculated by a series of Python codes.

2.2 Dosimetric Parameters

The DPs taken into account in this study are chosen based on the ABS (68, 19, 160) and RTOG 0924 (143) recommendations. The ideal objective is to deliver the prescribed dose only to the CTV. The DPs associated to the CTV is V100. Also, in the case of the OARs, such as bladder and rectum, the DPs are V75B and V75R, respectively. As discussed in 1.1.5, the ABS recommendations for the CTV is V100 > 90%, for bladder V75B < 1 cm^3, for rectum V75R < 1 cm^3, and for the urethra V125U < 1 cm^3 (68). So, ABS recommends a minimal coverage of 90% of CTV while respecting the minimization of the dose on the OARs. Note that V125 and V130 were not considered as DP since they were 0 for all patients; a hard constraint defined at CHU de Québec–Université Laval. The DPs of interest in this work are listed in Table 2.1.

Table 2.1 – DPs and their associated structure of interest.

DPs	**V100**	**V75B**	**V75R**	**D10U**
Structure of interest	Target (CTV)	Bladder	Rectum	Urethra

2.3 Geometric Parameters

In addition to the DPs of interest discussed before, the GPs must be determined to carry out the SFA. The GPs taken into account in this study included those associated with patients, those related to the implanted catheters, and a mix of these GPs. The GPs related to patients are the volume of the prostate (CTV) and OARs and the Hausdorff distance between the prostate and the OARs. The GPs related to catheters are the ratio of the number of catheters and the maximum surface of the prostate, the ratio of the area enclosing all the catheters and the maximum surface of the prostate, and the distance between all the catheters. Furthermore, the average of the minimum distance between the dwell positions on the two catheters closest to the rectum and their closest points on the rectum were measured. Those measurements were performed for the midplane and also full length of the rectum and, accordingly, were considered as two GPs in our study. The GPs studied in this research are listed in Table 2.2 and are discussed in the following subsections.

Table 2.2 – GPs of interest and the corresponding abbreviations. X showed in the Hausdorff distances (HDs) corresponds to the bladder, rectum, and urethra.

Patient GPs (Volumes)	**VCTV**	**VB**	**VR**	**VU**	
Description	CTV volume	Bladder volume	Rectum volume	Urethra volume	
Patient GPs (HDs)	**HMX**	**HAX**	**H95X**		
Description	Hausdorff distance between the prostate and the maximum volume of the X	Hausdorff distance between the prostate and the average volume of the X	Hausdorff distance between the prostate and the 95% volume of the X		
GPs Catheters	**GPC1**	**GPC2**	**GPC3**	**GPC4**	**GPC5**
Descriptions	The ratio of the number of the implanted catheters and the maximum surface of the prostate	The ratio of the area enclosing all the implanted catheters and the maximum surface of the prostate	The average distance between all the implanted catheters	The minimum distance between the active points of the catheters implanted in the lowest portion of the prostate and their closest point on the half length of the rectum	The minimum distance between the active points of the catheters implanted in the lowest portion of the prostate and their closest point on the half length of the rectum

2.3.1 Volume of the Contoured Structures

The volumes associated with different contoured structures in an HDR-BT treatment for prostate cancer are considered as four GPs to evaluate the SFs. The volume measured from the DICOM contours directly. These contoured structures consist of the target (CTV) and OARs including the bladder, rectum, and urethra.

2.3.2 Hausdorff Distances

In addition to the volumes of the four contoured structures, the GPs representing the distances between the CTV and three OARs could be considered. However, by considering only the shortest distance between two regions, very little information is captured. Indeed, the shortest distance is entirely independent of the shape of each of the regions under study, and also, the shortest distance does not take the position of the objects into consideration. Therefore, the concept of Hausdorff distance (HD) (161, 162) was chosen to overcome the previous limitation. HD is defined as the maximum distance of a set X to the closest point in the other set Y, as shown in Fig. 2.1. In other words, HD is the worst-case distance between two regions under measurement. The distances between all the points in a volume X to the closest point in the volume Y are computed. Then, the maximum of those closest distances yields the HD, which is given by

$$h(X,Y) = \max_{x \in X} \min_{y \in Y} d(x,y). \tag{2.1}$$

Note that asymmetry is the characteristic of maximum functions, and minimum functions are symmetrical. Therefore, the HD has asymmetrical properties, and hence, $h(X,Y)$ is not always equal to $h(Y,X)$. A more general form of HD is defined as the maximum of the two directed HDs (undirected

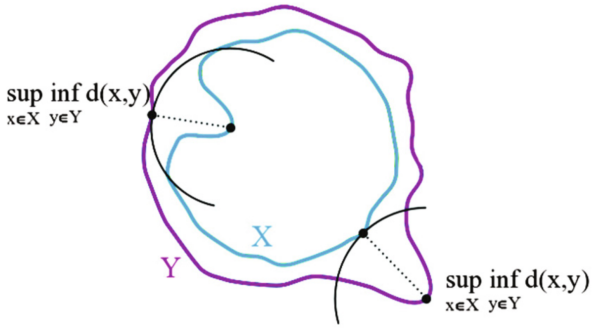

Figure 2.1 – Illustration of the Hausdorff distance between region X and region Y. "sup" indicates the supremum and "inf" the infimum (163).

HD), which is given by

$$H(X,Y) = max\left\{h(X,Y), h(Y,X)\right\}. \tag{2.2}$$

Note that $h(X,Y)$ in Eq.2.1 is the HD "from" X to Y, namely direct HD, however $H(X,Y)$ in Eq.2.2 is "between" X and Y, namely undirected HD. In addition, the average distance of a point in the set X to its closest point in the set Y is defined as the directed average HD, as written in the following equation

$$h_{ave}(X,Y) = \frac{1}{|X|}\sum_{x\in X}\min_{y\in Y} d(x,y). \tag{2.3}$$

Also, the average of the two directed average HDs yields the (undirected) average HD as

$$H_{ave}(X,Y) = \frac{h_{ave}(X,Y) + h_{ave}(Y,X)}{2}. \tag{2.4}$$

Furthermore, the maximum of the two directed average HD measures give rise to the (undirected) maximum average HD measure as

$$H_{max_{ave}}(X,Y) = max\left\{h_{ave}(X,Y), h_{ave}(Y,X)\right\}. \tag{2.5}$$

Moreover, by evaluating the pth percentile distance over all distances from points in X to their nearest point in Y, the directed percent HD is measured for a percentile of p and is provided by

$$h_p(X,Y) = K_p\left(\min_{y\in Y} d(x,y)\right) \forall x \in X, \tag{2.6}$$

where K_p is the pth percentile. Finally, the (undirected) percent HD measure is given by the mean as

$$H_p(X,Y) = \frac{h_p(X,Y) + h_p(Y,X)}{2}. \tag{2.7}$$

In this study, the directed 95% HD is considered, which is the point in X with a distance to its nearest point in Y that is larger or identical to precisely 95% of the other points in X.

Bear in mind that in the literature, the undirected HD is referred to as HD (161, 162).

The HDs studied include the HD between the CTV and bladder, CTV and rectum, and CTV and urethra. Although the (undirected) maximum HD is usually considered as an appropriate measure when comparing two volumes, it is an inadequate measure in the case of prostate HDR brachytherapy treatment. Indeed, the distance between the rectum and the prostate would have a more significant impact on the dosimetry when the distance is narrow over an extended length of the rectum instead of a short length. For this reason, the mean HD, and the percent HD (for a percentile 95%) are used in addition to the (undirected) maximum HD. Therefore, a more extensive study of the impact of the rectum-prostate distance on the dosimetry is allowed. A total of nine HDs were employed as GPs to evaluate the stochastic frontiers. The HDs between the CTV and the maximum, mean, and 95% volume of the OARs of every patient can be assessed using the "Segment Comparison" module in 3D Slicer, which provides comparison metrics for segments (i.e., contours, structures). However, to make the calculation process more efficient, a Python code was developed to be used in the Python console of the 3D Slicer to calculate all the required HDs.

2.3.3 Ratio of the Number of the Implanted Catheters and the Maximum Surface of the Prostate

An average of 17 catheters was inserted into the prostate gland under ultrasound guidance in this study. Nevertheless, in some cases between 14 and 22 catheters were used. The number of inserted catheters in a prostate HDR-BT treatment is an interesting parameter which could impact the dosimetry. Therefore, a new GP was studied by evaluating the ratio of the number of catheters and the maximum surface of the prostate. The total number of inserted catheters for each patient was extracted from the DICOM file imported in the OcP TPS.

The volume and the shape of the prostate were considered in the evaluation of its maximum surface. As shown in Fig. 2.2(a), the contour of the prostate was extracted from the DICOM file of each patient. Subsequently, as shown in Fig. 2.2(b), all those contour points were superposed on the xy-plane (2D), and the points constructing the maximum surface for a given angle were selected.

2.3.4 Ratio of the Area Enclosing All the Implanted Catheters and the Maximum Surface of the Prostate

In addition to the number of catheters inserted within the prostate gland, the way those catheters fill the space of the prostate could influence the dosimetry. Accordingly, another GP is proposed which gives the ratio of the area enclosing all the inserted catheters and the maximum surface of the prostate. The maximum surface of the prostate is the same as that used in the previous subsection 2.3.3. A Python code was developed to calculate the area enclosing all the catheters. As shown in Fig. 2.3(a), the 3D coordinates (xyz) of the dwell positions of all the inserted catheters were obtained. Subsequently, as illustrated in Fig. 2.3(b), the dwell positions are superposed on a 2D plane (xy-plane). Afterward,

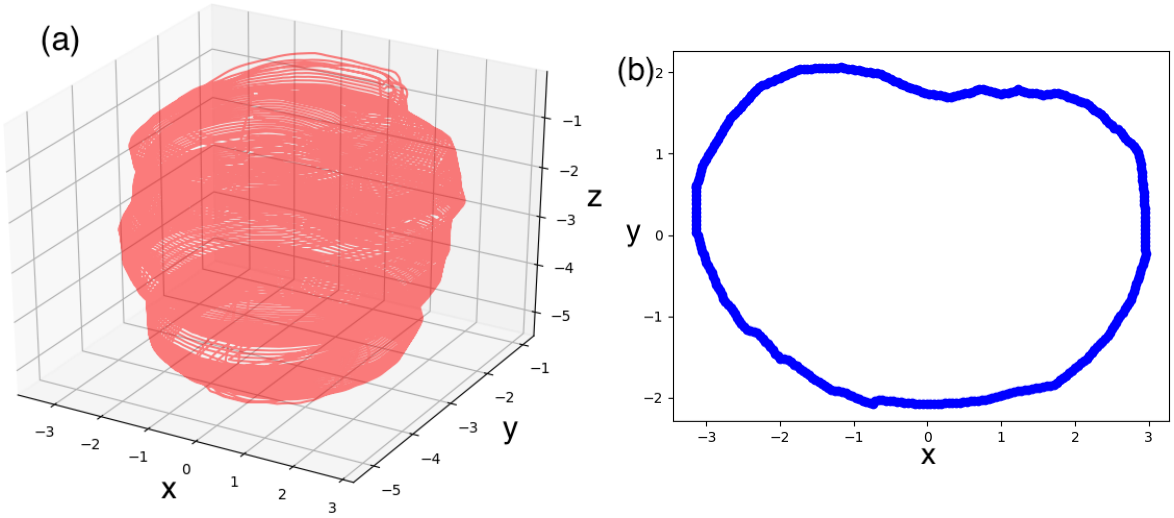

Figure 2.2 – (a) Illustration of the contour of the prostate in 3D (in red curves) extracted from the DICOM file of an HDR-BT treatment for prostate. (b) The maximum surface of the prostate superposed on a 2D plane.

the convex hull of all the given dwell positions was evaluated, which is the smallest convex set that contains all the points, as shown by the red line in Fig. 2.3(b). The area of that convex hull yields the surface area enclosing all the inserted catheters. Finally, the ratio of that area enclosing all the catheters and the maximum surface of the prostate was considered one GP.

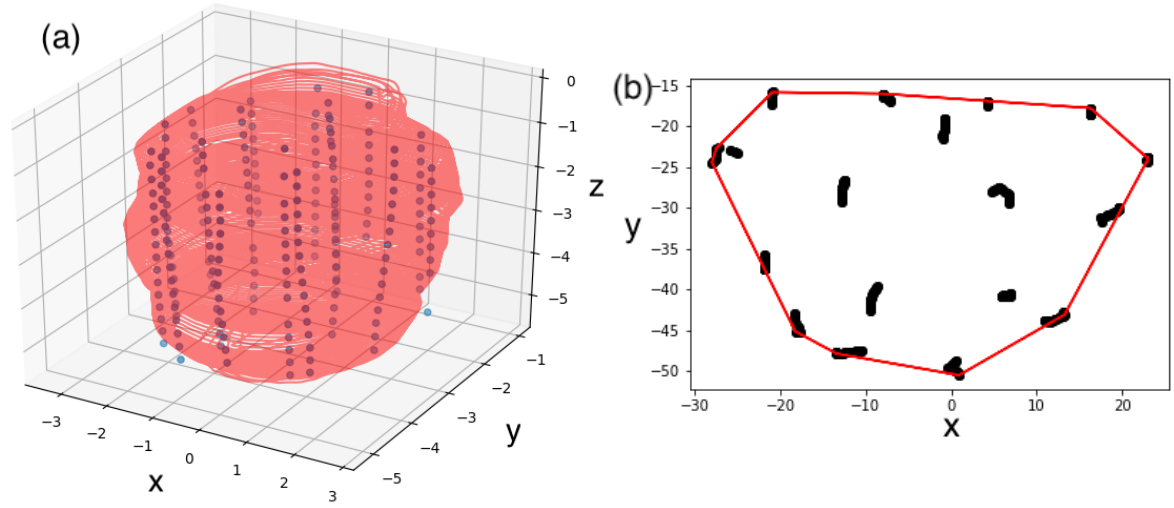

Figure 2.3 – (a) Graphical representation of the dwell positions of all the catheters inserted within the prostate shown as circles, and the 3D contour of the prostate shown in red curves obtained from the DICOM files. (b) The dwell positions superposed on a 2D plane (xy-plane) shown in black circles, and the convex hull of those points represented as a red line.

2.3.5 Average Distance between All the Implanted Catheters

The positioning (i.e. placement) of the implanted catheters, hence their distribution, in the volume of the prostate can affect the dosimetry in TRUS-guided real-time prostate HDR-BT (164, 165). Therefore, the average distance between all the implanted catheters is put forward as a new GP in this study. As discussed in 2.3.4, the 3D coordinates of the dwell positions of all the implanted catheters were extracted for every case. Fig 2.4(a) shows an example of a clinical case for the TRUS-guided HDR-BT treatment for prostate. The central point of each inserted catheter was obtained by computing the mean along the specified axis (the x, y, and z) for all the dwell positions of each catheter. In Fig. 2.4(b), the superpositions of those central points of all the inserted catheters on a 2D plane are exhibited for the same clinical case as in Fig. 2.4(a). Subsequently, the distances between the central point of each catheter and the central point of the rest of the catheters are evaluated. Moreover, the double counting of distances was not permitted in our evaluations. Consequently, the average of all those distances and their associated variance are computed. Note that in some clinical cases, catheters tend to be much more diverging as going near the base of the prostate. Then, using those evaluated central points to calculate the average distance between all the implanted catheters might be a limitation.

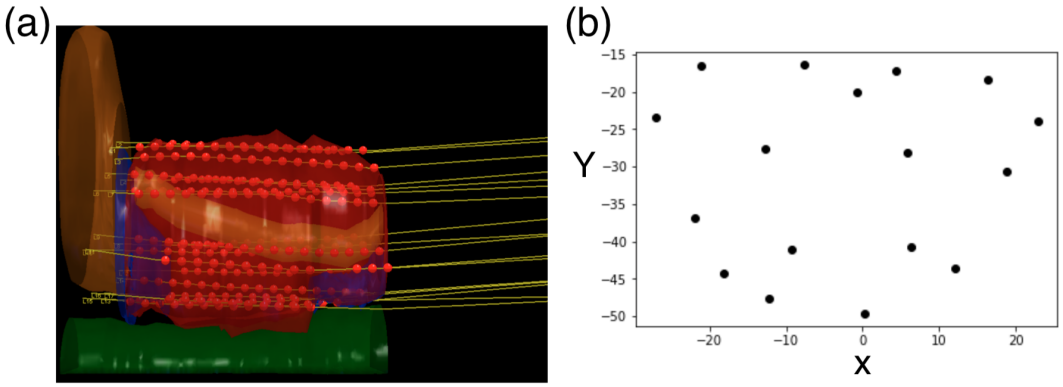

Figure 2.4 – (a) A 3D view of a clinical case taken from the OcP TPS showing the active points (red points) of all the inserted catheters (yellow lines) within the prostate gland (red volume). The bladder is shown as the brown volume, the rectum as the green volume, and the urethra in yellow volume. (b) The superpositions of the central active point of each catheter in a 2D plane (xy-plane).

2.3.6 Minimum Distance between the Dwell Positions of the Lowest Implanted Catheters and their Closest Points on the Rectum

The distance between the active points (i.e., the dwell positions) associated with the implanted catheters and the rectum has an impact not only on the prostate coverage but also on the rectum dose. Due to the proximity of the rectum to the prostate, the rectum is prone to be the dose-limiting structure in the prostate HDR-BT treatments. Overdosing of the rectum can lead to the occurrence of early and late toxicities (166, 167). Therefore, the average of the minimum distances between the dwell positions

of the catheters placed in the lowest portion of the prostate and their closest points on the rectum was used as another GP in the models developed in this research. A Python code was developed that uses the dwell positions and rectum points to determine the minimum distance of all the dwell positions on each catheter and all the points on the rectum. As a result, the catheters situated on the lowest portion of the prostate, hence in the closest proximity to the rectum as compared with the other catheters, were found. Consequently, the average of the minimum distances between the lowest catheters and rectum was evaluated.

Fig. 2.5(a) and (b) illustrate two different clinical cases in which the positioning of the rectum with respect to the prostate, and hence the distance between the rectum and the lowest implanted catheters are different. In the first case, Fig. 2.5(a), given the position of the rectum with respect to the prostate, the distance between the rectum and the lowest inserted catheters varies along the length of the rectum. However, in the second case, Fig. 2.5(b), which occurs more frequently in clinical plans, that distance is nearly identical all along the length of the rectum. Having very small distances between the rectum and the lowest inserted catheters all along the length of the rectum can greatly increase the rectum dose. To study the importance of considering those different cases in our frontier models, two GPs were used. In the first GP, the mean of the minimum distances between the dwell positions of the lowest implanted catheters and the points from the beginning of the rectum to its midplane was evaluated. In the second GP, the mean of minimum distances from the dwell positions of the lowest catheters and the points of the full length of the rectum was calculated.

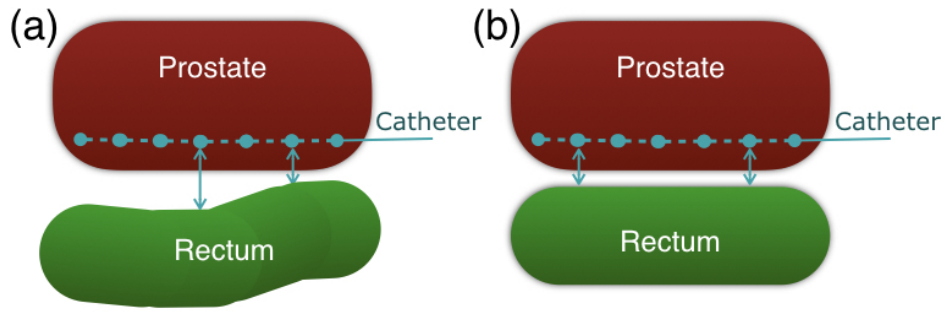

Figure 2.5 – Graphical representation of the two different clinical cases in which the positioning of the rectum with respect to the prostate, and hence the distance between the rectum and the lowest implanted catheters changes along the length of the rectum in (a), but is almost identical all along the length of the rectum in (b). The prostate is pictured in the red, rectum in green, and the dwell positions of the lowest implanted catheters in blue circles.

Two of the possible pitfalls of calculating the minimum distance between the dwell positions of the lowest implanted catheters and their closest points on the rectum are worth mentioning here: 1) considering only the surface area of the rectum obtained based on its convex hull area; 2) taking into account solely the implanted catheters with lower vertical axis (Y) values rather than the other catheters. The first pitfall can appear because the vertical line between a given dwell position of the lowest inserted catheters and a point on the rectum surface does not necessarily yield the required minimum

distance. Furthermore, the coordinates of the convex hull area of the rectum do not always correspond with the coordinates of the points on the surface of the rectum contour. For example, as shown in Fig. 2.6(a) and (b), the agreement between the coordinates of the rectum contour and the ones for the calculated convex hull are examined for two different TRUS-guided HDR-BT treatments for the prostate. As opposed to the case in Fig. 2.6(a), the coordinates of the convex hull of the rectum are not in accordance with the coordinates of the rectum surface exhibited in Fig. 2.6(b). To avoid that pitfall in our research project, all the points on the surface as well as in the volume of the rectum were used to evaluate the minimum distances between the rectum and the lowest implanted catheters. To discuss

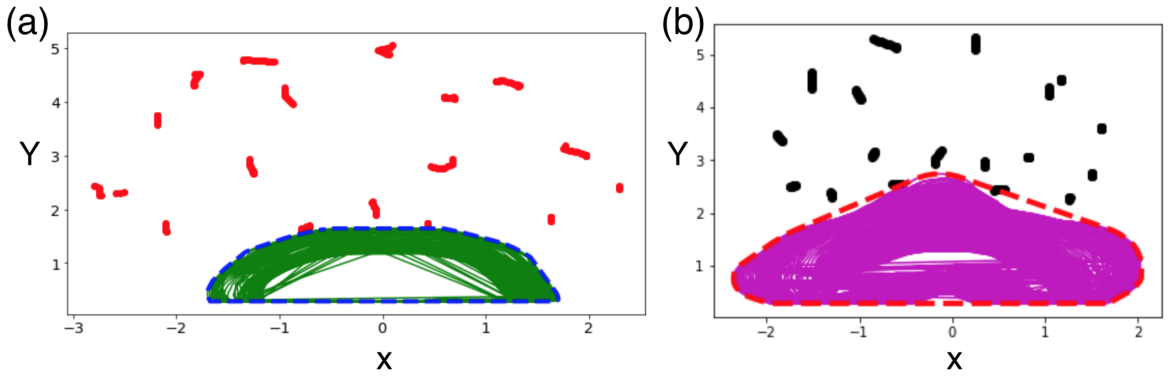

Figure 2.6 – Comparison between the rectum contour and its convex hull areas in two different TRUS-guided HDR-BT treatments for prostate cancer. Contrarily to the case in (a), the coordinates of the convex hull area for the rectum (dashed line) in (b) do not perfectly match with its contour (solid lines). The dwell positions of the inserted catheters are shown as dots.

the second possible pitfall mentioned above, one can refer to the example shown in Fig 2.7(a) and (b). Note that some of the catheters with smaller y values in their dwell position coordinates show much larger distances to the rectum contour as compared with the other catheters.

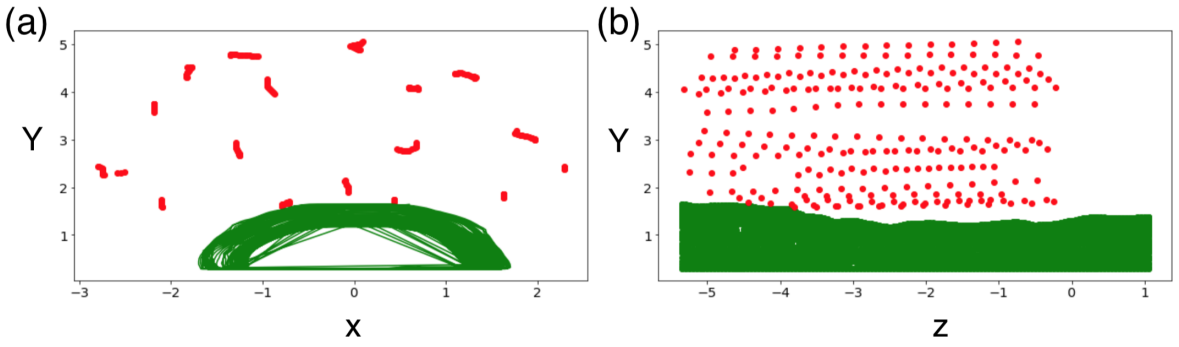

Figure 2.7 – Illustration of the positioning of the implanted catheters and their distances with respect to the rectum for a TRUS-based HDR-BT treatment for prostate cancer. The contour of the rectum (green lines), and the dwell positions of all the inserted catheters (red dots) shown in the x-y plane (a), and in the yz-plane (b).

2.4 Stochastic Frontier Optimization Process

Calculation of the global minimum of multidimensional functions is demanded in numerous problems in physics, medical physics, medicine, statistics, economics, biology, and many other fields (136, 168, 169, 170, 171, 172). In general, optimization methods are categorized as deterministic or stochastic. Standard deterministic approaches can provide satisfactory results for simple non-convex functions that do not include many dimensions. Deterministic methods are known to be fast; however, they are prone to trap the system to a local minimum instead of finding the global minimum. On the other hand, the stochastic methods offer solutions for global optimization problem including multi-dimensions. As compared to the deterministic methods, using stochastic methods allow finding a good approximation of the global minimum through a relatively small amount of computations, with significantly less risk of getting the system stuck within a local minimum (153). Examples of the stochastic methods are evolution algorithms (173, 174), genetic algorithms (175, 176), and SA (177, 136, 178, 179). The SA optimization method is inspired by annealing in metallurgy. By heating materials and then cooling them in a controlled way to influence both the temperature and the thermodynamic free energy, larger sized crystals with the least defects can be obtained. To simulate the thermal noise in the SA optimization method, an artificial temperature is introduced and then gradually reduced. The SA has a statistical nature, and it avoids falling into a local minimum. Therefore, the SA optimization method provides finding the global minimum of any given multi-body problem with a large number of minima (180).

The problems in this research project include optimization of the PSF models for the target, and the CSF model for bladder, rectum, and urethra. To find the optimal PSF model for the target and the optimal CSF model for each of the bladder, rectum, and urethra, a large number of SF models including all the possible combinations of the dominant GPs associated with each of these SF models needs to be optimized. Therefore, finding the global minimum of a multidimensional function is the challenge associated with these optimization processes. To perform these complex, non-linear optimization problems with a large number of optima, MLL method implemented in R (181) and its GenSA algorithm (153, 182, 183) are used. Please note that because the global minimum of a given SF model is obtained using the GenSA algorithm, a minus one (-1) needs to be multiplied to the LL function in Eq.1.17 in order to obtain the maximum of the LL (i.e., MLL). R is a programming language for statistical calculation (181). The R programming was done in RStudio, which is an open-source, integrated development environment for R (184). Additionally, generalized simulated annealing is a calculation method based on stochastic dynamics. The objective of these optimization processes is to find the MLL for each of the different target PSF and the bladder, rectum, and urethra CSF models. *dnorm* and *pnorm* are used to apply the LL function (185). *dnorm* function provides the value of the probability density function (PDF) for a normal distribution. The PDF for the normal

distribution is given by

$$p(x \mid \mu, \sigma) = \frac{1}{\sigma\sqrt{2\pi}} e^{\frac{(x-\mu)^2}{2\sigma^2}}, \tag{2.8}$$

where μ is the mean, and σ is the standard deviation. In case of $\mu = 0$ and $\sigma = 1$, Eq.2.8 turns to $p(x \mid 0,1) = 1/\sqrt{2\pi}\, exp(x^2/2)$. *pnorm* is the cumulative density functions (CDF) of the normal distribution. *pnorm* function is the integral from $-\infty$ to q of the probability density function of the normal distribution. The integral from q to ∞ can be tackled by simply choosing the argument *lower.tail* of the *pnorm* function as *FALSE*. In that case, similar results as given by $1 - pnorm(q, lower.tail = FALSE)$ can be produced by the *pnorm(q)* (185). Consequently, the LL of a production function given in Eq.1.17 in R language is written as

$$\mathscr{L} = sum\left(log\left(\frac{2}{\sigma}\right) * dnorm(\frac{\varepsilon}{\sigma}, 0, 1) * pnorm(-\frac{\varepsilon\lambda}{\sigma}, 0, 1)\right), \tag{2.9}$$

where *sum* is the summation over n plans, $\sigma = \sqrt{\sigma_u^2 + \sigma_v^2}$, and $\lambda = \sigma_u/\sigma_v$. Also, $\varepsilon = \log(y) - f(x_i, \beta)$, is the difference between the dose measured by the OcP TPS (y) and the dose obtained by stochastic frontier analysis in Eq.1.13. Furthermore, the term $1 - pnorm(-\varepsilon\lambda/\sigma, 0, 1)$ in Eq.2.9 was replaced by its equivalent: $pnorm(-\varepsilon\lambda/\sigma, 0, 1)$. Moreover, as stated above, GenSA results in the global minimum. Hence, a minus one (-1) must be introduced to the summation in Eq.2.9 to maximize the LL function. As a result, the MLL value is obtained for the target PSF model. Additionally, to define a cost function in R, the last term in Eq.2.9 must be replaced with $pnorm(\varepsilon\lambda/\sigma, 0, 1)$. Therefore, the MLL value is determined for each of the bladder, rectum, and urethra CSF models.

In the SF optimization process using GenSA algorithm, the values of the model coefficients a_0, a_1, and the weight over the associated GPs, β_i in Eq.1.13 are obtained by maximizing the LL associated with a given SF model under study. These SF models are developed based on the Eq.1.13. Accordingly, the difference between the dose predicted by each of these optimized SFs and the dose provided by the IPSA, ε, is assessed. The probability of occurrence of this difference between each of the SF optimized values and its relevant observation value is determined using Eq.1.17, or equivalently Eq.2.9 in R. Following the same procedure for every plan, the logarithms of these probabilities are summed. To minimize this sum, hence to maximize the LL of the next iteration, GenSA alters the a_0, a_1, β_i, σ_u, and σ_v values. A minus one (-1) is introduced to the LL function in Eq.1.17 to obtain the MLL. Note that several arguments can be used in GenSA to adjust, for example, the initial values for the parameters to be optimized, as well as the lower and upper bounds for these parameters. Other arguments can be employed, such as the maximum number of iterations, the initial value for the temperature, the maximum running time, the maximum number of call of the objective function, and the number of steps after which the program will stop when there is no any improvement (153). We adjusted the default values for the initial values of the parameters under optimization such that they can be generated automatically. Moreover, we applied constraints such as: $\sigma_u \geqslant 0$ and $\sigma_v \geqslant 0$ on Eq.1.13 and Eq.2.9. Also, we set the lower and upper bounds for the rest of the parameters, for example, a_0, a_1, and β_i to accept all the real numbers ($\mathbb{R}$). As a consequence, enough freedom is given to the GenSA algorithm to explore the optimal parameters.

2.5 Application of Spearman Correlation Method in Finding the Dominant Geometric Parameters

The number of possible SFs for each of the target PSF and the bladder, rectum, and urethra CSF models can be computed by summing up all the different combinations of GPs. The number of combinations when choosing r elements from a set of n elements is given by ${}_rC_n = n!/r!(n-r)!$. If the number of GPs in the set (n) is 18 and the number of GPs in each combination (r) is taken as, for example, 12, then the number of combination (i.e., n things taken r at a time) is 18,564. Since for the total of $n = 18$ GPs, r can be taken between $r = 1, \cdots, 18$, there would be 18 different combination to be summed. The result of the sums of all the possible combinations of all the 18 GPs in our study $(1 + 18 + 153 + \cdots + 18)$ gives a total of 262,143 potential SFs for each of the target PSF or bladder, rectum, and urethra CSF models. Additionally, the MLL in Eq.1.17 or its equivalent Eq.2.9 would need to be evaluated for all these SFs. That is a very large number which would require a prohibitively long computing time, and thus would not be practical. To tackle that difficulty, the correlation between GP and DP was calculated to simplify the problem. To do so, the SCC method, discussed in chapter 1.3, is brought into play to asses the strength and direction of a monotonic relationship between two variables. The two variables in our study are a GP and a DP of interest. Also, the SCC between every two GPs can be evaluated. By evaluating the SCC between a DP and a GP, the dominant GPs associated with a given SF model are obtained. As a result of only taking into account these dominant GPs, the total possible combinations to be optimized for the target PSF and the bladder, rectum, and urethra CSF models would be significantly reduced. For example, if 12 dominant GPs is considered (rather than 18 GPs) for the target PSF model, only 4095 (as compared to 262,143) combinations need to be studied. That leads to a reduction in the cost of the corresponding calculations.

It should be noted that R built-in functions in Rstudio are used to evaluate the SCC matrix including all the possible pair parameters between all the GPs and the DP of interest. These R built-in functions in Rstudio are provided in A.3. For more details related to the R built-in functions in Rstudio, the interested reader is referred to (186).

2.6 Brute-Force Search

The dominant GPs for each of the target PSF and the bladder, rectum, and urethra CSF models are found using the SCC method. Then, the target PSF, as well as the bladder, rectum, and urethra CSFs models including all the possible combinations of their corresponding dominant GPs are optimized. The optimizations of these SF models are carried out using the MLL method implemented in R, and its GenSA algorithm. The SF with the largest value of the MLL as compared to the other possible target PSFs is determined for the target PSF. Afterward, to specify the optimal SF model for the target PSF, the LRT, given in Eq.1.18, and its corresponding p-value are used. By employing LRT,

the statistical significance of adding new GPs to a given SF model is studied. In other words, LRT and its corresponding p-value are performed between the obtained target PSF model with the highest MLL and another PSF model with nearly the same MLL value yet a lower number of GPs. Then, one examines whether choosing the target PSF model with a higher number of GPs rather than selecting the PSF model with a lower number of GPs is statistically significant. If choosing the PSF model with a larger number of GPS is statistically significant, this model is selected as the optimal target PSF model. Otherwise, the target PSF model with the lower number of GPs is selected. Therefore, the LRT is carried out between this model and another PSF model with even less number of the dominant GPs. This process is continued, and different LRTs are studied until the point where it is not statistically significant to select a model with a lower number of GPs anymore. At that point, the model with a higher number of GPs is chosen as the optimal PSF model for the target. Please bear in mind that a similar process is followed, individually, for each of the bladder, rectum, and urethra CSF models, and their corresponding optimal CSF models were determined.

Independent optimization of a significant number of target PSF and bladder, rectum, and urethra CSF models including different possible combinations of their dominant GPs, as well as individual evaluation of their corresponding MLL values, are not efficient. Therefore, a systematic approach, namely brute-force search, was used to tackle these difficult problems (187). Brute-force search, also called an exhaustive search, is a search over all the plausible solutions for a problem, without eliminating any possibilities. It is a general problem-solving approach in which all the possible solutions are systematically enumerated. Finally, the fulfillment of the problem's statement is verified through the analysis of each of the possibilities. In general, after determining all the constraint defined by the problem under study in a brute-force search, a method of generating all possible solutions that satisfy the constraints of the problem is developed. Indeed, one needs to ensure there are no unacceptable solutions among all the generated solutions and to verify the accuracy of the results.

For the target PSF model in this research project, the DP of interest is the dose V100. Then, a list including all the dominant GPs for the target PSF model is defined. As explained in 2.5, these dominant GPs are determined using the SCC method. Furthermore, a loop iterating over various combinations of the parameters in the list of the dominant GPs is established. Various forms of PSFs are defined in the loop. Depending on the length of the GPs in each of these PSFs, the form of the frontier in Eq.1.13 changes. For instance, for a list of 12 dominant GPs, frontiers including 12 GPs, 11 GPs, $\cdots$, and 1 GP are developed. As discussed in 2.5, the number of combinations can be calculated for each of these PSF models. For example, 12 possible combinations for the PSF with 1 GP, 66 combinations for the PSF with 2 GPs, $\cdots$, and 1 combination for the PSF with 12 GPs are obtained. Accordingly, all the possible PSF models including various combinations of these dominant GPs are systematically generated in R. The SF optimization process is conducted for each of these target PSF models using the MLL approach and its GenSA algorithm as discussed in 2.4. As a result, the MLL values and the optimized parameters are evaluated for all the generated target PSF models. Note that the same procedure is carried out individually for the bladder, rectum, and urethra CSF models

considering their relevant dominant GPs.

Consequently, using the brute-force test, the MLL value associated with all the possible combinations of dominant GPs for each of the target PSF, as well as the bladder, rectum, and urethra CSFs are systematically calculated. Automation of all the optimization processes and the MLL evaluations associated with a great number of PSF and CSF models are accomplished using parallel calculations in R. Moreover, the obtained results of these calculations are collected in parallel. The parallel computations in R are fulfilled using the corresponding Rstudio packages including R built-in functions for parallel execution of the codes on systems with several cores or processors or many computers (188). To increase the speed of these parallel calculations, they are executed on a machine with multiple cores. The interested reader is referred to A.3 to obtain details on R built-in functions in Rstudio to perform a brute-force search using loops and parallel computations.

2.7 Application of the SF Models on the CT-based HDR-BT Plans for Prostate Cancer

Once the target PSF and the bladder, rectum, and urethra CSF models are developed based on the TRUS-based HDR-BT treatment plans, we verify if these SF models are universal. In other words, we study whether these SF models succeed to perform well outside of the respective TRUS-based category of the HDR-BT for prostate cancer. The generalization of the developed SF models is performed using another category of the HDR-BT treatments, such as CT-based.

Therefore, another cohort consisting of one hundred CT-based HDR-BT plans for prostate cancer is used in which CT was used rather than TRUS. Furthermore, all the patients in this cohort were treated with a single fraction 15Gy. Moreover, the treatments of all these patients were optimized using the IPSA algorithm in the Oncentra Brachy TPS. Using this cohort, a CT-based PSF model is developed for the target. Subsequently, the CT-based PSF model for the target is compared to its corresponding TRUS-based model. Additionally, a CT-based CSF model is developed for each of the bladder, rectum, and urethra. Finally, each of the bladder, rectum, and urethra CT-based models was compared to its corresponding TRUS-based CSF model.

Please note that our objective in comparing the developed rectum, as well as the target and urethra, models with their corresponding models using the CT-based plans including the modified GPs is to verify if these SF models can be applied to another category of the HDR-BT treatment for prostate cancer. Therefore, in the case of the CT-based SF models, the SCC approach is not used to specify the dominant GPs for the CT-based models. For the sake of the comparison between the TRUS-based and CT-based categories of the HDR-BT treatments, the dominant GPs similar to their corresponding TRUS-based SF models are used to design four new SF models. These SF models include a PSF model for the target and a CSF model for each of the bladder, rectum, and urethra. Afterward, each of these

SF models is individually applied to one hundred CT-based HDR-BT plans. Then, the optimization approach, similar to the TRUS-based models, is followed, however, this time using the CT-based plans. The corresponding MLL values are obtained. Further, several LRTs are carried out, and the corresponding p-values between every selected null and alternative models are evaluated. Thus, the optimal CT-based target PSF model is obtained. Finally, the dominant GPs in the CT-based target PSF model are compared with the GPs in the corresponding TRUS-based target PSF model. Additionally, the same approach is followed to figure out the optimal CT-based CSF models for the bladder, rectum, and urethra CSF models. The dominant GPs in the CT-based CSF model for the bladder, rectum, and urethra are compared with the dominant GPs in their corresponding TRUS-based CSF model.

It should be noted that differences are observed between the range of the bladder and rectum volumes in the two categories of the HDR-BT treatments under study. These differences in the bladder and rectum volumes between the TRUS-based and CT-based plans are due to the variations in the contouring of the structures in each of these two categories of the HDR-BT treatment for prostate cancer. On average, the contoured volumes of the bladder in CT-based HDR-BT plans under investigation are obtained five to six times bigger than the corresponding contoured volumes in TRUS-based plans. In the case of the rectum, the CT-based contours are, on average, three to four times bigger than the corresponding TRUS-based contours. As a result of the limited image field-of-view in US-based HDR-BT, only fractions of rectum and bladder can be contoured. As an example, Figs. 2.8(a) and (b) show the prostate and OARs contours, associated with, respectively, CT-based and TRUS-based. The prostate contour is represented in red, the bladder in the blue, the rectum in brown, and the urethra in yellow. As can be deducted form Fig. 2.8(a), in the case of using CT-based HDR-BT for prostate, the OAR volumes are fully contoured. However, in TRUS-based HDR-BT for prostate, as exhibited in Fig. 2.8(b), only parts of the rectum and bladder volumes are contoured. Additionally, as mentioned in 1.1.1.2, the limitations in the capacity of the crystals used in the current US equipment lead to restrictions in the production and detection of the sound waves. More importantly, since the probe tube of TRUS equipment is placed inside the rectum, solely the interior part of the rectum can be contoured. Due to these limitations exist in contouring the entire volume of the structures, such as the rectum and bladder, for Dose-Volume Histogram (DVH) calculation, the BT OAR dose distribution information is restricted. Bear in mind that TRUS images provide sufficient information needed to verify whether the volumes of bladder and rectum receive 75% of the prescription dose. Therefore, the agreement with the ABS recommendation for bladder and rectum: V75B < 1 cm^3 and V75R < 1 cm^3 respectively, is controlled (68).

As will discussed in 3.3, the modified GPs are introduced into the CT-based HDR-BT plans for the sake of the comparison between the developed TRUS-based SF models and their corresponding CT-based SF models. In the CT-based plans including the modified GPs, the extra volumes associated with the variations in contouring the structures in the TRUS-based and CT-based HDR-BT treatments for prostate cancer. In 3.3, the TRUS-based rectum CSF model is compared with the rectum CSF model developed using the CT-based HDR-BT treatment plans in which the modified GPs were applied.

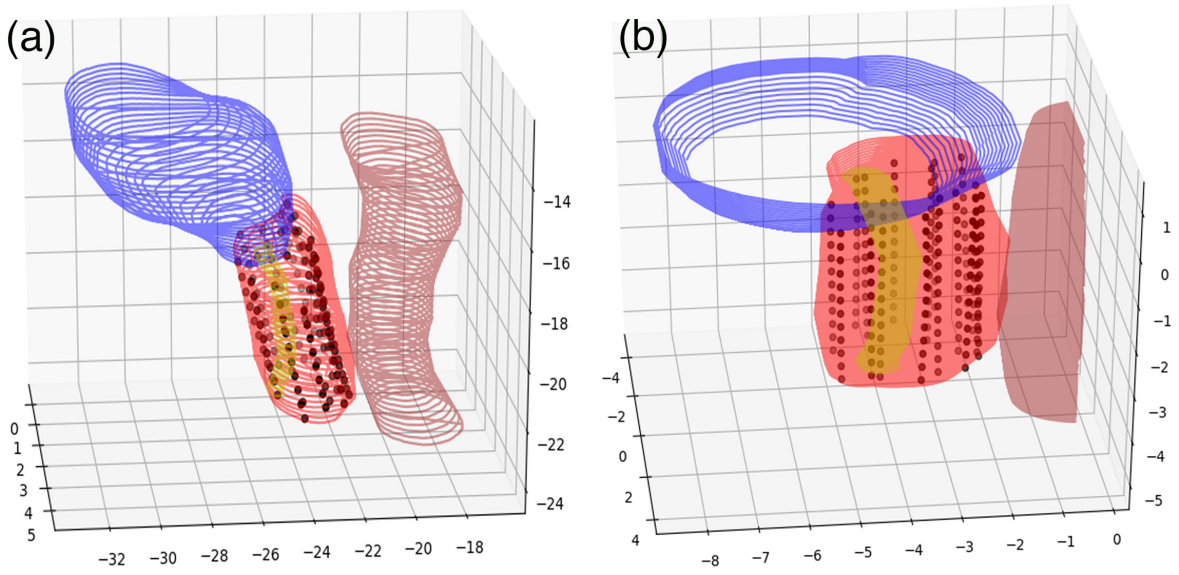

Figure 2.8 – Comparison between the contours obtained by using CT-based (a) and TRUS-based (b) images in HDR-BT for the prostate. The contours of the prostate shown in red, bladder in the blue, rectum in brown, and urethra in yellow. Dark dots represent the dwell positions within the prostate.

The rectum CSF model will be discussed as the first example to verify whether the variations in the contouring of the structures in the CT-based as compared with the TRUS-based HDR-BT treatments for prostate cancer can lead to differences in the dominant GPs of the corresponding SF models. Therefore, the extra contoured volume of the rectum, such as the part of the rectum that extends further than the length of the prostate, is discarded from the CT-based HDR-BT treatment plans. Additionally, the GPs related to the HDs between the CTV and rectum, and the minimum distance between the active points of the catheters placed in the lowest portion of the prostate and their closest points on the rectum will vary accordingly. Then, the CT-based rectum CSF models are designed including different combinations of these modified GPs. Consequently, the rectum CSF models in the TRUS-based are compared with the corresponding models in the CT-based plans including the modified GPs. It should be noted that the same process is followed for the target PSF and urethra CSF models, which will be discussed in 3.3.

Chapter 3

Results and Discussion

3.1 Production Stochastic Frontier

In the following section, the results of the SCCs for the target PSF are discussed. Then, once the GPs having negligible correlation with the DP of interest have been discarded, the brute-force search is implemented. Finally, the CSF with the highest MLL value but the minimum number of GPs is established for bladder, rectum, and urethra.

3.1.1 Results of the Spearman Correlation Coefficient and Brute-Force Search for the Target Parameters

A pairwise SCC matrix provides measures of the SCC between every combination of the parameters of interest. Employing such a pairwise SCC matrix is a great way to investigate new data. Fig. 3.1 shows the V100 DP and all the 18 GPs of the target. The horizontal and vertical axes of the table in Fig. 3.1 represent all the 18 GPs and the DP V100 for the target covering. Furthermore, the spectrum on the right of the figure exhibits the strength and the direction of the correlation between the pair parameters. $+1$ shown in dark blue indicates a strong positive correlation, and -1 displayed in dark red signifies a strong negative correlation. The parameters in Fig. 3.1 were ordered to detect more easily the pattern of high and low correlations, and also the positive or negative correlations between many parameters. The intensity of the color filled in the entire block denotes the strength of a correlation associated with the relationship between every pair of parameters. Additionally, the magnitude and direction of an SCC between two parameters are signified respectively by a value and its $\pm$ sign inside of each block. Every parameter in the diagonal is auto-correlated with itself. The auto-correlations of all parameters are shown using a dark blue color and $+1$ value along the diagonal. Other forms of representing the pairwise SCC matrix are possible. Two examples of these different forms using geometrical shapes are provided in A.1. However, the SCC representation in Fig. 3.1 is easier to follow and is used in this research to choose the dominant GPs.

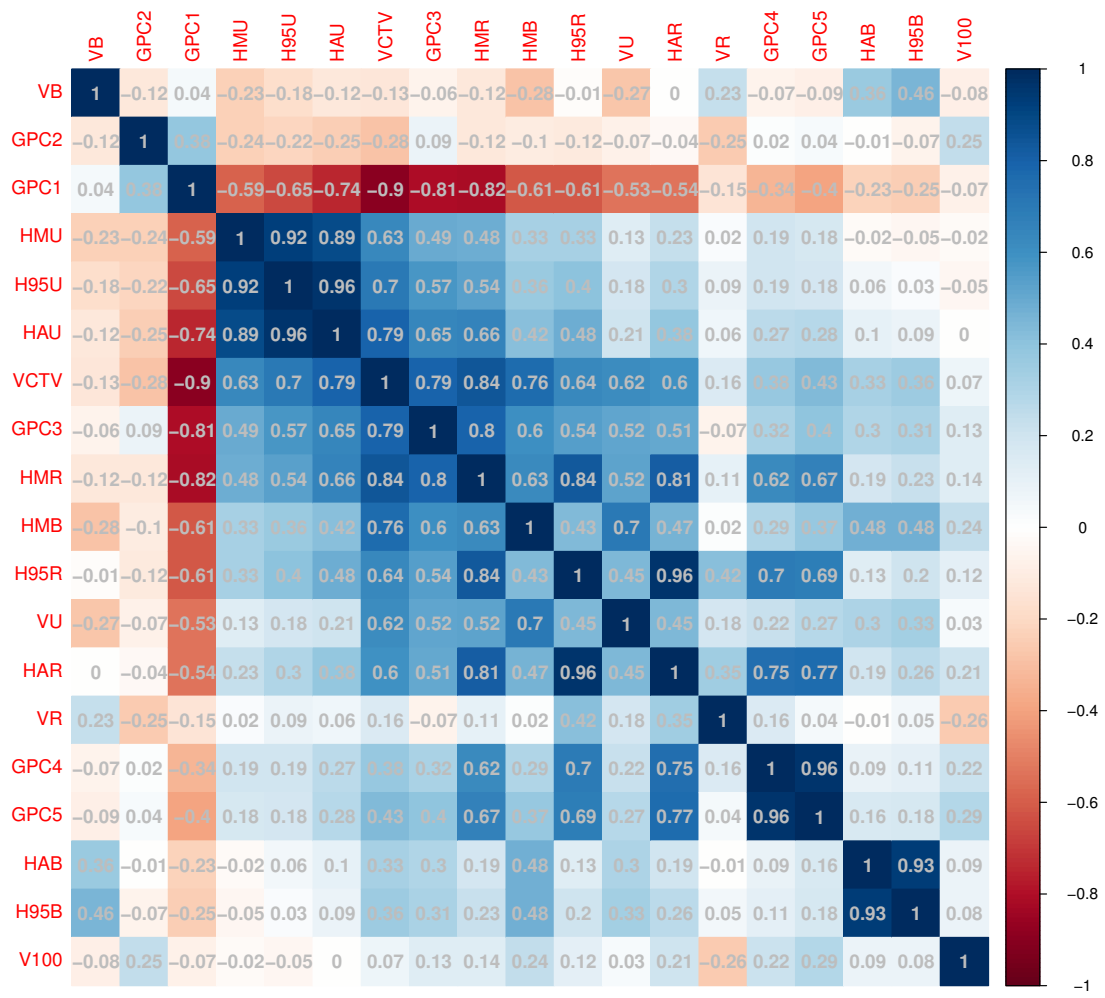

Figure 3.1 – Target SCC matrix representing the strength and direction of the SCCs of all the pair parameters between the 18 GPs and the DP (V100) of the target. The color spectrum along with the corresponding number indicate the direction and strength of each correlation. The darkest blue and red illustrate the strongest positive and negative correlations, respectively.

As discussed in 2.6, after finding the dominant GPs for each SF by means of the SCC method, brute-force search was carried out. This search included a systematic optimization of the possible combinations of dominant GPs, and subsequently calculation of the corresponding MLL value for each model. The dominant GPs with larger values of the SCCs as compared with the other pair parameters of the target covering given in Fig. 3.1 was selected for the brute-force search. Table. 3.1 provides the selected GPs along with their SCCs with respect to dose V100 to the target. The GPs with higher correlation with the selected GPs in Table. 3.1, and smaller correlation with the DP of interest as compared with the corresponding selected GPs, were not selected for the target PSF model. For example, as shown in Fig. 3.1, the volume of CTV (VCTV) has a high correlation (0.84) with the Hausdorff

distance of the max of the volume of the rectum (HMR). Also, the HMR has a higher SCC (0.14) with the V100 DP as compared with the VCTV (0.07). Therefore, VCTV was not taken into account in the target PSF model. The 12 selected GPs were sorted in Table. 3.1 based on their SCC values in descending order regardless of their $\pm$ signs. As discussed in 2.5, by taking the 12 dominant GPs into

Table 3.1 – The GPs with higher values of the SCC, hence more significant correlation with respect to the DP V100 for the target.

	GPC5	**VR**	**GPC2**	**HMB**	**GPC4**	**HAR**	**HMR**	**GPC3**	**H95R**	**HAB**	**H95B**	**VB**
V100	0.2881	-0.2574	0.2474	0.2414	0.2176	0.2087	0.136	0.1348	0.1197	0.0857	0.0834	-0.0806

account, a total of 4,095 possible SFs need to be verified for the target, and the corresponding MLL values need to be computed.

3.1.2 Target Production Stochastic Frontier

As discussed in 1.2.3, the LRT in Eq.1.18 was performed to evaluate the statistical significance of adding different GPs in a PSF model. Table. 3.2 shows the MLL values related to a number of target PSF models including various GPs (n). It should be noted that all the possible combinations were examined, but only the values for n =18, 12, 7, 5, 4, 3, and 2 are presented. The p-value, provided in Eq.1.18, corresponding to the LRT for the two competing SF models under study was computed. The two competing models are the model with the fewer number of GPs (i.e., null model) and the model with more parameters (i.e., alternative model). Moreover, the difference between the number of GPs of the null and alternative models, df, is provided.

The last column in Table. 3.2 shows the rejected model in the LRT between the two considered competing models. The MLL values of all the possible combinations of the GPs for the target PSF models were calculated in the previous section 3.1.1. After, the LRT is performed between every two selected models and the corresponding p-value is studied. For example, the LRT between the two models with 18 and 12 parameters resulted in a p-value larger than the significance level of 0.05. As a result, the alternative model with 18 parameters was rejected, and the model with 12 parameters was chosen. In the same way, we calculated the LRT and the corresponding p-value of each two competing null and alternative models in Table. 3.2. As another example, the LRT between the null model with two parameters and the alternative model with three parameters resulted in a p-value less significant than 0.05. Thus, the null model was rejected, and the alternate model with three parameters was chosen. These dominant GPs for the target PSF model are the volume of the rectum (VR), the Hausdorff distance (HD) between CTV and the average volume of the rectum (HAR), and the ratio of the area enclosing all the implanted catheters and the maximum surface of the prostate (GPC2).

Additionally, one can examine the LRT between the alternative model with 18 parameters and the null model with three parameters. Then, the corresponding p-value showed a value of 1, which is larger

Table 3.2 – MLL values for some optimized target PSF models including different number of GPs using the TRUS-based HDR-BT plans for prostate cancer. P-value related to the LRT between the selected null and alternative models. The null model has a lower number of parameters with respect to the alternative model on its higher row with a larger number of parameters. The degree of freedom (df) is the difference between the number of parameters between the null and alternative models. The rejected model in each LRT is shown.

GPs included in each target PSF model (TRUS-based)	**n**	**MLL**	**p-value**	**Null model**	**Alternative model**	**df**	**Rejected model**
All the GPs	18	-289.7524					
VB, VR, HMB, HAB, H95B, HMR, HAR, H95R, GPC2, GPC3, GPC4, GPC5	12	-290.1153	1	12 par.	18 par.	6	Alternative
VB, VR, HMB, H95B, HMR, HAR, GPC4	7	-289.5159	0.9449	7 par.	12 par.	5	Alternative
VB, VR, HAB, HAR, GPC5	5	-291.9008	1	5 par.	7 par.	2	Alternative
VR, HMB, GPC2, GPC5	4	-290.0231	0.0526	4 par.	5 par.	1	Alternative
VR, HAR, GPC2	3	-291.2876	1	3 par.	4 par.	1	Alternative
VR, HAR	2	-286.9135	0.003	2 par.	3 par.	1	Null

than the selected significance level. Therefore, the alternative model with 18 parameters was rejected, whereas the null model with three parameters was selected.

Furthermore, the LRT between the two models with five and three GPs was carried out, and the corresponding p-value was evaluated. The resulting p-value (0.541) was larger than the chosen significance level. Thus, the alternative model with five GPs was rejected, and the null model with three GPs was chosen. Therefore, the model with three GPs was determined as the main model for the target PSF model. Eq.3.1 gives the target PSF model for the TRUS-based HDR-BT along with the corresponding weights of all its dominant GPs.

$$\begin{aligned}\text{Target PSF model (TRUS-based)} &= -1319.072 \times (\text{VR}) + 2579.514 \times (\text{HAR}) \\ &+ 9981.375 \times (\text{GPC2}).\end{aligned} \tag{3.1}$$

Fig. 3.2 shows the hundred TRUS-based HDR-BT treatment plans for prostate cancer along with the developed target PSF. This frontier is based on the PSF model in Eq.3.1. Note that 94% of these plans were found below the target PSF.

3.2 Cost Stochastic Frontiers

Following the same methods as in the preceding section 3.1, the resulting SCCs, brute-force searches, and the developed optimum CSFs are obtained for the three OARs. The considered OARs are the bladder, rectum, and urethra. The results are provided in the following.

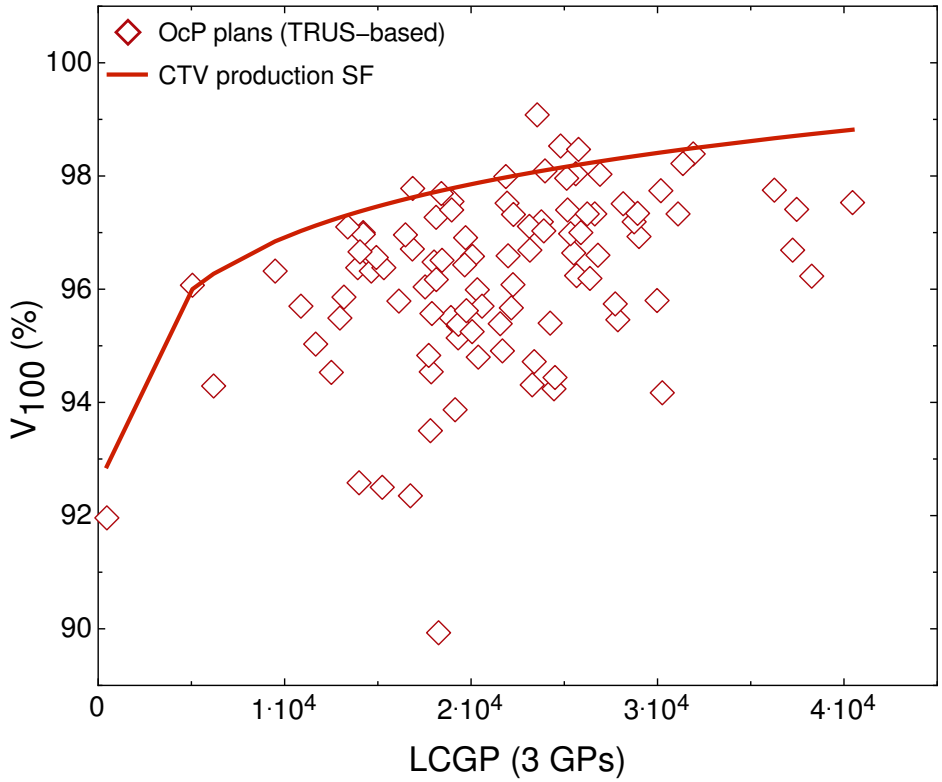

Figure 3.2 – One hundred TRUS-based HDR-BT plans for prostate cancer demonstrated by the empty diamonds. The developed target PSF exhibited by the solid line.

3.2.1 Bladder

3.2.1.1 Results of the Spearman Correlation Coefficient and Brute-Force Search for the Bladder Parameters

Fig. 3.3 shows the results of the SCCs for the dominant GPs determined for the bladder. This figure represents the pattern of strong, weak, positive or negative correlations between all the GPs for the bladder. Other graphical representations of the bladder SCCs are provided in A.1. Fig. 3.3 was selected to decide the parameters included in the bladder CSF model.

As mentioned previously in 2.6, the GPs with larger values of SCCs for paired parameters of the bladder provided in Fig. 3.3 were selected. Then, the brute-force search was carried out to systematically evaluate the MLL value of each of the possible combinations of these GPs for the bladder. Table. 3.3 represents the chosen GPs and their corresponding SCCs with respect to dose V75 to the bladder (V75B). By considering 13 dominant GPs, a total of 8,191 possible PSF models for the bladder need to be optimized and the corresponding MLL values calculated.

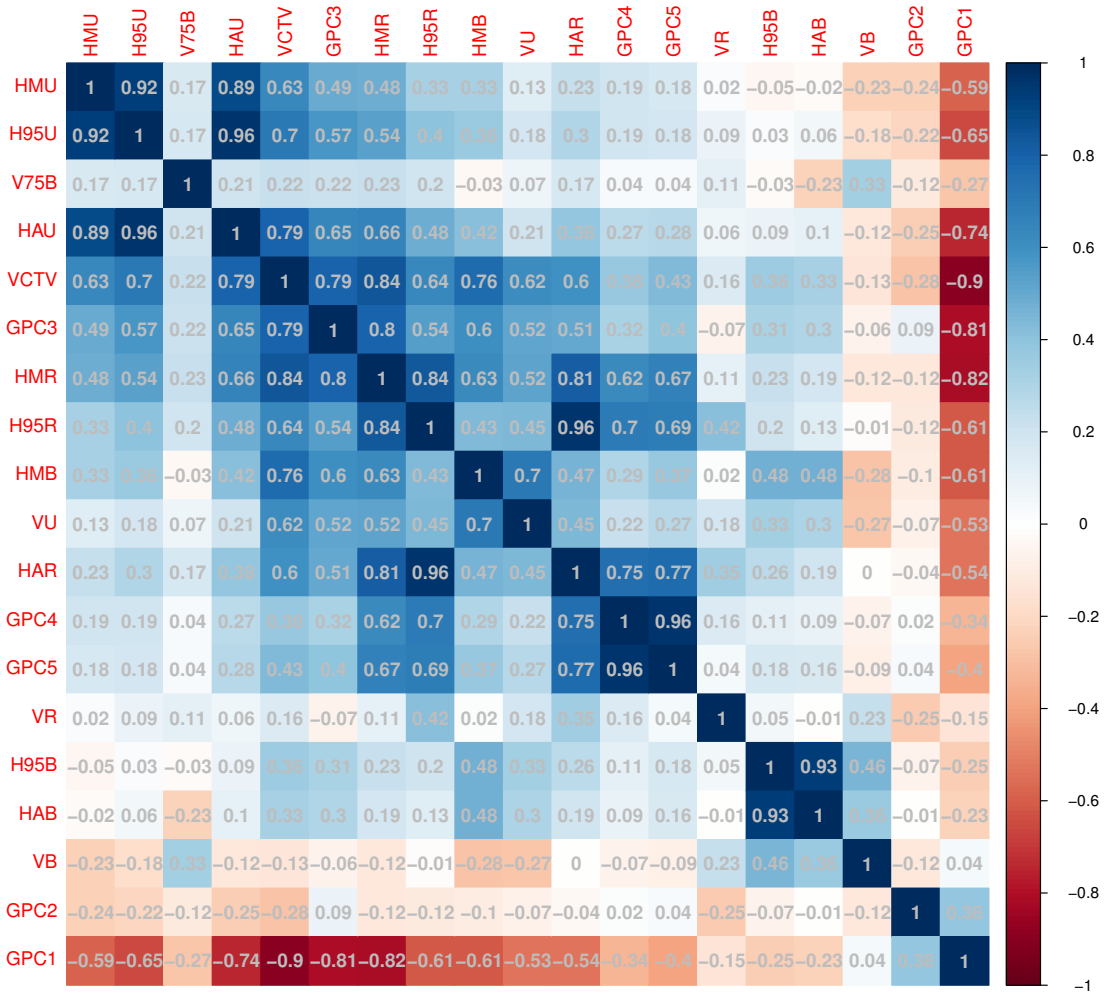

Figure 3.3 – Bladder SCC matrix indicating the strength and direction of the SCCs of all the pair parameters between the 18 GPs and the DP (V75) of the bladder. The color spectrum and the corresponding number represent the direction and strength of each correlation. The darkest blue and red indicate the strongest positive and negative correlations, respectively.

Table 3.3 – The GPs with higher values of the SCCs, hence higher correlation, to dose V75 to the bladder (V75B).

	VB	GPC1	HMR	HAB	VCTV	GPC3	HAU	H95R	HAR	H95U	HMU	GPC2	VR
V75B	0.3308	-0.2714	0.2292	-0.2257	0.2244	0.2158	0.2076	0.1991	0.1732	0.1707	0.1663	-0.117	0.1118

3.2.1.2 Bladder Cost Stochastic Frontier

Referring to our previous discussion in 3.1.2, the MLL values of all the possible combinations of the GPs for the bladder CSF models in 3.2.1.1 were obtained. Note that all combinations were tested, however only the values for 18, 13, 7, 6, and 5 GPs are presented in Table. 3.4. The LRT and the corresponding p-value was evaluated for each of the two selected models; the null model and alternative models.

Table 3.4 – MLL values for some optimized bladder CSF models including different number of GPs using the TRUS-based HDR-BT plans for prostate cancer. P-value related to the LRT between the selected null and alternative models.

GPs included in each bladder CSF model (TRUS-based)	n	MLL	p-value	Null model	Alternative model	df	Rejected model
All the GPs	18	124.0163					
VCTV, VB, VR, HAB, HMR, HAR, H95R, HMU, HAU, H95U, GPC1, GPC2, GPC3	13	125.6517	0.6583	13	18	5	Alternative
VB, VR, HAB, HMR, HAU, H95U, GPC1, GPC3	8	130.0937	0.1137	8	13	5	Alternative
VB, HAB, HMR, HAU, H95U, GPC1, GPC3	7	129.9388	1	7	8	1	Alternative
VB, HAB, HMR, HAU, GPC1, GPC3	6	131.4082	0.0864	6	7	1	Alternative
VB, HAB, HMR, H95R, GPC1	5	137.1237	0.0007	5	6	1	Null

The LRT between the alternative model with 18 parameters and the null model with six parameters was considered. The corresponding p-value was obtained (0.2534) more substantial than the significance level of 0.05. Therefore, the alternative model with 18 GPs was rejected, and the null model with six GPs was chosen. The same way every two competing bladder CSF models were verified. Furthermore, by performing the LRT between the alternative model with six and the null model with five GPs, the corresponding p-value was evaluated (0.0007) smaller than the significance level. As a result, the null model with five GPs was rejected, and the model with six GPs was selected. Although not presented in Table. 3.4, all the possibilities below $n = 5$ were tested. Consequently, the chosen bladder CSF model is composed of six dominant GPs. These dominant GPs are: the volume of the bladder (VB), the HD between the CTV and the average volume of the bladder (HAB), the HD between the CTV and the maximum volume of the rectum (HMR), the HD between the CTV and the average volume of the urethra (HAU), the ratio of the number of implanted catheters and the maximum surface of the prostate (GPC1), and the average distance between all the implanted catheters (GPC3). Eq.3.2 provides the developed bladder CSF model.

$$\begin{aligned}\text{Bladder CSF model (TRUS-based)} &= 1124.7473 \times (\text{VB}) - 6887.3695 \times (\text{HAB}) \\ &+ 3516.2393 \times (\text{HMR}) + 3840.7572 \times (\text{HAU}) + 8962.7214 \times (\text{GPC1}) \\ &- 5634.4686 \times (\text{GPC3}).\end{aligned} \tag{3.2}$$

Fig. 3.4 exhibits the hundred TRUS-based HDR-BT plans for prostate cancer along with the developed bladder CSF. 63% of the plans were found above the bladder CSF.

3.2.2 Rectum

3.2.2.1 Results of the Spearman Correlation Coefficients and Brute-Force Search for the Rectum Parameters

Fig. 3.5 exhibits the SCCs associated with all the pair parameters for the rectum. These parameters were arranged following a pattern of strong and weak, as well as positive or negative correlations.

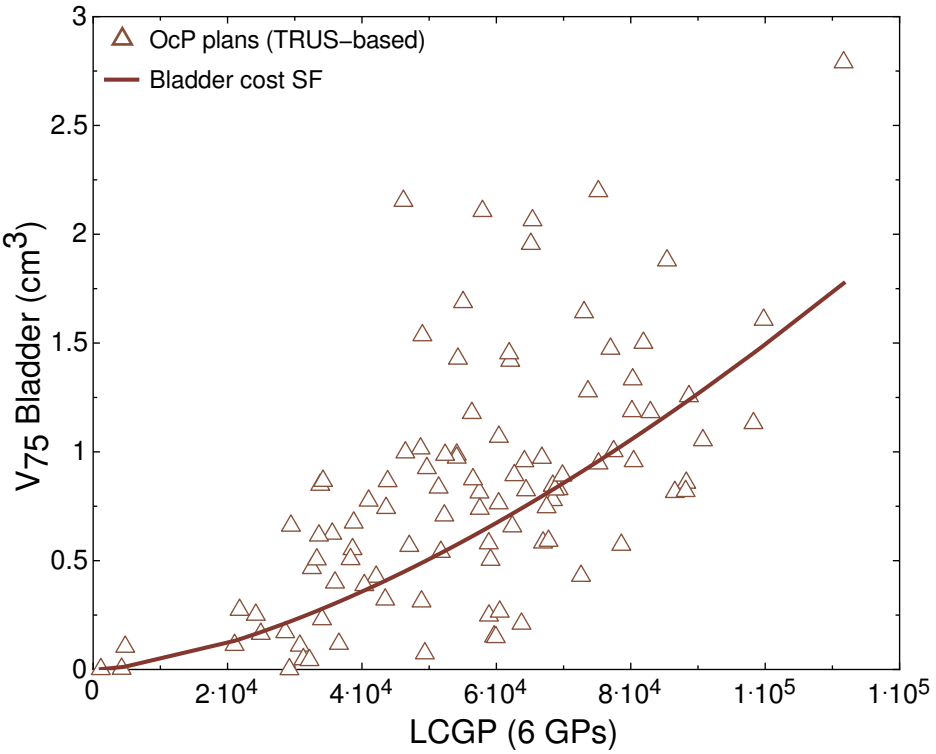

Figure 3.4 – One hundred TRUS-based HDR-BT plans for prostate cancer exhibited by the empty triangles. The corresponding developed bladder CSF shown by the solid line.

Other illustrations of the SCCs for rectum are given in A.1, however Fig. 3.5 was used to decide on the dominant GPs in the rectum CSF model.

As explained in 2.6, the brute-force search were performed using GPs with larger values of the SCCs with respect to V75R, as provided in Table. 3.5.

Table 3.5 – The GPs with higher values of the SCC, hence more significant correlation, dose V75 for the rectum (V75R).

	GPC5	GPC4	HAR	GPC2	H95R	HMR	H95U	VR	VB	GPC1	HAU	HMU	VCTV
V75R	-0.5419	-0.4798	-0.4458	-0.3674	-0.3262	-0.2356	0.181	0.1737	0.161	-0.1375	0.1367	0.1094	0.0746

Since 13 dominant GPs are taken into consideration, the MLL needs to be evaluated for a total of 8,191 possible SF frontiers for the rectum.

3.2.2.2 Rectum Cost Stochastic Frontier

Table. 3.6 provides the MLL values resulting from the optimization of some of the possible combination the rectum CSF models for TRUS-based HDR-BT plans. The LRT between every two selected models was carried out and the corresponding p-value was calculated. Note that all the possible com-

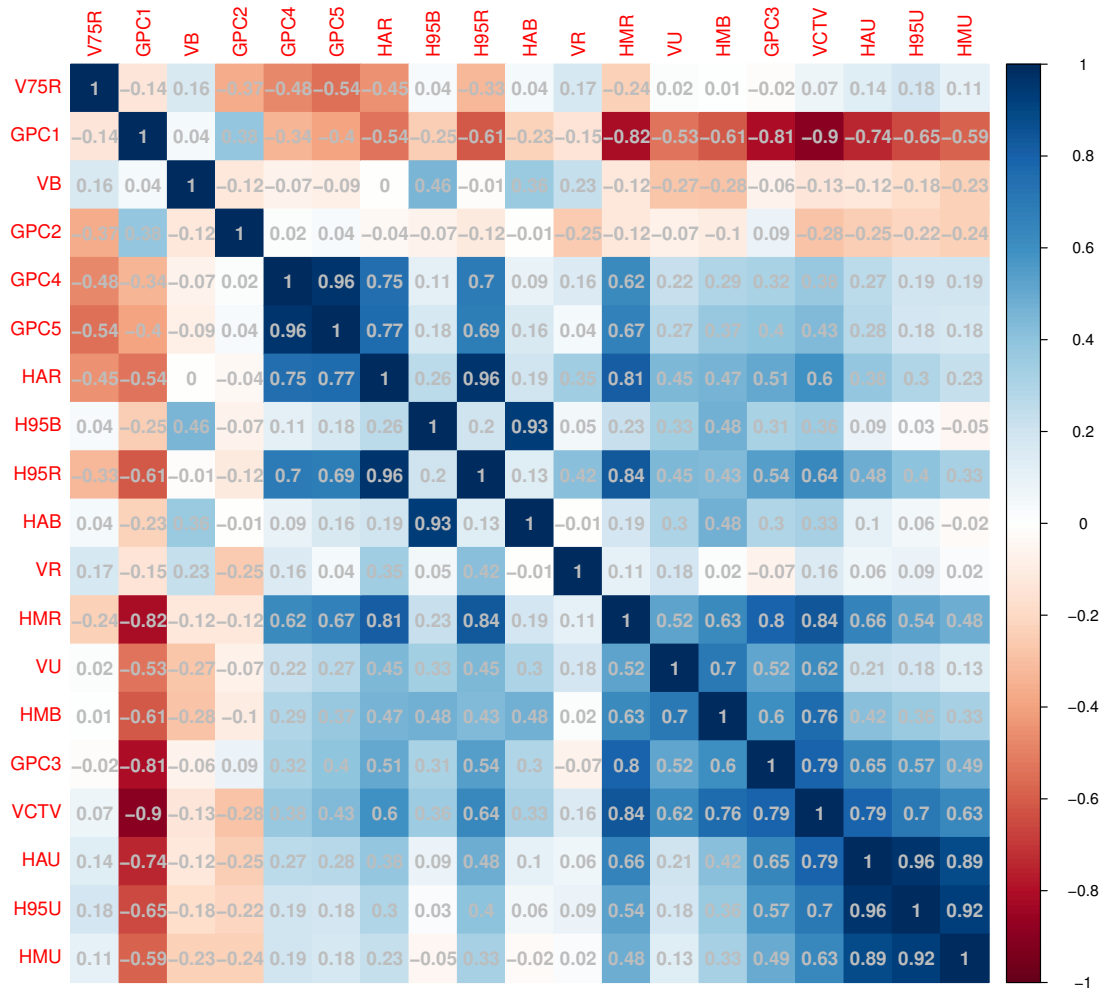

Figure 3.5 – Rectum SCC matrix providing the strength and direction of the SCCs of all the pair parameters between the 18 GPs and the DP (V75) of the rectum. The strength and direction of correlations are exhibited by a color spectrum and a related number. The darkest blue and red show the strongest positive and negative correlations, respectively.

binations were studied, but only the values for the rectum CSFs including 18, 13, 8, 7, 6, and 5 GPs are presented in Table. 3.6. The LRT between the general model including all the 18 parameters and the model with six parameters resulting in the p-value (1) larger than the significance level. Therefore, the alternative model with 18 parameters was rejected and the null model with six parameters was selected. Moreover, the LRT between the alternative model with six GPs and the null model with 5 GPs gave rise to a p-value of 0.0041. Therefore, the null model was rejected and the alternative model with 6 GPs was selected. Note that the other possibilities below $n = 5$ were examined as well, however they are not shown in Table. 3.6.

Consequently, the selected rectum CSF model consists of six dominant GPs including: the volume of the rectum (VR); the HD between the CTV and the maximum volume of the rectum (HMR); the HD between the CTV and the maximum volume of the urethra (HMU); the HD between the CTV and the

Table 3.6 – MLL values for some optimized rectum CSF models including different number of GPs using the TRUS-based HDR-BT plans for prostate cancer. P-value related to the LRT between the selected null and alternative models.

GPs included in each rectum CSF model (TRUS-based)	n	MLL	p-value	Null model	Alternative model	df	Rejected model
All the GPs	18	106.0698					
VCTV, VB, VR, HMR, HAR, H95R, HMU, HAU, H95U, GPC1, GPC2, GPC4, GPC5	13	99.8337	1	13	18	5	Alternative
VB, VR, HMR, HMU, HAU, H95U, GPC2, GPC5	8	98.37778	1	8	13	5	Alternative
VB, VR, HMR, HMU, H95U, GPC2, GPC4	7	94.88882	1	7	8	1	Alternative
VR, HMR, HMU, H95U, GPC2, GPC4	6	96.03932	0.1295	6	7	1	Alternative
VR, HMR, H95U, GPC2, GPC4	5	100.1528	0.0041	5	6	1	Null

95% volume of the urethra (H95VU); the ratio of the area enclosing all the implanted catheters and the maximum surface of the prostate (GPC2); and the minimum distance between the active points of the catheters situated in the lowest portion of the prostate and their closest points on the midplane of the rectum (GPC4). Eq.3.3 provides the dominant GPs and the corresponding optimized weights for the developed rectum CSF.

$$\begin{aligned}\text{Rectum CSF model (TRUS-based)} &= 391.4045 \times (\text{VR}) - 1041.2476 \times (\text{HMR}) \\ &- 1585.6728 \times (\text{HMU}) + 8140.0598 \times (H95U) + 9999.9928 \times (GPC2) \\ &- 3392.6239 \times (GPC4). \end{aligned} \tag{3.3}$$

Fig. 3.6 represents the hundred TRUS-based HDR-BT plans, along with the rectum CSF in Eq.3.3. 71% of these plans were found above the rectum CSF.

3.2.3 Urethra

3.2.3.1 Results of the Spearman Correlation Coefficient and Brute-Force Search for the Urethra Parameters

Fig. 3.7 shows the SCCs associated with all the pair parameters of the urethra. The brute-force search was performed to systematically optimize the models including all the possible combinations of the GPs for the urethra and to calculate the corresponding MLL values. 12 different GPs with larger SCCs values between the GP and dose D10 to the urethra (D10U) were selected. Table. 3.7 provides combinations of these 12 selected GPs for the urethra model. The MLL values were calculated for all the possible combination of the 12 GPs, in other words, a total of 4,095 possible urethra CSFs.

Table 3.7 – The GPs with higher values of the SCC, hence more important correlation, for the dose D10 to the urethra.

	GPC2	VB	H95B	HAB	HMB	VR	GPC1	VCTV	H95R	HAR	VU	GPC4
D10U	-0.4484	0.34	0.3247	0.2851	0.268	0.2626	-0.2012	0.1933	0.1256	0.1197	0.1094	-0.0684

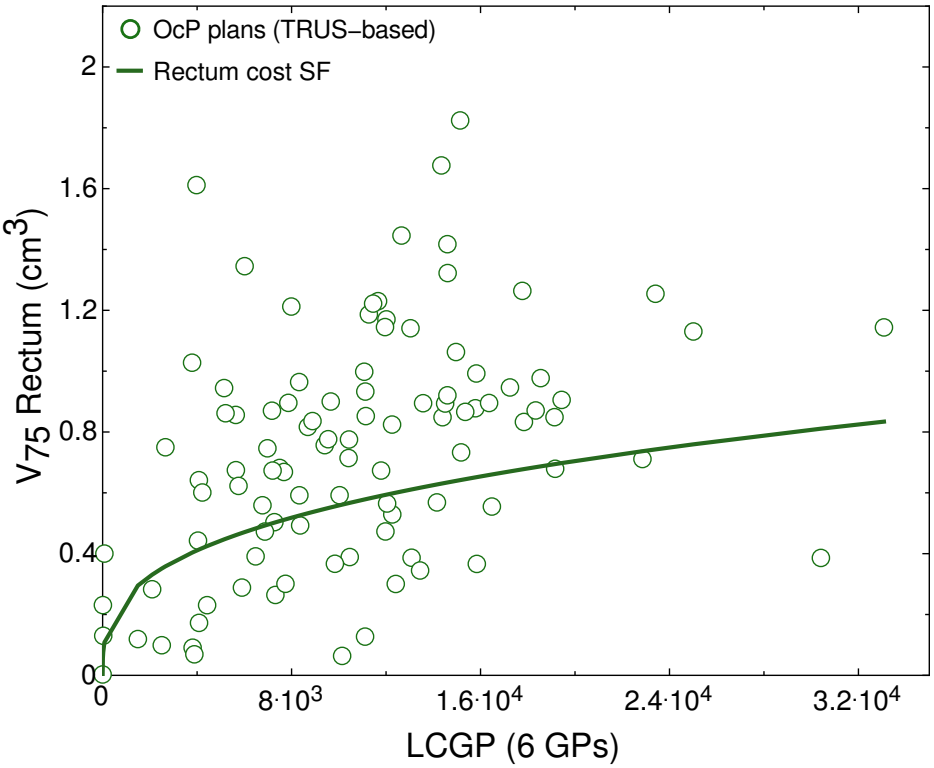

Figure 3.6 – One hundred TRUS-based HDR-BT plans for prostate cancer shown by the empty circles and the developed rectum CSF by the solid line.

3.2.3.2 Urethra Cost Stochastic Frontier

A similar process as described for the other two OARs in 3.2.1.2 and 3.2.2.2 was followed in order to find the optimal urethra model. Negligible technical inefficiency (σ_u) was resulted for almost all the urethra CSF models including different combinations of GPs. Table. 3.8 shows the MLL value associated with some of the urethra models including different GPs. The LRT between each two chosen models were carried out, and the corresponding p-value were evaluated.

Table 3.8 – MLL values for some optimized urethra CSF models including different number of GPs using the TRUS-based HDR-BT plans for prostate cancer. P-value related to the LRT between the selected null and alternative models.

GPs included in each urethra CSF model (TRUS-based)	n	MLL	p-value	Null model	Alternative model	df	Rejected model
All the GPs	18	-214.2277					
VCTV, VB, VR, VU, HMB, HAB, H95B, HAR, H95R, GPC1, GPC2, GPC4	12	-211.4032	0.4636	12	18	6	Alternative
VB, VR, HMB, H95B, GPC1, GPC2	6	-209.4899	0.7001	6	12	6	Alternative
VB, VR, H95B, GPC1, GPC2	5	-208.3598	0.1327	5	6	1	Alternative
VB, VR, H95B, GPC2	4	-205.7679	0.0227	4	5	1	Null

The LRT between the alternative model including all the 18 GPs for the urethra and the null model

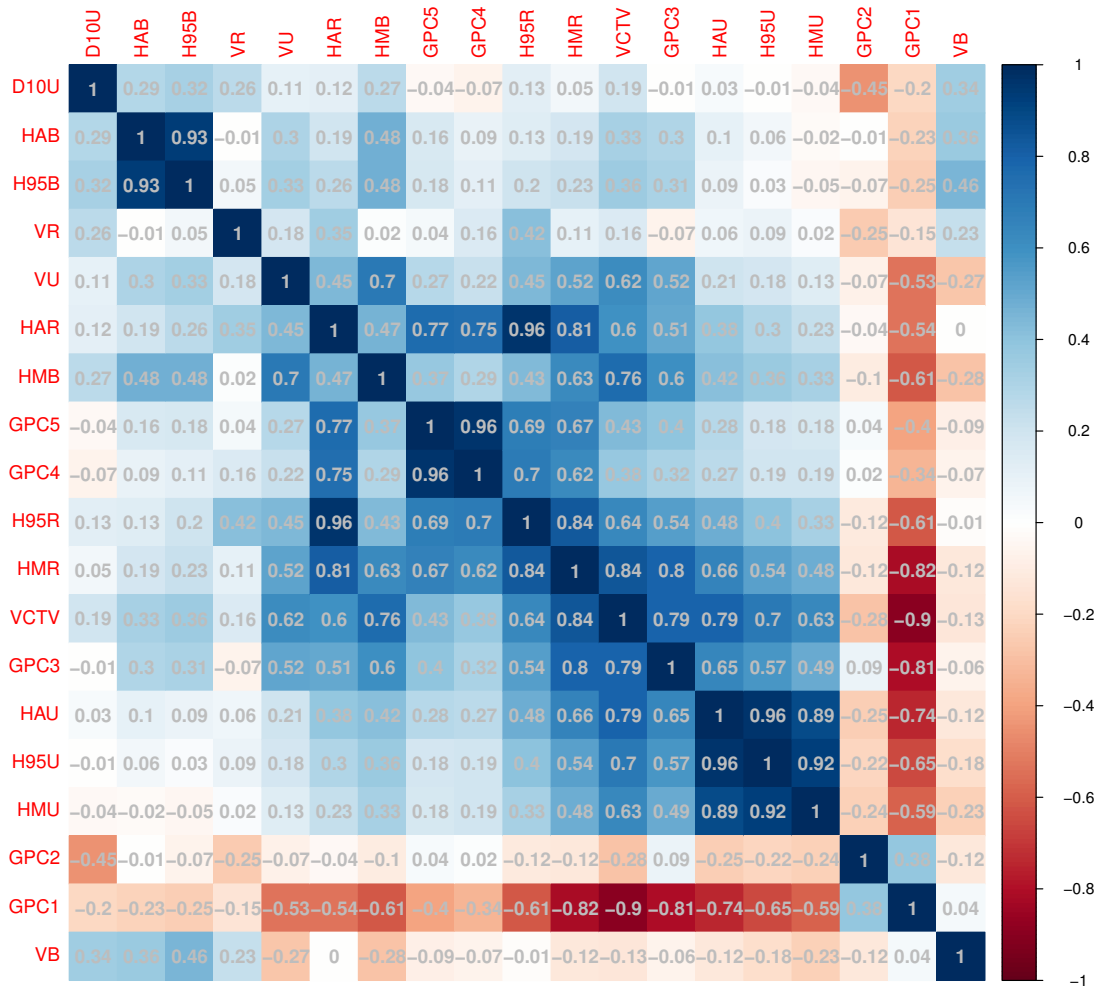

Figure 3.7 – Urethra SCC matrix exhibiting the strength and direction of the SCCs of all the pair parameters between the 18 GPs and the DP (D10) of the urethra. The strength and direction of correlations are shown by a color spectrum and the related number. The darkest blue points to the strongest positive correlation and the red to the strongest negative correlation.

with five parameters resulted in the p-value of 0.2534. Therefore, the alternative model was rejected, and the null model with five GPs was chosen. Moreover, the LRT between the alternative model with five parameters and the null model with four parameters resulted in p-value=0.02. As a result, the null model was rejected, and the model with five GPs was kept. The same test was performed for other possibilities of the urethra model including a lower number of GPs. Consequently, the model including five parameters was selected as the optimal urethra model. This model has five dominant GPs including: the volume of the bladder (VB); the volume of the rectum (VR); the HD between the CTV and the 95% volume of the bladder (H95VB); the ratio of the number of implanted catheters and the maximum surface of the prostate (GPC1); and the ratio of the area enclosing all the implanted catheters and the maximum surface of the prostate (GPC2). Eq.3.4 provides the urethra model. Fig. 3.8 shows the hundred TRUS-based HDR-BT plans for prostate cancer and the developed

urethra model. An equal number of these TRUS-based plans were found above and below the urethra model line.

$$\begin{aligned}\text{Urethra CSF model (TRUS-based)} &= 53.1001 \times (\text{VB}) + 174.4364 \times (\text{VR}) \\ &+ 426.6623 \times (\text{H95B}) - 4.971673 \times (\text{GPC1}) - 9900.526 \times (\text{GPC2}).\end{aligned} \tag{3.4}$$

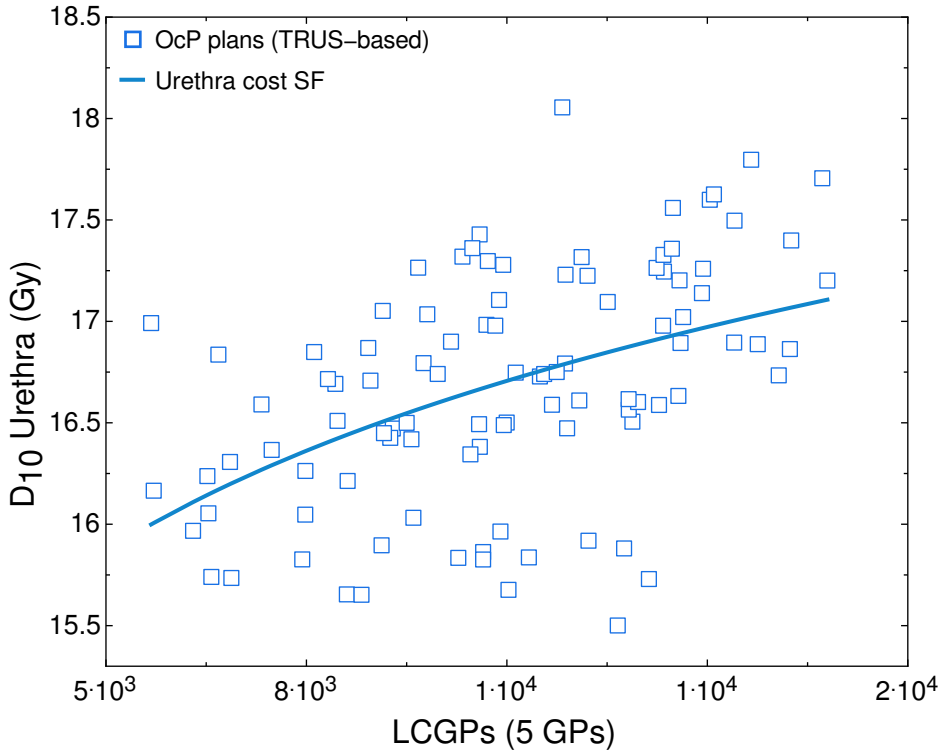

Figure 3.8 – One hundred TRUS-based HDR-BT treatment plans for prostate cancer presented in empty squares. The solid line demonstrates the developed urethra model.

3.3 Application of the Developed SF Models to the CT-based HDR-BT Treatment Plans

So far in this chapter, the target PSF and the bladder, rectum, and urethra CSF models were successfully developed for the TRUS-based HDR-BT treatment for prostate cancer. Now, in this section, we verify whether these SF models succeed to be used on the CT-based HDR-BT plans for prostate cancer. Therefore, a different cohort consisting of one hundred CT-based plans was used to develop a CT-based PSF model for the target. Then, the CT-based PSF model for the target was compared to its corresponding TRUS-based model discussed in 3.1.2. Additionally, a CT-based CSF model was developed individually for each of OARs: the bladder, rectum, and urethra. Finally, comparisons were

performed between each of the bladder, rectum, and urethra CT-based models and the corresponding TRUS-based CSF model, given in 3.2.1.2 3.2.2.2 and 3.2.3.2 respectively. The DPs including the dose V100 to the target, V75 to the bladder, V75 to the rectum, and D10 to the urethra were taken into account as discussed in 2.2. Table. 3.9 provides the average and standard deviation (SD) of these DPs using one hundred CT-based HDR-BT treatment plans for prostate cancer (second cohort). Additionally, the average and SD of these DPs are provided for one hundred TRUS-based HDR-BT plans (first cohort).

Table 3.9 – The average and standard deviation (SD) associated with the DPs including the dose V100 to the target, V75 to the bladder, V75 to the rectum, and D10 to the urethra using one hundred TRUS-based HDR-BT treatment plans for prostate cancer. The results of using one hundred CT-based plans are given as well.

SF model	V100 (%) target TRUS-based	V100 (%) target CT-based	V75 (cm^3) bladder TRUS-based	V75 (cm^3) bladder CT-based	V75 (cm^3) rectum TRUS-based	V75 (cm^3) rectum CT-based	D10 (Gy) urethra TRUS-based	D10 (Gy) urethra CT-based
Average	96.19	96.28	0.824	0.697	0.739	0.672	16.68	16.54
SD	1.5448	1.2528	0.5600	0.2792	0.3839	0.2782	0.5695	0.3747

Note that the objective in this section is to examine if the developed target and OARs SF models for TRUS-based category of HDR-BT treatment are universal. In other words, if the developed SF models can be implemented in another category of the HDR-BT treatment for prostate cancer. Thus, different target PSF and the bladder, rectum, and urethra CSF models are designed using the dominant GPs as in their corresponding TRUS-based SF models. Then, each model is individually applied to one hundred CT-based HDR-BT plans. Following the same optimization process as in the TRUS-based models, the MLL values were calculated. For example, the MLL values were obtained for the CT-based target PSF models including the same GPs as in their corresponding TRUS-based models in Table. 3.2. The LRTs were carried out between the null and alternative models, and the corresponding p-values were evaluated. Therefore, the optimal CT-based target PSF model was determined. Finally, the dominant GPs in this CT-based target PSF model were compared with the GPs in the corresponding TRUS-based target PSF model. The same procedure was followed to find the optimal CT-based bladder, rectum, and urethra CSF models using the models with similar combinations of the dominant GPs as in their corresponding model in Tables.3.4, 3.6, and 3.8, respectively. Tables.3.10, 3.11, 3.12, and 3.13 show the MLL values obtained for all the CT-based target PSF, and the bladder, rectum, and urethra CSF models under investigation. The p-values resulted from the LRTs between different null and alternative models are compared.

Table. 3.10 shows the p-values associated with different LRTs. These LRTs were performed between the null model with a lower number of GPs and the alternative model on its upper row with a larger number of GPs. The CT-based target PSF model with the highest MLL value and the lowest number of GPs has three dominant GPs: VR, HAR, and GPC2. Eq.3.5 gives the the dominant GPs as well as the weights over the GPs in the CT-based target PSF. Fig. 3.9(a) shows one hundred CT-based plans and the developed CT-based target PSF model. 85% of CT-based plans are below the CT-based target

Table 3.10 – MLL calculated for the target PSF models including different number of GPs using the CT-based HDR-BT plans for prostate cancer. The p-value corresponding to LRTs between different null and alternative model are compared. The null model chosen as the model with a lower number of GPs with respect to an alternative model on its higher row with a larger number of GPs.

GPs included in each target PSF model (CT-based)	n	MLL	p-value	Null model	Alternative model	df	Rejected model
All the GPs	18	-297.8254					
VB, VR, HMB, HAB, H95B, HMR, HAR, H95R, GPC2, GPC3, GPC4, GPC5	12	-296.4884	0.8485	12 par.	18 par.	6	Alternative
VB, VR, HMB, H95B, HMR, HAR, GPC4	7	-296.2747	0.994	7 par.	12 par.	5	Alternative
VB, VR, HAB, HAR, GPC5	5	-296.0379	0.7891	5 par.	7 par.	2	Alternative
VR, HMB, GPC2, GPC5	4	-295.2243	0.202	4 par.	5 par.	1	Alternative
VR, HAR, GPC2	3	-295.5493	1	3 par.	4 par.	1	Alternative
VR, HAR	2	-292.622	0.0155	2 par.	3 par.	1	Null

Table 3.11 – MLL calculated for the bladder CSF models with different number of GPs (n) using the CT-based HDR-BT plans for prostate cancer. The LRTs between different null and alternative models are performed, and the resulting p-values are compared.

GPs included in each bladder CSF model (CT-based)	n	MLL	p-value	Null model	Alternative model	df	Rejected model
All the GPs	18	240.722					
VCTV, VB, VR, HAB, HMR, HAR, H95R, HMU, HAU, H95U, GPC1, GPC2, GPC3	13	237.9421	1	13	18	5	Alternative
VB, VR, HAB, HMR, HAU, H95U, GPC1, GPC3	8	238.4298	0.9645	8	13	5	Alternative
VB, HAB, HMR, HAU, H95U, GPC1, GPC3	7	240.317	0.052	7	8	1	Alternative
VB, HAB, HMR, HAU, GPC1, GPC3	6	243.635	0.009	6	7	1	Null

Table 3.12 – MLL calculated for the rectum CSF models with different number of GPs (n) using the CT-based HDR-BT plans for prostate cancer. The LRTs between different null and alternative models are performed, and the resulting p-values are compared.

GPs included in each rectum CSF model (CT-based)	n	MLL	p-value	Null model	Alternative model	df	Rejected model
All the GPs	18	113.493					
VCTV, VB, VR, HMR, HAR, H95R, HMU, HAU, H95U, GPC1, GPC2, GPC4, GPC5	13	116.7086	0.2664	13	18	5	Alternative
VB, VR, HMR, HMU, HAU, H95U, GPC2, GPC5	8	119.2973	0.3946	8	13	5	Alternative
VB, VR, HMR, HMU, H95U, GPC2, GPC4	7	120.3514	0.1465	7	8	1	Alternative
VR, HMR, HMU, H95U, GPC2, GPC4	6	121.5776	0.1173	6	7	1	Alternative
VR, HMR, H95U, GPC2, GPC4	5	121.7648	0.5406	5	6	1	Alternative
VR, HMR, H95U, GPC4	4	121.7945	0.8074	4	5	1	Alternative
VR, H95U, GPC4	3	123.9284	0.0388	3	4	1	Null

Table 3.13 – MLL calculated for the urethra CSF models with different number of GPs (n) using the CT-based HDR-BT plans for prostate cancer. The LRTs between different null and alternative models are performed, and the resulting p-values are compared.

GPs included in each urethra CSF model (CT-based)	n	MLL	p-value	Null model	Alternative model	df	Rejected model
All the GPs	18	-243.6617					
VCTV, VB, VR, VU, HMB, HAB, H95B, HAR, H95R, GPC1, GPC2, GPC4	12	-242.1881	0.8154	12	18	6	Alternative
VB, VR, HMB, H95B, GPC1, GPC2	6	-241.1653	0.9154	6	12	6	Alternative
VB, VR, H95B, GPC1, GPC2	5	-241.3882	1	5	6	1	Alternative
VB, VR, H95B, GPC2	4	-239.1187	0.0331	4	5	1	Null

PSF.

$$\text{Target PSF model (CT-based)} = -1582.595 \times (\text{VR}) + 7755.235 \times (\text{HAR}) - 6578.814 \times (\text{GPC2}). \tag{3.5}$$

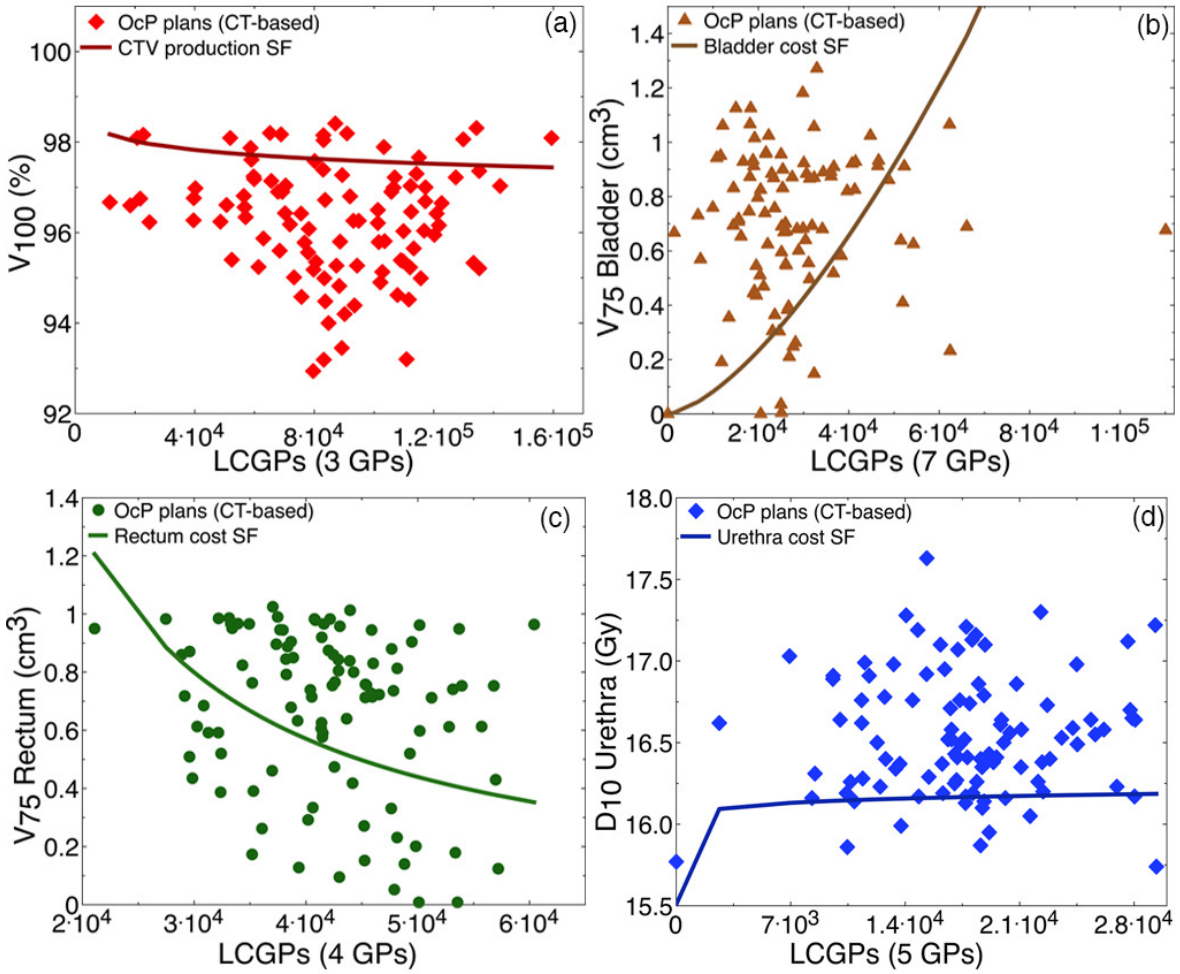

Figure 3.9 – Plots of one hundred CT-based HDR-BT plans for prostate cancer along with The target PSF (a), and the bladder (b), rectum (c), and urethra (d) CSFs.

Fig. 3.10(a) compares the developed target PSFs using the TRUS-based and CT- HDR-BT plans for prostate cancer. The dominant GPs associated with the optimal CT-based target PSF model are equivalent to the GPs in the TRUS-based target PSF model (Table. 3.2). As will later be seen in this section, the shape of the target PSF curves for the CT- and TRUS-based HDR-BT plans are compared. In order to better compare these curves, an outlier (the first plan point in the horizontal axis with V100= 91.96%) was excluded from Fig. 3.2. Fig. 3.10(a) shows the resulting TRUS-based target PSF.

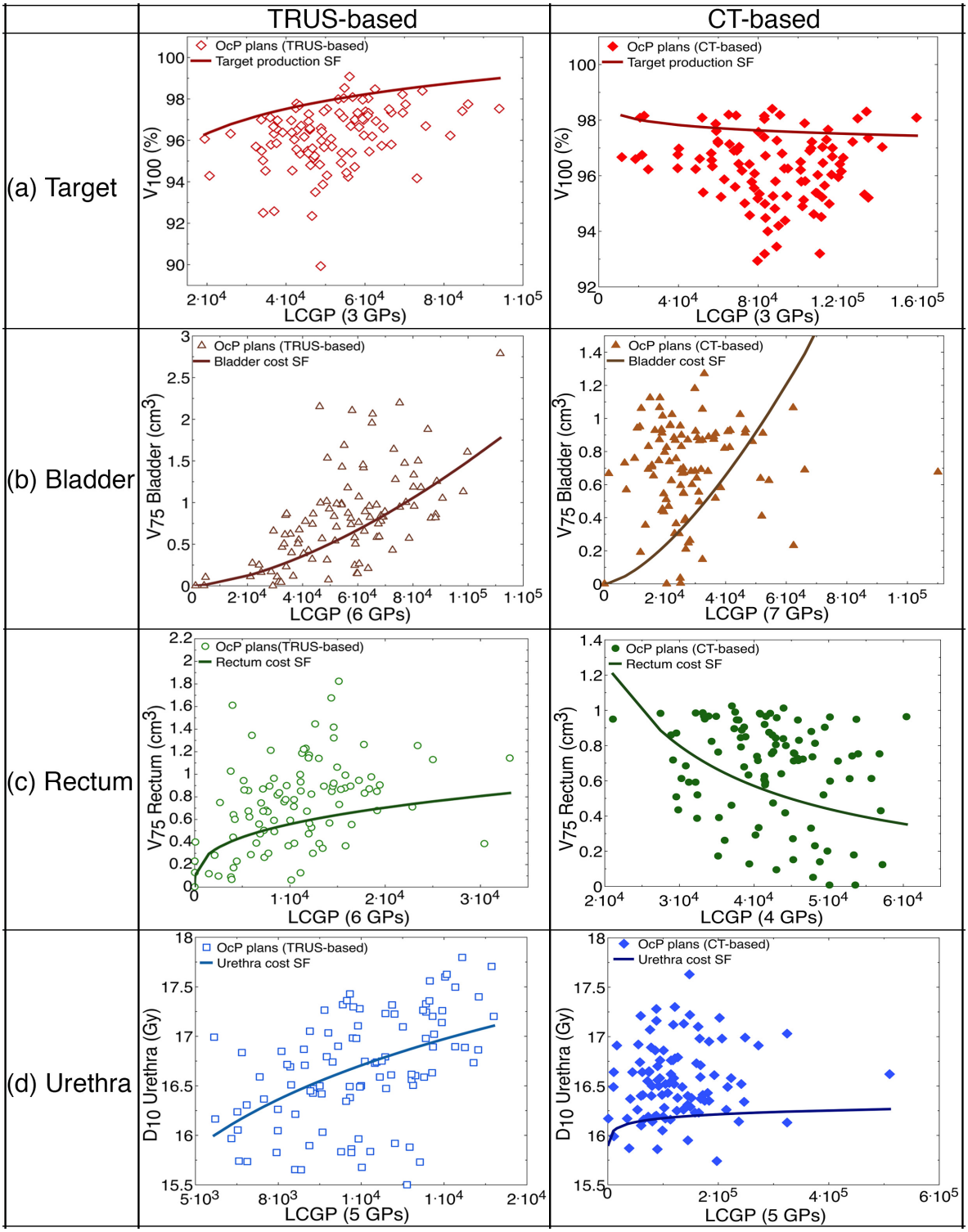

Figure 3.10 – Comparisons between the target PSF models developed, as well as the bladder, rectum, and urethra CSF models, using the TRUS-based and CT-based HDR-BT plans. One hundred TRUS-based and one hundred CT-based HDR-BT plans shown along with the corresponding frontiers.

Table. 3.13 points to the model with five dominant GPs as the optimal CT-based urethra CSF model. These dominant GPs are: VB, VR, H95B, GPC1, and GPC2. Furthermore, Eq.3.6 provides the optimal CT-based urethra CSF model. Fig. 3.9(d) exhibits one hundred CT-based HDR-BT plans along with the developed CT-based urethra CSF model. 88% of these CT-based plans were found above the CT-based urethra CSF.

Moreover, Fig. 3.10(d) compares the optimal urethra CSF model for the CT-based TRUS-based HDR-BT plans for prostate cancer. Identical dominant GPs were obtained for both urethra CSF models using the CT- and TRUS-based HDR-BT plans. Note that an outlier (i.e., the plan point with the lowest LCGP value and a $D_{10} = 15.77$ Gy) was excluded from the CT-based plans in Fig. 3.9(d) in order to better compare the urethra CSF curves associated with the CT- and TRUS-based HDR-BT plans. Eq.3.6 gives the resulting urethra CSF model using CT-based HDR-BT plans excluding one outlier. As opposed to the predicted fit for the urethra model using TRUS-based HDR-BT plans (Fig. 3.8), a stochastic frontier was yielded for the CT-based urethra model.

$$\begin{aligned}\text{Urethra CSF model (CT-based)} * = {} & 2576.366 \times (\text{VB}) + 943.4741 \times (\text{VR}) \\ & - 4913.513 \times (\text{H95B}) - 9981.531 \times (\text{GPC1}) - 9928.864 \times (\text{GPC2}).\end{aligned} \tag{3.6}$$

In the case of the bladder and rectum, however, Tables.3.11 and 3.12, respectively, represents the resulted optimal CSF models including a number of dominant GPs. Following the same method as discussed for the TRUS-based models, the LRTs were performed between the competing null and alternative models, and the corresponding p-values were compared to decide on the optimal SF model using the CT-based plans. As can be inferred from Table. 3.11, the model with seven GPs was chosen as the optimal CT-based bladder CSF model. The seven GPs in the CT-based bladder CSF model are: VB, HAB, HMR, HAU, H95U, GPC1, and GPC3. Eq.3.8 gives the optimal CT-based bladder CSF model. Fig. 3.9(b) illustrates the hundred CT-based HDR-BT plans along with the developed CT-based bladder CSF model. 81% of these CT-based plans were situated above the bladder CSF. Therefore, in contrast to the six dominant GPs obtained for the optimal TRUS-based bladder model (Table. 3.4), the corresponding bladder model using CT-based HDR-BT plans includes seven dominant GPs. Fig. 3.10(b) compares the bladder CSFs for the TRUS-based and CT-based HDR-BT plans for prostate cancer. Moreover, for rectum, Table. 3.12 points out to the model including four dominant GPs as the optimal rectum CSF model using CT-based HDR-BT plans. These four dominant GPs are: VR, HMR, H95U, and GPC4. Eq.3.7 gives the developed CT-based rectum CSF model. Also, Fig. 3.9(c) represents the hundred CT-based HDR-BT plans for prostate cancer along with the corresponding rectum CSF. 69% of these CT-based plans are located above the rectum CSF. As opposed the six dominant GPs determined for the optimal TRUS-based rectum CSF model (Table. 3.6), the optimal CT-based rectum CSF consists of four dominant GPs. Fig. 3.10(c) compares the rectum CSFs associated with the TRUS-based and CT-based HDR-BT plans.

$$\begin{aligned}\text{Rectum CSF model (CT-based)} = {} & -58.8073 \times (\text{VR}) + 812.1918 \times (\text{HMR}) \\ & - 1696.563 \times (\text{H95U}) + 9987.567 \times (\text{GPC4})\end{aligned} \tag{3.7}$$

$$\begin{aligned}\text{Bladder CSF model (CT-based)} &= 539.3829 \times (\text{VB}) - 1966.5788 \times (\text{HAB}) \\ &- 168.25359 \times (\text{HMR}) + 9050.4987 \times (\text{HAU}) - 3586.78959 \times (\text{H95U}) \\ &+ 9851.0892 \times (\text{GPC1}) - 294.6391 \times (\text{GPC3}). \end{aligned} \tag{3.8}$$

According to our discussion in 1.1.1, the contoured volumes of the bladder and rectum in the case of CT-based plans are bigger than the corresponding contours in the TRUS-based plans. The limited capacity of the crystals used in the TRUS equipment yields limitation in the image field-of-view for the TRUS-based HDR-BT treatment for prostate cancer. Furthermore, only the interior part of the rectum can be contoured in the TRUS-based HDR-BT treatment for prostate cancer because the probe tube of TRUS equipment is placed in the rectum. Therefore, as opposed to the CT-based, only fractions of the entire bladder and rectum volumes can be contoured in the TRUS-based HDR-BT for prostate cancer. The bladder volume, as well as the rectum volume, in TRUS-based HDR-BT plans ranges, respectively, from 3.57 cm^3 to 69.33 cm^3, and from 8.45 cm^3 to 29.46 cm^3. Nevertheless, the ranges of the bladder and the rectum volumes in the case of the CT-based plans are, respectively, from 64.65 cm^3 to 304.5 cm^3, and from 29.41 cm^3 to 122.14 cm^3. Furthermore, the volume of the urethra in the TRUS-based plans ranges from 0.75 cm^3 to 2.92 cm^3, which is comparable to the range of the corresponding volume in the CT-based plans from 0.88 cm^3 to 2.63 cm^3. Further, the ranges of the prostate volume in the TRUS-based and CT-based HDR-BT plans are similar. In the TRUS-based plans, the prostate volume ranges from 21.62 cm^3 to 150.39 cm^3, and in the CT-based plans from 33.25 cm^3 to 112.95 cm^3. Moreover, as discussed in 1.2.2, the developed SF models directly depend on the patient-specific geometry knowledge, hence on the GPs. Accordingly, the observed differences in the dominant GPs between the bladder and rectum CSF models for the TRUS-based and CT-based categories of the HDR-BT may arise from the discrepancies in the data associated with dominant GPs applied in each of these models. These discrepancies in the GPs are attributed to the variations in the ways the bladder and rectum are contoured in the case of TRUS-based as compared to the CT-based HDR-BT treatment for prostate cancer.

In order to confirm this hypothesis, one can exclude the extra contouring volumes associated with these structures, and then develop the CT-based SF models based on the modified GPs. In the case of the rectum CSF model, CT-based CSF models including various combination of the modified GPs were designed. For the sake of comparison, the dominant GPs in these CT-based models were chosen according to the CT-based rectum models given in Table. 3.12; however, the modified values of the dominant GPs are taken into consideration. Table. 3.14 represents the MLL values obtained for these rectum CSF models using CT-based HDR-BT plans including the modified GPs. The LRTs were carried out between the null and alternative models within these rectum CSF models, and the corresponding p-values were compared. The LRT, for instance, between the null model with six GPs and the alternative model with all the 18 GPs resulted in a p-value of 1. Therefore, the alternative model was rejected and the null model with six dominant GPs was chosen. Also, the LRT between the null model with five GPs and the alternative model with six GPs yielded a p-value much smaller than the chosen significance level. Therefore, the model with six GPs was selected as the optimal rectum CSF

model in the case of CT-based plans with modified GPs. Eq.3.4 provides the rectum CSF model for the CT-based HDR-BT including the modified GPs. As a result, there are the same six dominant parameter (GPs) in the optimal rectum CSF model using the CT-based HDR-BT plans with modified GPs and in the corresponding model using the TRUS-based plans.

Table 3.14 – MLL obtained for the rectum CSF models including different number of GPs using the CT-based HDR-BT plans for prostate cancer including the modified GPs. p-values corresponding to the LRTs between the null and alternative models are compared.

GPs included in each rectum CSF model (CT-based_Modified)	**n**	**MLL**	**p-value**	**Null model**	**Alternative model**	**df**	**Rejected model**
All the GPs	18	113.8544					
VCTV, VB, VR, HMR, HAR, H95R, HMU, HAU, H95U, GPC1, GPC2, GPC4, GPC5	13	116.8002	0.3169	13	18	5	Alternative
VB, VR, HMR, HMU, HAU, H95U, GPC2, GPC5	8	119.1902	0.4433	8	13	5	Alternative
VB, VR, HMR, HMU, H95U, GPC2, GPC4	7	120.3514	0.1275	7	8	1	Alternative
VR, HMR, HMU, H95U, GPC2, GPC4	6	113.951	1	6	7	1	Alternative
VR, HMR, H95U, GPC2, GPC4	5	121.7648	0.00007	5	6	1	Null

$$\begin{aligned}\text{Rectum CSF model (CT-based-Modified GPs)} &= 266.2561 \times (\text{VR}) - 395.0085 \times (\text{HMR}) \\ &+ 242.3593 \times (\text{HMU}) + 1342.663 \times (\text{H95U}) + 9584.1 \times (\text{GPC2}) - 9876.329 \times (\text{GPC4}). \end{aligned} \quad (3.9)$$

Fig. 3.11(c) exhibits the hundred CT-based plans including the modified GPs along with the corresponding rectum CSF. Fig. 3.11(a) and Fig. 3.11(b) show the comparison between this rectum CSF model for the CT-based plans including the modified GPs and the corresponding models for the TRUS-based and CT-based plans, respectively. As compared to the CT-based (Fig. 3.11(b)), the TRUS-based rectum CSF (Fig. 3.11(a)) has two extra dominant GPs: HMU and GPC2. Moreover, the curves of these TRUS-based and CT-based rectum CSFs exhibited in the Figs. 3.11(a) and (b), respectively, are not identical. Nevertheless, the dominant GPs obtained for the rectum CSF model using the CT-based plans including the modified GPs (Fig. 3.11(c)) and the TRUS-based plans (Fig. 3.11(a)) are in agreement. Also, the curve of the frontier in Fig. 3.11(c) is comparable with the curve of the frontier in Fig. 3.11(a). Therefore, the differences in the GPs and the frontier curves between the CT-based and TRUS-based CSF models for the rectum are due to the variation existed in the contouring of the volumes in the the TRUS-based and CT-based HDR-BT for prostate cancer.

In the case of the target, the CT- and TRUS-based PSFs have the same dominant GPs. However, different curves, as shown in Figs. 3.12(a) and (b), are observed for, respectively, the CT- and TRUS-based PSFs. As mentioned in 3.1.2, the rectum volume is one of the dominant GPs of the target PSF model. Hence, the difference between the two curves for the CT- and TRUS-based PSFs may stem from the variations in the contouring of the volumes between the CT- and TRUS-based HDR-BT treatments for prostate cancer. In order to verify this hypothesis, the extra contoured GPs for the target PSF model in the case of the CT-based plans were discarded following the same procedure as for the rectum. Then, the shape of the target PSF for the CT-based including the modified GPs (Fig. 3.12(c))

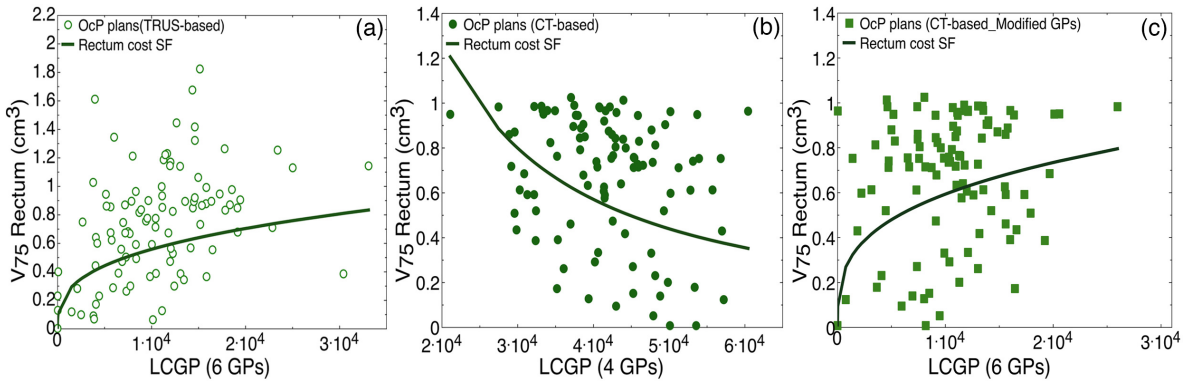

Figure 3.11 – Comparison between the TRUS-based rectum CSF (a) with the corresponding frontiers for the CT-based plans (b), and for the CT-based plans including modified GPs (c). The TRUS-based HDR-BT plans for prostate cancer represented by empty circles, the CT-based plans by full circles, and the CT-based plans including the modified GPs by full rectangles. The corresponding curves for these rectum CSFs shown by solid lines.

was obtained identical to the TRUS-based plans (Fig. 3.12(a)). Eq.3.10 shows the target PSF model using the CT-based plans including the weights over the dominant GPs.

$$\text{Target PSF model (CT-based-Modified GPs)} = 74.25001 \times (\text{VR}) + 1564.696 \times (\text{HAR})$$
$$9855.687 \times (\text{GPC2}). \tag{3.10}$$

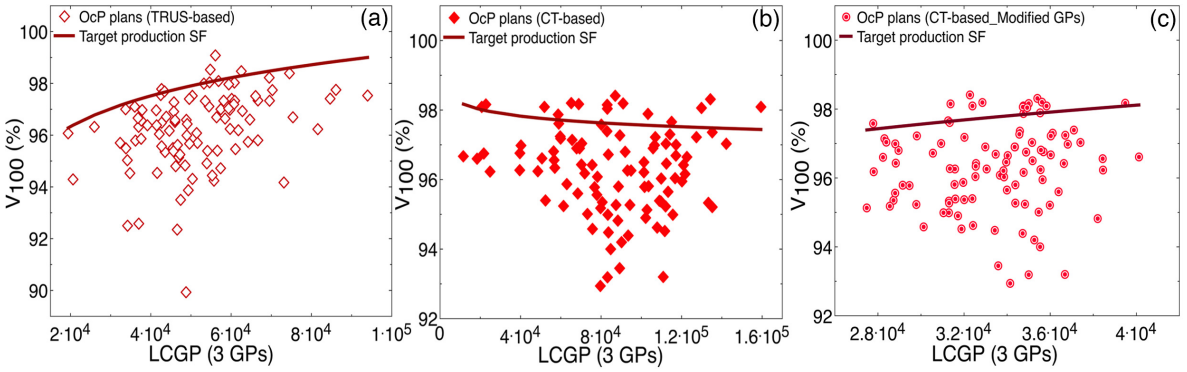

Figure 3.12 – Target PSF model developed for the TRUS-based plans (a) compared with the corresponding model for the CT-based plans (b), and for the CT-based plans including the modified GPs (c). The TRUS-based HDR-BT plans for prostate cancer shown by empty diamonds, the CT-based plans by full diamonds, and the CT-based plans including the modified GPs by full circles. Solid lines represent the corresponding curves for these target PSFs.

In the case of the urethra, a null technical-inefficiency, and a fit was obtained for the TRUS-based urethra model (Fig. 3.13(a)). Additionally, in the CT- (Eq.3.4) and TRUS-based (Eq.3.6) urethra CSF models, the variations in contouring the volumes in TRUS and CT-based HDR-BT treatments for prostate cancer resulted in different values for the parameters such as the rectum volume. These

variations in the contouring, hence in the dominant GPs, may be the cause for the difference observed in the urethra models using TRUS-based and CT-based HDR-BT plans. In order to confirm this hypothesis, the urethra CSF model for the CT-based plans was developed, but this time using the modified values of the dominant GPs. Figs. 3.13(b) and (c) show the resulted urethra CSFs for the CT-based plans and CT-based plans including the modified GPs, respectively. Eq.3.11 provides the urethra CSF using the CT-based plans including the modified GPs as well as the weights over the dominant GPs.

$$\begin{aligned}\text{Urethra CSF model (CT-based Modified GPs)} * = {} & 2992.103 \times (\text{VB}) + 776.3866 \times (\text{VR}) \\ & - 893.5612 \times (\text{H95B}) - 9812.360 \times (\text{GPC1}) - 9971.997 \times (\text{GPC2}),\end{aligned} \tag{3.11}$$

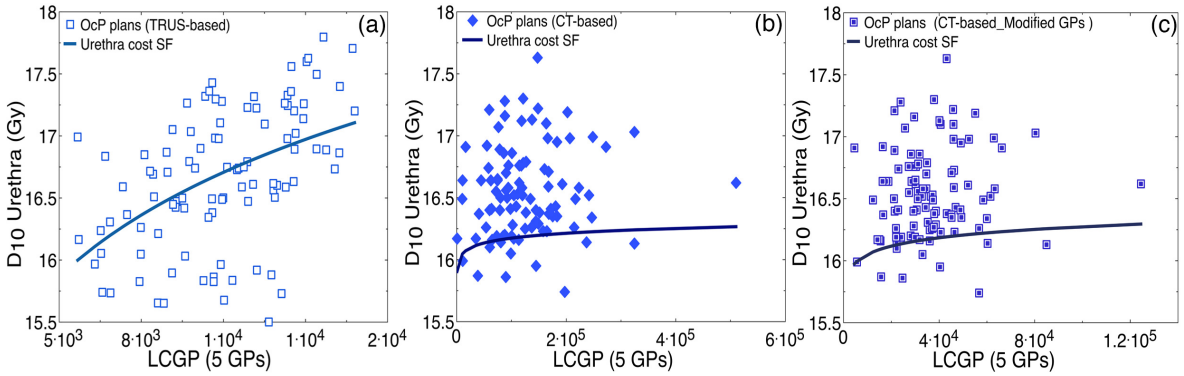

Figure 3.13 – The urethra model developed for the TRUS-based plans (a) compared with the urethra CSFs for the CT-based plans before (b), and after (c) considering the modified dominant GPs. Empty rectangles in (a) represent the TRUS-based HDR-BT plans for prostate cancer, full diamonds in (b) show the CT-based plans, and the full rectangles in (c) the CT-based plans including the modified GPs. The corresponding curves for these urethra CSFs illustrated by solid lines.

As a result, the optimal target PSF model and the rectum and urethra CSF models developed for the TRUS-based HDR-BT treatment for the prostate were shown to include the same dominant GPs as the corresponding models in the CT-based category. Therefore, we confirmed the hypothesis that our target PSF and OARs CSF models developed using TRUS-based HDR-BT plans for prostate cancer, can be used for the CT-based category of the HDR-BT treatment. Therefore, the developed SF models can perform well outside of the TRUS-based category of the HDR-BT treatment for prostate cancer. In other words, the developed SF models are universal.

The dominant GPs, along with the corresponding weights were obtained for all the developed optimal TRUS-based and CT-based (modified GPs) target PSF and bladder, rectum, and urethra CSF models. These weights of the dominant GPs were evaluated through the optimization of the corresponding SF model explained in 2.4. All the dominant GPs in the target PSF models associated with the TRUS-based and CT-based (modified GPs) HDR-BT plans for prostate cancer, as given, respectively, in Eqs.3.1 and 3.10 are identical. These dominant GPs include the volume of the rectum (VR), the

HD average between the target and rectum volume (HAR), and the ratio of the area enclosing all the implanted catheters and the maximum surface of the prostate (GPC2). The HAR and GPC2 parameters impact positively the target covering in the TRUS-based as well as the CT-based (modified GPs) target PSF models. A comparison between the weights obtained for all the dominant GPs in the TRUS-based and CT-based (modified GPs) target PSF models showed that GPC2 has the most significant influence on the target (V100) covering. A greater ratio of the area including all the inserted catheters and the maximum surface of the prostate (i.e., GPC2) indicates delivering the dose of radiation to a larger regions of the target: hence, increased the dose V100 to the target. Further, as discussed in 2.3.2, HD measurements take into account not only the distances between the two structures but also their distinct shapes. Therefore, the differences between the two structures in term of their shapes and distances are provided by HD measurements. As stated above, a positive impact of the HAR parameter on the target V100 covering were obtained in both the TRUS-based and CT-based (modified GPs). Therefore, when the HAR parameter augments, the TRUS-based and CT-based HDR-BT plans will shift towards the target PSFs and above this production frontier. In the case of the parameter related to the volume of the rectum (VR), as opposed to the negative impact on the target covering obtained related to the VR parameter in the TRUS-based target PSF model, a positive impact was observed for VR in the CT-based (modified GPs) target PSF model.

In the case of the rectum, both the TRUS-based and CT-based (modified GPs) CSF models given in Eqs.3.3 and 3.9, respectively, include the same dominant GPs. These six dominant GPs are the volume of the rectum (VR), the HD maximum between the target and the rectum (HMR), the HD maximum between the target and the urethra (HMU), the HD 95% between the target and the urethra (H95U), the ratio of the area enclosing all the implanted catheters and the maximum surface of the prostate (GPC2), and finally, the minimum distance between the active points of the catheters placed in the lowest portion of the prostate and their closest points on the midplane of the rectum (GPC4). In the TRUS-based and the CT-based (modified GPs) rectum CSF models, the VR, H95U, and GPC2 parameters exhibited a positive impact on the dose V75 received by the rectum. Indeed, greater dose V75 to the rectum is associated with larger volumes of the rectum (VR). Furthermore, HDs point out the dissimilarities between the two structures in term of distance and shape. It should be noted that since the urethra is situated within the target, the distance between the target and urethra is irrelevant. Therefore, only the shape of the structure is considered in H95U. A positive weight was obtained for the H95U parameters in both the TRUS-based and the CT-based (modified GPs) rectum CSF models. Also, the resulted weight associated with the HMU parameter in the rectum CSF model showed a negative influence on the dose V75 to the rectum. This is contrary to the positive weight obtained for the HMU parameter in the rectum CSF model developed using CT-based (modified GPs) plans. Further, in the case of the TRUS-based target PSF model, the GPC2 parameter has the most substantial influence on the dose V75 to the rectum. In other words, the ratio of the area enclosing all the inserted catheters and the maximum surface of the prostate is of higher importance as compared with the other GPs in the rectum CSF model using TRUS-based HDR-BT plans for prostate cancer. In the case of the CT-based (modified GPs) rectum CSF model, the most important impact on the dose V75 to the

rectum was acquired related to the GPC4 parameter. The GPC4 parameter impact negatively the dose V75 to the rectum in the TRUS-based and the CT-based (modified GPs) rectum CSF models. When the minimum distance between the dwell positions related to the catheters situated in the lowest part of the prostate and their nearest points on the midplane of the rectum (i.e., GPC4) increases, the dose V75 to the rectum is reduced. Additionally, negative weights were obtained associated with the HMR parameters in both the TRUS-based and CT-based (modified GPs) rectum CSF models. Hence, the increase in the HMR parameter indicates the decrease in the dose V75 to the rectum.

In the case of the last OAR, urethra, five identical dominant GPs were determined in the TRUS-based as well as the CT-based (modified GPs) models, given in Eqs.3.4 and 3.11, respectively. These five dominant GPs are the volume of the bladder (VB), the volume of the rectum (VR), the HD 95% between the target bladder (H95B), the ratio of the number of implanted catheters and the maximum surface of the prostate (GPC1), and the ratio of the area enclosing all the implanted catheters and the maximum surface of the prostate (GPC2). The VB and VR parameters showed a positive impact on the dose D10 to the urethra in both the TRUS-based and CT-based (modified GPs) CSF models. Contrarily, the GPC1 and GPC2 parameters both revealed negative impacts on the dose D10 to the urethra in the TRUS-based and CT-based (modified GPs) urethra models. Moreover, the weight associated with the H95B parameter on the dose D10 to the urethra was found to be positive. However, this weight (H95B) was obtained negative in the case of CT-based (modified GPs) urethra CSF model.

Additionally, Table. 3.15 shows the results predicted by the developed SF models using the cohort including one hundred TRUS-based and the cohort with one hundred CT-based HDR-BT treatment plans for prostate cancer. The number of the plans above the target PSF and below the bladder, rectum, and urethra CSFs in each cohort under study are provided. 94% of the TRUS-based plans in the first

Table 3.15 – The percentage of the TRUS-based and CT-based plans predicted to be below and above the target PSF and bladder, rectum, and urethra CSFs, respectively.

	Number of plans below the target PSF	Number of plans above the bladder CSF	Number of plans above the rectum CSF	Number of plans above the urethra CSF
TRUS-based	94%	63%	71%	50%
CT-based	85%	81%	69%	88%

cohort were positioned under the developed TRUS-based target PSF. Additionally, 63% and 71% of these plans were found above the bladder and rectum CSFs, respectively. In the case of the urethra, 50% of the TRUS-based plans were placed above and 50% below the urethra model. It should be noted that finding a treatment plan under the target PSF or above the bladder, rectum, and urethra CSFs do not point to a clinically unacceptable plan in the HDR-BT treatment for prostate cancer. The optimization of all the plans under study was provided a clinically acceptable dose V100 to the target, V75 to the bladder and rectum, and D10 to the urethra. In other words, the optimization of all these plans was carried out in agreement with the ABS recommendations for each of the dose criteria in the HDR-BT treatment for prostate cancer. However, the observed differences between the plans optimized by the TPS and the ones predicted by the developed SF models point out to the possibility of

further improvement in the target covering and OARs dose minimization for these plans under investigation. For instance, the target covering can be improved for 94% of the patients in the TRUS-based plans. Furthermore, using the TRUS-based bladder and rectum CSF models indicate that the irradiated volume of the bladder and rectum can be reduced for, respectively, 63% and 71% of the patients in the TRUS-based plans. Accordingly, there is room to spare a greater volume of the bladder and rectum for, respectively, 63% and 71% of the patients in the TRUS-based plans under study. Furthermore, the predictive power of the developed SF models was examined using the hundred CT-based HDR-BT treatment plans for prostate cancer in the second cohort. 85% of the CT-based plans were positioned under the CT-based target PSF. Hence, the target PSF predicted that the target covering could be improved for 85% of the plans in the CT-based HDR-BT plans under study. Additionally, 81% of these CT-based plans under study were placed above the bladder, 69% above the rectum, and 88% above the urethra CSFs. Therefore, the dose received by the bladder, rectum, and urethra could be minimized for the 81%, 69%, and 88% of the CT-based plans, respectively.

Table. 3.16 provides the developed optimal SF models for the two category of the HDR-BT treatment for prostate cancer, i.e., the TRUS-based and CT-based. The number (n) and the type of the dominant GPs included in each of these TRUS-based and CT-based optimal models for the target PSF and for the bladder, rectum, and urethra CSF models are given. MLL values are obtained through optimization of the SF models using the hundred TRUS-based as well as the CT-based HDR-BT treatment plans for prostate cancer. Furthermore, the statistics of the probability density of ε, the mean (E(ε)) and the variance (V(ε)), were evaluated for each of these SF models. Moreover, the standard deviation (SD) of the two error terms; the technical inefficiency (σ_u) and the random noise (σ_v) in Eq.1.17 or Eq.2.9 were calculated. The model parameters, a_0 and a_1 in Eq.1.13, were obtained for each model as well. A technical inefficiency of $\sigma_u = 0.0219$ was obtained for the target PSF using the TRUS-based HDR-BT plans, which is contrary to the urethra CSF model with a null technical inefficiency. Therefore, using the developed target PSF model predicted a larger improvement in the target covering as compared with the minimization of the dose D10 to the urethra using the TRUS-based HDR-BT plans. Thus, the urethra was found to be the organ for which the minimization of the dose is well optimized in TRUS-based HDR-BT treatment plans. In other words, no variability was related to the planners' competency and judgment in the optimization of the urethra in the TRUS-based HDR-BT plans. In fact, medical physicists, under the recommendation of radiation oncologists, put many efforts in the minimization of dose to the urethra. Indeed, hundred percent (i.e., the highest) technical efficiency is associated with the minimization of the dose D10 to the urethra using the TRUS-based HDR-BT plans. Consequently, no further improvement of the dosimetric parameter D10 for the urethra was possible based on the developed urethra CSF model using the TRUS-based plans under study. The most significant technical inefficiency between the OARs sparing in the TRUS-based HDR-BT plans under study was predicted based on the rectum CSF model for the minimization of the dose V75 to the rectum ($\sigma_u = 0.208$).

In comparison to the bladder, a higher mean, $E(\varepsilon) = 0,166$, was obtained for the minimization of the

Table 3.16 – The number of the dominant GPs (n), the dominant GPs, the optimized MLL, the model parameters a_0 and a_1, the mean E(ε), the variance V(ε), and the standard deviation (SD) of the two error terms (i.e., σ_u and σ_v) calculated for all the optimal TRUS-based and CT-based SF models.

SF model	n	Dominant GPs	MLL	σ_u	σ_v	a_0	a_1	E(ε)	V(ε)	SD
TRUS-based target PSF	3	VR, HAR, GPC2	-291.2876	0.0219	0.0049	4.44581	0.01390	-0.0175	0.0002	0.0141
TRUS-based bladder CSF	6	VB, HAB, HMR, HAU, GPC1, GPC3	131.4082	0.1028	0.8987	-17.54720	1.55900	0.0820	0.8115	0.9008
TRUS-based rectum CSF	6	VR, HMR, HMU, H95U, GPC2, GPC4	96.03753	0.2081	0.6200	-3.66957	0.33517	0.1660	0.4001	0.6326
TRUS-based urethra CSF	5	VB, VR, H95B, GPC1, GPC2	-208.3598	0.0000	0.0301	2.20701	0.06542	0.0000	0.0009	0.0301
CT-based target PSF	3	VR, HAR, GPC2	-295.5493	0.0174	0.0074	4.6133	-0.0028	-0.0139	0.0002	0.0128
CT-based bladder CSF	7	VB, HAB, HMR, HAU, H95U, GPC1, GPC3	240.317	0.4314	2.6696	-16.2794	1.4964	0.3442	7.1944	2.6822
CT-based rectum CSF	4	VR, HMR, H95U, GPC4	121.7945	0.0004	0.8	11.3983	-1.1348	0.0003	0.6400	0.8000
CT-based urethra CSF *	5	VB, VR, H95B, GPC1, GPC2	-239.6553	0.0284	0.0136	2.74314	0.00349	0.0227	0.0005	0.0219
CT-based modified GPs target PSF	3	VR, HAR, GPC2	-295.9722	0.0189	0.0063	4.3785	0.0195	-0.0151	0.0002	0.0130
CT-based modified GPs rectum CSF	6	VR, HMR, HMU, H95U, GPC2, GPC4	113.951	0.0089	0.7604	-3.3521	0.3073	0.0071	0.5782	0.7604
CT-based modified GPs urethra CSF *	5	VB, VR, H95B, GPC1, GPC2	-239.7017	0.0291	0.0131	2.72043	0.00600	0.0232	0.0005	0.0219

dose V75 to the rectum through the rectum CSF model using the TRUS-based HDR-BT plans. Higher technical inefficiency for the rectum predicts higher variations in the quality of the TRUS-based HDR-BT plans. As discussed in 1.2.2, a higher technical inefficiency can be linked to a higher variation in the planners' experience and judgment. The bladder CSF model predicted that further improvement in the minimization of the dose V75 to the bladder was possible in the TRUS-based HDR-BT plans. However, this improvement would be on a smaller scale as compared with the dose V75 to the rectum. Therefore, the developed rectum CSF model can provide predictive information on how to improve the minimization of the dose V75 to the rectum in the TRUS-based HDR-BT treatment for prostate cancer.

Table. 3.16 shows that the technical inefficiency of the target covering ($\sigma_u = 0.017$) and the urethra sparing ($\sigma_u = 0.028$) is of the same order of magnitude using the CT-based HDR-BT plans in the second cohort separately. Furthermore, the highest variability in the planner's experience and judgment in the CT-based HDR-BT plans under study was related to the minimization of the dose V75

to the bladder ($\sigma_u = 0.431$). As compared to the other OARs in the CT-based plans, larger mean ($E(\varepsilon) = 0.344$) was obtained for the bladder. Moreover, the lowest technical inefficiency in the CT-based HDR-BT plans was associated with minimization of the dose V75 to the rectum $\sigma_u = 0.0004$ with the mean $E(\varepsilon) = 0.0003$. In other words, rectum was found as the OARs the most spared in the CT-based HDR-BT treatment plans under investigation.

Additionally, the comparison between the two developed target PSF models using the TRUS-based and CT-based HDR-BT plans individually revealed that the technical inefficiencies predicted by the models in the two cohorts have the same order of magnitude. However, slightly larger technical inefficiency was obtained for the target PSF model using the TRUS-based ($\sigma_u = 0.0219$) than for the corresponding model using the CT-based ($\sigma_u = 0.0174$) HDR-BT plans under study. Furthermore, a better balance between the target covering and urethra sparing was predicted for the TRUS-based plans rather than the CT-based HDR-BT plans under study. Therefore, a more critical improvement for the trade-off between the target covering and urethra sparing was predicted based on the urethra CSF model using the CT-based, as compared to the TRUS-based HDR-BT plans for prostate cancer.

As compared with the TRUS-based HDR-BT plans, the developed bladder CSF models predicted more considerable variability between the clinically optimized treatment plans for the CT-based plans. Moreover, larger values of the mean and the corresponding SD of the ε was predicted by the bladder CSF model using the CT-based plans ($E(\varepsilon) = 0.344$, SD=2.68) in comparison with the TRUS-based plans ($E(\varepsilon) = 0.083$, SD=0.90). Thus, the bladder CSF model predicted a considerable dispersion associated with the implanter variability. This is because of the greater variability in the catheter geometry at the tip of the catheters, which is also the closets to the bladder.

As shown in Table. 3.16, the technical inefficiency of the rectum CSF model for the CT-based plans ($\sigma_u = 0.0004$) is negligible in comparison with the one for the TRUS-based plans under study ($\sigma_u = 0.2081$). The very low technical inefficiency obtained for the CT-based plans indicates that rectum is the OAR that was better optimized in the case of the CT-based plans in comparison to the TRUS-based HDR-BT plans under study. In other words, lower variations due to planners' experience and judgments in minimization of the dose V75 to the rectum was predicted for the CT-based plans as compared with the TRUS-based HDR-BT plans. It should be noted that in the TRUS-based HDR-BT treatment for prostate cancer, the presence of the TRUS tube in the rectum can affect the shape of the rectum wall, prostate, and its adjacent anatomy. The separation between prostate and rectum due to the impact of the presence of the TRUS probe in HDR-BT treatment was studied by Rylander *et al.* (189). The distance between the prostate and rectum, as well as the rectal DVH parameters for HDR-BT for prostate, were compared for two different cases; one case with, and the other case without the TRUS probe in place during the dose delivery. An increase of 1 cm of the median distance at the base of the prostate was observed due to the variation in distance between the prostate and the anterior rectal wall. Also, the decrease of 0.2 cm at the apex was reported (189).

The comparison between the urethra model for the TRUS-based and CT-based HDR-BT plans under

investigations showed that, as opposed to the null technical inefficiency in the case of the TRUS-based plans, a relatively small technical inefficiency ($\sigma_u = 0.0284$) was obtained for the CT-based HDR-BT plans under study. The more critical technical inefficiency associated with the urethra sparing in the CT-based plans relative to the TRUS-based plans can be linked to the more significant variations exist in the planners' experience and judgment in minimization of the dose D10 to the urethra in the case of CT-based plans. In fact, in the case of the CT-based HDR-BT treatment plans under study, less control existed on the precision of the needle positioning. Changes in needle positioning can occur when the patient's legs are lowered in order to acquire the CT images. As a result, potential errors in the distance between the needles and the urethra in the CT-based plans can be more significant than in the TRUS-based plans. This confirms that it is not just the planner's experience but rather team experience globally: how the catheters are implanted changes what it is possible to do on the planning side of the HDR-BT treatment for prostate cancer.

Table. 3.16, also, represents a comparison of the mean and the SD of the ε between different TRUS-based and CT-based SF models. The target covering and the average of all the bladder, rectum, and urethra (OARs) sparing were compared between the TRUS-based and CT-based HDR-BT plans under investigation. The target PSF model predicted a similar target covering for the TRUS-based ($E(\varepsilon) = -0.0175$, SD=0.014) and for the CT-based ($E(\varepsilon) = -0.0139$, SD=0.012) HDR-BT plans. However, the average OAR sparing was better performed in the case of the TRUS-based plans ($E(\varepsilon) = 0.082$, SD=0.521) rather than the CT-based ($E(\varepsilon) = 0.122$, SD=1.16) HDR-BT plans. Higher values of the mean and SD of ε obtained for the average of the OARs sparing in the CT-based in comparison with the TRUS-based plans showed a larger variation of planner's experience and judgment in the minimization of the dose to the OARs in CT-based HDR-BT plans. As compared with the TRUS-based plans, a larger number of the CT-based plans were founded for which despite having a similar dominant GPs, the optimization of the dose to the OARs was performed differently. Therefore, the developed bladder, rectum, and urethra CSF models predicted more important improvement of the optimization of the dose received by each of the OARs in the case of the CT-based plans in comparison with the TRUS-based plans.

Conclusion

The SF analysis, a model in economics, was successfully applied to develop the QC tool based on the patient-specific anatomic knowledge. The treatment plans of previous patients treated by the TRUS-based HDR-BT were employed to develop the SF models. The purpose was to provide treatment planners for the HDR-BT treatment for prostate cancer with a geometry-based QC tool. This QC tool allows planners to base their decision-making process on quantitative factors, rather than only based on subjective methods. It should be noted that practical or subjective methods should still, but to a lesser extent, be taken into consideration in the treatment planning process. However, the QC tool can be used as a quantitative benchmark to provide planners, before the planning, with the knowledge on how to cope with the challenge of attaining a trade-off between target-coverage and OARs-sparing. Consequently, the quality of planning for the HDR-BT treatment for prostate cancer is improved.

To develop the SF models, one hundred clinical HDR-BT treatment plans for prostate cancer were used in this research project, in which TRUS was employed as the only imaging modality. Furthermore, a single fraction of 15 Gy was prescribed for these patients. The clinical optimizations of these TRUS-based HDR-BT plans were carried out using the IPSA algorithm. Additionally, OcP TPS was used. Moreover, the ABS recommendations for the dose parameters were followed for the target (CTV), and the three OARs: bladder, rectum, and urethra. The DPs include: V100 of the target; V75 of the bladder; V75 of the rectum; and D10 of the urethra. These DPs were extracted for all the clinical patients in the TRUS-based cohort.

In total, 18 different GPs were taken into account in this study. Thirteen of these GPs are associated with the geometry of the patient. These GPs include the volume of the CTV, bladder, rectum, and urethra, as well as the Hausdorff distance (HD) between the prostate and the three OARs. Furthermore, five of these GPs are related to the implanted catheters within the prostate. These catheter-related GPs consist of the ratio of the number of implanted catheters and the maximum surface of the prostate; the ratio of the area enclosing all the implanted catheters and the maximum surface of the prostate; the average distance between all the implanted catheters, and the minimum distance between the active points of the catheters placed in the lowest portion of the prostate and their closest points on the midplane and full length of the rectum.

The SCC approach was used to study the relationships between the GPs and DPs of interest. Examining the monotonic relationships between the GPs and DPs provided information regarding the

dominant GPs in a given SF model. Subsequently, to systematically explore all the possible combinations of the dominant GPs, and to optimize the corresponding SF models, brute-force searches and parallel computations were carried out in the statistical computing package R. Indeed, the optimization of each of the SF models was performed using a maximum likelihood method implemented in the R, and its GenSA algorithm. Then, in order to make a comparison between the optimized SF models including different combinations of GPs, the LRT and its corresponding p-value were employed. The LRT and its p-value indicate the accepted or rejected model between the two competing models: the null and alternative models. As a result, an optimal PSF model for the target, and an optimal CSF model for each of the bladder, rectum, and urethra were developed using the TRUS-based HDR-BT for prostate cancer.

Based on the SCCs matrices evaluated individually for the target as well as each of the OARs, the GPs with a more significant correlation to the dose V100 to the target, V75 to the bladder and rectum, and D10 to the urethra were selected. Different possible combinations were studied using the dominant GPs for the target PSF, bladder, rectum, and urethra CSF. These possible target PSF and OARs CSF models were optimized in different brute-force searches, and parallel computations in R. In the brute-force searches for the target, bladder, rectum, and urethra, a total of, respectively, 4,095, 8191, 8191, 4095 possible combinations of the GPs were studied. Consequently, the optimal target PSF and bladder, rectum, and urethra CSF models comprise three, six, six, and three GPs, respectively. Table. C.1 provides the dominant GPs for the optimal target PSF and bladder, rectum, and urethra CSF models for the TRUS-based HDR-BT.

The following step was to examine if the developed TRUS-based target PSF and the bladder, rectum, and urethra CSF models may be generally used for another category of the prostate HDR-BT. We verified whether or not the four developed TRUS-based SF models could be applied for the CT-based HDR-BT plans for prostate cancer. Therefore, we designed CT-based SF models for the target PSF and bladder, rectum, and urethra CSF including the same GPs as in their corresponding TRUS-based SF models. After, we examined if each of the optimal target PSF or OARs CSF models developed using the CT-based HDR-BT plans has the same GPs as its corresponding optimal TRUS-based SF model. The optimal SF model was chosen using the evaluated MLL values, and based on the LRTs and the corresponding p-values. The evaluation of these MLL value was carried out through optimization using the same method of the maximum likelihood implemented in the R and also its GenSA algorithm. It should be noted that the second cohort used in this research consisted of one hundred clinical HDR-BT treatment plans for prostate cancer, in which CT was used as the imaging modality rather than TRUS. These plans were all associated with the patients who were treated with a single fraction of 15 Gy. The planning of all these CT-based HDR-BT treatment plans was done using the IPSA algorithm implemented in the OcB TPS (Nucletron, Veenendaal, The Netherlands). The DPs taken into consideration for the CT-based SF models were similar to those for the TRUS-based models. Furthermore, the same as for the TRUS-based models, 18 GPs were used for the TRUS-based models.

Table C.1 – The optimal target PSF and bladder, rectum, and urethra CSF models for the TRUS-based, CT-based, and CT-based including the modified GPs HDR-BT plans for prostate cancer. The number of the dominant GPs (n), the dominant GPs, the percentage of the plans above and under each SF, the technical inefficiency (σ_u), the ratio of the two error terms (i.e., σ_u and σ_v), the expectation E(ε), and the standard deviation (SD) of the two error terms evaluated for the given SF models.

SF model	**n**	**Dominant GPs**	**Plans under the SF (%)**	**Plans above the SF (%)**	**Tech. inefficiency (σ_u)**	σ_u/σ_v	**E(ε)**	**SD**
TRUS-based target PSF	3	VR, HAR, GPC2	94	6	0.0219	4.469	-0.0175	0.0141
CT-based target PSF	3	VR, HAR, GPC2	85	15	0.0174	2.351	-0.0139	0.0128
CT-based modified GPs target PSF	3	VR, HAR, GPC2	-	-	0.0189	3	-0.0151	0.0130
TRUS-based bladder CSF	6	VB, HAB, HMR, HAU, GPC1, GPC3	37	63	0.1028	0.114	0.0820	0.9008
CT-based bladder CSF	7	VB, HAB, HMR, HAU, H95U, GPC1, GPC3	19	81	0.4314	0.161	0.3442	2.6822
TRUS-based rectum CSF	6	VR, HMR, HMU, H95U, GPC2, GPC4	29	71	0.2081	0.335	0.1660	0.6326
CT-based rectum CSF	4	VR, HMR, H95U, GPC4	31	69	0.0004	0.0005	0.0003	0.80
CT-based modified GPs rectum CSF	6	VR, HMR, HMU, H95U, GPC2, GPC4	-	-	0.0089	0.0117	0.0071	0.7604
TRUS-based urethra CSF	5	VB, VR, H95B, GPC1, GPC2	50	50	0.0000	0	0.0000	0.0301
CT-based urethra CSF*	5	VB, VR, H95B, GPC1, GPC2	12	88	0.0284	2.088	0.0227	0.0219
CT-based modified GPs urethra CSF*	5	VB, VR, H95B, GPC1, GPC2	-	-	0.0291	2.2213	0.0232	0.0219

Table. C.1 represents the dominant GPs associated with the optimal CT-based target PSF and bladder, rectum, and urethra CSF models. Each of the optimal CT-based target PSF and urethra CSF models includes the same dominant GPs as its corresponding TRUS-based model. However, differences were observed in the dominant GPs obtained for the optimal bladder and rectum CSF models between the TRUS-based and CT-based HDR-BT plans under investigations. We suggested that the differences between the bladder and rectum CSF models associated with the TRUS-based and CT-based HDR-BT plans for prostate cancer may arise from the variations in the contouring of the structures in these two categories of HDR-BT treatments. To confirm this hypothesis, we, first, studied the differences in the dominant GPs caused by the variations in the contouring of the bladder and rectum between the TRUS-based and CT-based HDR-BT. The limitation in the contouring of the volumes in the TRUS-based plans is due to the limited capacity of the crystals used in the TRUS equipment. Moreover, the TRUS tube is placed inside of the rectum during the TRUS-based HDR-BT treatment for prostate cancer. Consequently, only fractions of the bladder and rectum volumes were contoured in the TRUS-based, which is contrary to the CT-based plans. In the CT-based HDR-BT for prostate cancer, the entire bladder and rectum volumes are contoured. Note that despite contouring fractions of the bladder and rectum in the case of the TRUS-based plans, their corresponding volumes required in order to verify

the fulfillment of the ABS recommendations (V75B < 1 cm^3 and V75R < 1 cm^3) were adequately contoured. In the next step to prove our hypothesis, we developed CT-based CSF models in which the extra contoured volumes in comparison with the TRUS-based plans were discarded from the CT-based HDR-BT treatment plans under study. Following the optimization approach discussed before for the TRUS-based and CT-based plans, the MLL values were obtained for the CT-based SF models including the modified GPs. After, the LRTs were carried out between the null and alternative models using the CT-based plans including the modified GPs. Then, the resulting p-values were compared to decide the statistical significance of adding new GPs to an SF model, hence to determine the optimal SF model. As a result of using the CT-based plans including the modified GPs, the optimal rectum CSF model was concluded to possess six dominant GPs. Therefore, the dominant GPs found for the optimal rectum CSF model using the TRUS-based and CT-based HDR-BT plans including the modified GPs are in agreement and consists of six identical dominant GPs.

Table. C.1 summarizes the results obtained by comparing the dosimetric parameters obtained through the TPS with the ones predicted by the developed target PSF and the bladder, rectum, and urethra CSF models using the TRUS-based and CT-based HDR-BT plans. Note that all the plans in the first (TRUS-based) and second (CT-based) cohorts under study were optimized using the TPS. Hence, all the ABS recommendations for the dosimetry indices in HDR-BT treatments for prostate cancer were sufficiently fulfilled by the plans under investigation. Therefore, all these plans were clinically accepted. Nevertheless, the percentage of the plans predicted to be below the target PSF or above the OARs CSFs suggest that the optimization of these HDR-BT treatment plans using the TPS did not necessarily result in the most optimal attainable plan. In other words, the developed target PSF and bladder, rectum, and urethra CSF models predicted that further improvement in the covering of the target and sparing each of the OARs are possible for the HDR-BT plans under study. The target PSF model predicted that the dose V100 received to the CTV can be improved more in the case of the plans situated under the corresponding frontier. Therefore, the target covering can be improved for the 94% of the TRUS-based HDR-BT plans under study, which is relatively more significant than for the CT-based plans (85%). Thus, the dose V100 to the target (CTV) was better covered in the TRUS-based as compared with the CT-based plans. Moreover, the bladder CSF model predicted that minimization of the dose V75 received to the bladder can be improved for the 63% of the TRUS-based HDR-BT plans under examination. In the case of using CT-based plans, bladder sparing can be improved for a higher number of plans (81%) than the TRUS-based plans. Hence, the rectum is an OAR for which the dose V75 is minimized for a more significant volume in the CT-based HDR-BT plans than in TRUS-based plans. Furthermore, the developed rectum CSF models predicted that the improvement in minimization of the dose V75 to the rectum was possible for 71% of the TRUS-based plans, which is comparable to the CT-based (69%) plans under study. Moreover, in the case of the TRUS-based HDR-BT plans, urethra model behaved as a fit, with an equal number (50%) of the plans above and below the model line. As is discussed in the following, a null technical inefficiency was predicted by the urethra CSF model using the TRUS-based HDR-BT plans. Therefore, the TRUS-based urethra model includes no predictive knowledge for the dose D10 to the urethra in the TRUS-based plans

under study. In other words, no further improvement of the minimization of the dose D10 to the urethra was possible for these TRUS-based plans. As opposed to the TRUS-based plans, the urethra CSF model predicted the possibility to minimize the irradiated volume of the urethra for a significant number (88%) of the CT-based HDR-BT plans under examination. As a result, urethra was the OAR that was much better spared using the TRUS-based, as compared to the CT-based plans, HDR-BT treatment plans for prostate cancer.

Although the comparison between the optimal TRUS-based and CT-based target PSF models showed different frontier curves, similar curves were observed for the target PSF models using the TRUS-based and CT-based HDR-BT plans including the modified GPs. Moreover, Table. C.1 shows that the urethra CSF model developed using the CT-based plans including the modified GPs comprise the same dominant GPs as its corresponding models for the TRUS-based and CT-based plans. The frontier curve of the CT-based urethra CSF was shown to be different from the fit obtained for the TRUS-based urethra model. However, identical frontier curves were observed for the urethra CSF model using the CT-based plans and CT-based plans including the modified GPs. Additionally, similar curves were observed associated with the frontiers developed for the rectum CSF models using the TRUS-based and CT-based plans including the modified GPs. Consequently, we showed that the optimal TRUS-based target PSF and the rectum and urethra CSF models were successfully applied to the CT-based HDR-BT treatment plans for prostate cancer.

Table. C.1 also gives the expectation of ε (E(ε)), the standard deviation (SD) of the two error terms; the technical inefficiency (σ_u) and the random noise (σ_v) in Eq.1.17 or Eq.2.9, as well as the ratio of the two error terms in Eq.1.10 for each of the optimal SF models, as discussed in 1.2.2. In the case of the TRUS-based HDR-BT plans under study, as opposed to the null technical inefficiency predicted by the urethra CSF model, the target PSF model predicted a technical inefficiency of $\sigma_u = 0.0219$. Therefore, the possibility to better improve the target covering is more significant than the urethra sparing using the TRUS-based HDR-BT plans. The urethra model predicted no variation associated with the planners' experience and judgment in the minimization of the dose D10 to the urethra using the TRUS-based HDR-BT plans. In effect, great effort was made to spare the most possible of the urethra volume in the TRUS-based HDR-BT treatment plans under study. However, the largest technical inefficiency between the target covering and OARs sparing using the TRUS-based HDR-BT plans was obtained based on the rectum CSF model for the minimization of the dose V75 to the rectum ($\sigma_u = 0.208$). A higher technical inefficiency specifies a more significant variation in the planners' experience and judgment for the minimization of the dose V75 to the rectum in the TRUS-based plans. On a lesser extent than the rectum sparing, further improvement in the minimization of the dose V75 to the bladder was predicted by the bladder CSF model using TRUS-based plans. In the case of the CT-based HDR-BT plans under examination, the best trade-off was between the target covering ($\sigma_u = 0.017$) and the urethra sparing ($\sigma_u = 0.028$). The highest technical inefficiency ($\sigma_u = 0.431$), and expectation value ($E(\varepsilon) = 0.344$), were obtained associated with the minimization of the dose V75 to the bladder using the CT-based HDR-BT plans. Consequently, the highest variability in

the planner's experience and judgment using the CT-based HDR-BT plans was related to the bladder sparing. The lowest technical inefficiency was predicted for the minimization of the dose V75 to the rectum ($\sigma_u = 0.0004$). As a result, rectum was the organ for which the minimization of the irradiated volume was better performed as compared with the other OARs in the CT-based HDR-BT treatment plans.

The developed bladder CSF model predicted a more significant variability in the quality of the CT-based HDR-BT plans in comparison with the TRUS-based plans under study. As compared with the TRUS-based plans ($E(\varepsilon) = 0.083$, SD=0.90), a higher expectation value and the corresponding SD was obtained based on the bladder CSF model ($E(\varepsilon) = 0.344$, SD=2.68) using the CT-based plans. In other words, a more extreme variation in the planners' experience and judgment in sparing the bladder was associated with the CT-based than the TRUS-based HDR-BT plans. Furthermore, as opposed to the TRUS-based plans, a relatively negligible technical inefficiency obtained for the minimization of the dose V75 to the rectum in the CT-based HDR-BT plans. Thus, variations in the quality of the TRUS-based HDR-BT plans associated with the optimization of the dose V75 to the rectum due to planners' experience and judgment are more critical as compared with the CT-based plans. Note that the TRUS tube is placed in the rectum during the HDR-BT delivery, which affects the shape of the rectum wall, prostate and the surrounding anatomy hence changes the distances between the prostate and rectum.

In the case of the urethra CSF model, contrarily to the technical inefficiency of $\sigma_u = 0.0284$ for the CT-based HDR-BT plans, a null technical inefficiency was obtained using the TRUS-based plans. Therefore, more variations in the Planners' experience and judgment in minimization of the dose D10 to the urethra was associated with the CT-based than TRUS-based HDR-BT plans. Note that in the case of the CT-based HDR-BT treatment, changes in the patient position (i.e., lowering the legs) to acquire CT images can reduce the precision in the needle positioning.

Additionally, according to the expectation and SD of the ε obtained for different TRUS-based and CT-based SF models, the target covering in the TRUS-based plans ($E(\varepsilon) = -0.0175$, SD=0.014) was comparable with the target covering in the CT-based plans ($E(\varepsilon) = -0.0139$, SD=0.012). Nevertheless, as compared with the CT-based plans ($E(\varepsilon) = 0.122$, SD=1.16), a better average OAR sparing was predicted in the case of the TRUS-based HDR-BT plans under study ($E(\varepsilon) = 0.082$, SD=0.521). Therefore, a more considerable variation in planner's experience and judgment in the average OARs sparing was observed in the CT-based than in the TRUS-based HDR-BT plans. Thus, the developed bladder, rectum, and urethra CSF models predicted a more significant improvement in the minimization of the dose received by the OARs in the CT-based plans as compared with the TRUS-based plans.

In conclusion, we successfully developed the target PSF and the bladder, rectum, and urethra CSF models for the TRUS-based HDR-BT treatment for prostate cancer. Additionally, we confirmed that these PSF and CSF models succeed to perform well in another category of the HDR-BT treatment

for prostate cancer (i.e., CT-based). Hence, we showed that the target PSF and OARs CSF models developed for the TRUS-based category of the prostate HDR-BT are universal. Finally, the target PSF and the bladder, rectum, and urethra CSF models developed for the HDR-BT treatment for prostate cancer can be included in a QC tool. Using this QC tool can provide the planners with the knowledge of any possible further improvement of the dosimetric parameter such as V100 of the target, V75 of the bladder, V75 of the rectum. In other words, planners can generate optimized plans to obtain the possible patient-specific dosimetry for each patient according to the patient-specific geometrical information. Thus, the QC tool can be used to minimize the impact of the subjective judgment on the best trade-off between target covering and OARs sparing due to the variability in the planners' experience and judgment on the quality of a plan in HDR-BT treatment for prostate cancer. Therefore, the quality of the HDR-BT treatment plans for prostate cancer can be improved. Furthermore, the developed SF models can predict the possible dosimetric indices for each patient based on the patient-specific geometrical knowledge. Thus, the planners can continue the optimization process if the geometry of the patient allows further improvement in the target covering and OARs sparing. In the case of a patient for whom no further improvement in the dosimetry is possible due to the patient's geometry, the planner can stop the inefficient optimization at the right time. As a result, planners can save more planning time.

Furthermore, one can exploit the developed SF models for the target PSF and bladder, rectum, and urethra CSF models in order to generate the corresponding DVHs. In order to construct these DVHs, the SF models can be utilized to predict the dose V100 to the target, V75 to the bladder and rectum, and D10 to the urethra based on the geometric knowledge of each patient in an HDR-BT treatment for prostate cancer. Then, DVHs are produced by relating the predicted dose to the tissue volumes. The generated DVHs provide planners the possibility to evaluate an HDR-BT treatment plan for prostate cancer before the planning process.

The outcome of this research project will be published in a main article. The article is dedicated to the development of a geometry-based target and OARs dose prediction tool, built by bringing the concept of SF analysis into play. The developed QC tool can be employed in the HDR-BT planning for prostate cancer treatment to increase the target coverage and OARs sparing, hence to improve the quality of these treatments. The PSF model will be proposed for the target covering, as well as one CSF model for each of the OARs: the bladder, rectum, and urethra. In each of these PSF and CSF models, the dominant GPs and their corresponding weights will be provided. We will discuss that these target PSF and OARs CSF models developed based on TRUS-based plans are applicable for another category of HDR-BT treatment for prostate cancer, CT-based HDR-BT. Furthermore, a multi-dimensional plot will be considered comprising the optimal PSF for the target and the CSF for the bladder, rectum, and urethra. These optimal SFs developed based on the specific-anatomical knowledge of preceding HDR-BT prostate patients can be used to tackle the multi-objective problems of new patients. Each dimension of the multi-dimensional plot will be associated with different objectives. These objectives are either increasing the dose to the target or reducing the dose received by each

of the OARs. Therefore, planners using this multi-dimensional plot could be able to predict, before the planning, the possible balance between target coverage and OARs sparing for a new prostate patient. Consequently, planners can avoid wasting time and effort attempting to achieve dose objectives in cases that the patients' geometries do not allow further improvements. Moreover, in the case of new planners with fewer competencies, as compared to the well-experienced planners, the developed QC tool can be used as a guide to teach them the details of the planning procedure for the HDR-BT treatment for prostate cancer.

As a final thought, I feel privileged to have had the chance to touch on clinical research. The brilliant concept of SF, initially used in economics, was successfully brought into play to develop SF models to improve the quality of the HDR-BT treatment for prostate cancer.

Future works

The developed PSF and CSF models can be used to predict the dose to the target and OARs, respectively. The subsequent step in researching the current topic could be the implementation of these developed SF models in the clinical environment. For this, a QC tool comprising the developed target PSF and bladder, rectum, and urethra CSF models need to be designed. Then, scripts including these PSF and CSF models can be implemented into clinical workflow. In this way, the clinicians will be allowed to ascertain what should be plausible for new prostate patients who are going to be treated using HDR-BT. Following the clinical implementation of these models, for instance after four months, a thorough survey can be performed. This survey will show the impact of these models on planners' work, as well as on the quality of plans, and on saving the time. Furthermore, the QC tool can be used to compare HDR-BT plans produced by different clinics quantitatively. Therefore, this QC tool can be used to benchmark the procedures and capabilities of different institutions.

Appendix A

Appendices

A.1 Different Representations of the SCCs

Fig. A.1 exhibits the V100 DP and all the 18 GPs of the CTV. Furthermore, their associated density plots, as well as histograms, are indicated along the diagonal. The SCCs designating the associations between all the possible pairs among the 18 GPs and DP V100 are shown in the upper triangle of Fig. A.1. The scatter plots between every two parameters along with the related LOESS (local regression) smoothed fit are represented in the lower triangle of Fig. A.1. Since a nonlinear trend line that expresses the movement in the data is required, LOESS regression is used to fit a smooth curve between two or more points in the data series. LOESS is a nonparametric regression method, which combines the simplicity of linear least squares regression with the flexibility of nonlinear regression, and fits several multiple regressions in the local neighborhood. A LOESS regression divides the data under study into localized subsets and fits regression on each of those subsets. Then, by using the LOESS regression results, the data series can be fitted by a LOESS curve where each point is acquired by weighing the individual regressions (190). Note that the *pairs.panels* function from *psych* package in RStudio was used here.

The *corrplot* provides a graphical analysis package to look at the correlation coefficient of a number of variables at once package in R. In Fig. A.2, the degree of association between every pair of parameters is visualized with the ellipse and the pie methods. In the upper triangle of Fig. A.2, the SCC between every set of parameters is represented by a pie. The intensity of the color and the arc length (and hence its central angle and area) of each slice of pie indicate the size of the correlation. So, a relatively small slice of light blue pie denotes a weak positive correlation between two parameters, whereas a red slice indicates a negative correlation. In the lower triangle of Fig. A.2, the two parameters are represented with ellipses. The tendency of an ellipse to be oriented either from lower left to upper right or from the bottom right to top left, are respectively indicatives of a positive and a negative correlation. Also, the width (minor axis) of an ellipse is a demonstration of the strength of a correlation. The smaller the minor axis of an ellipse, the stronger the correlation. Additionally, the intensity of the blue or red

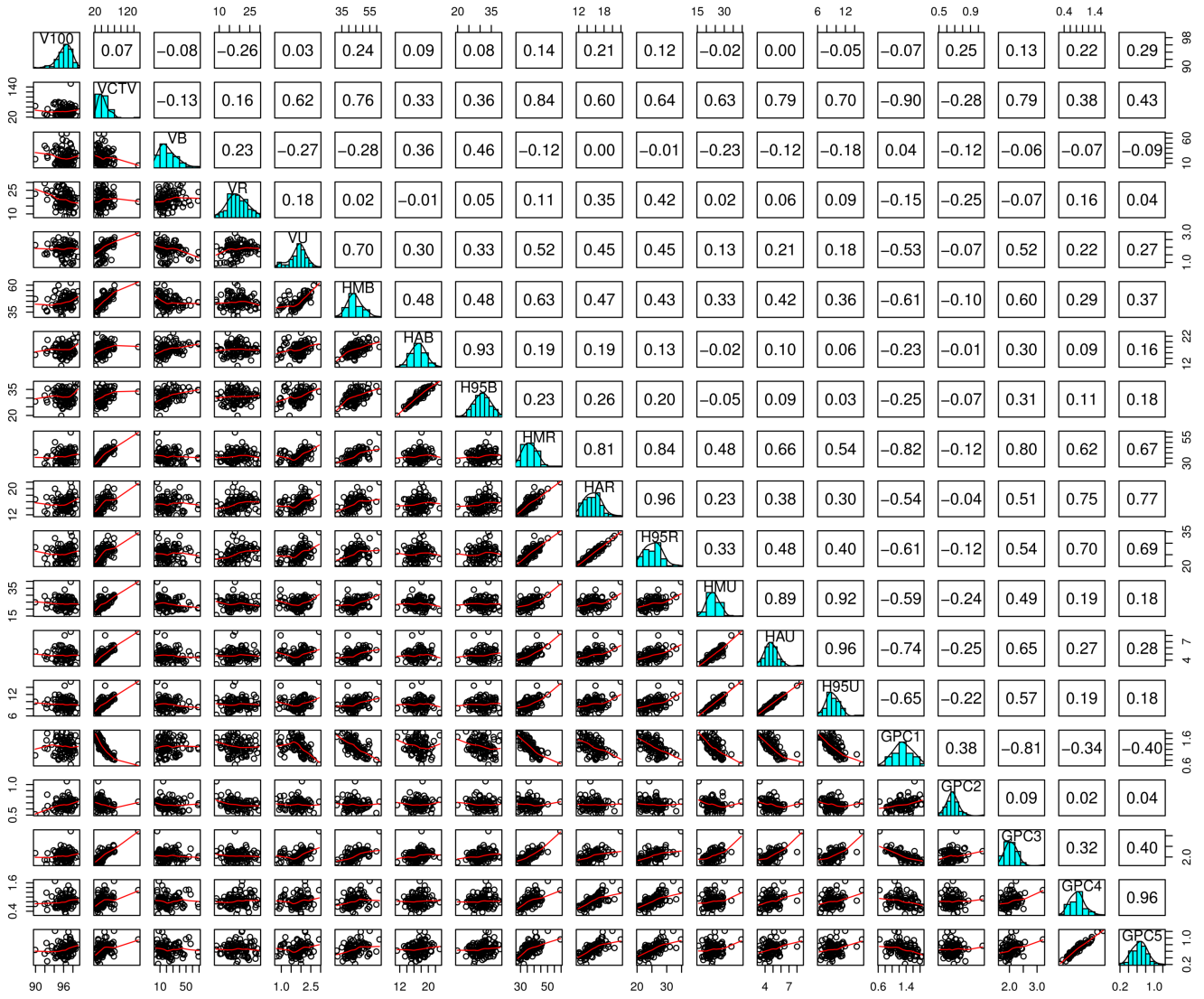

Figure A.1 – SCCs between all the pair parameters of the target PSF.

color of an ellipse shows the strength of a respectively positive and negative correlation.

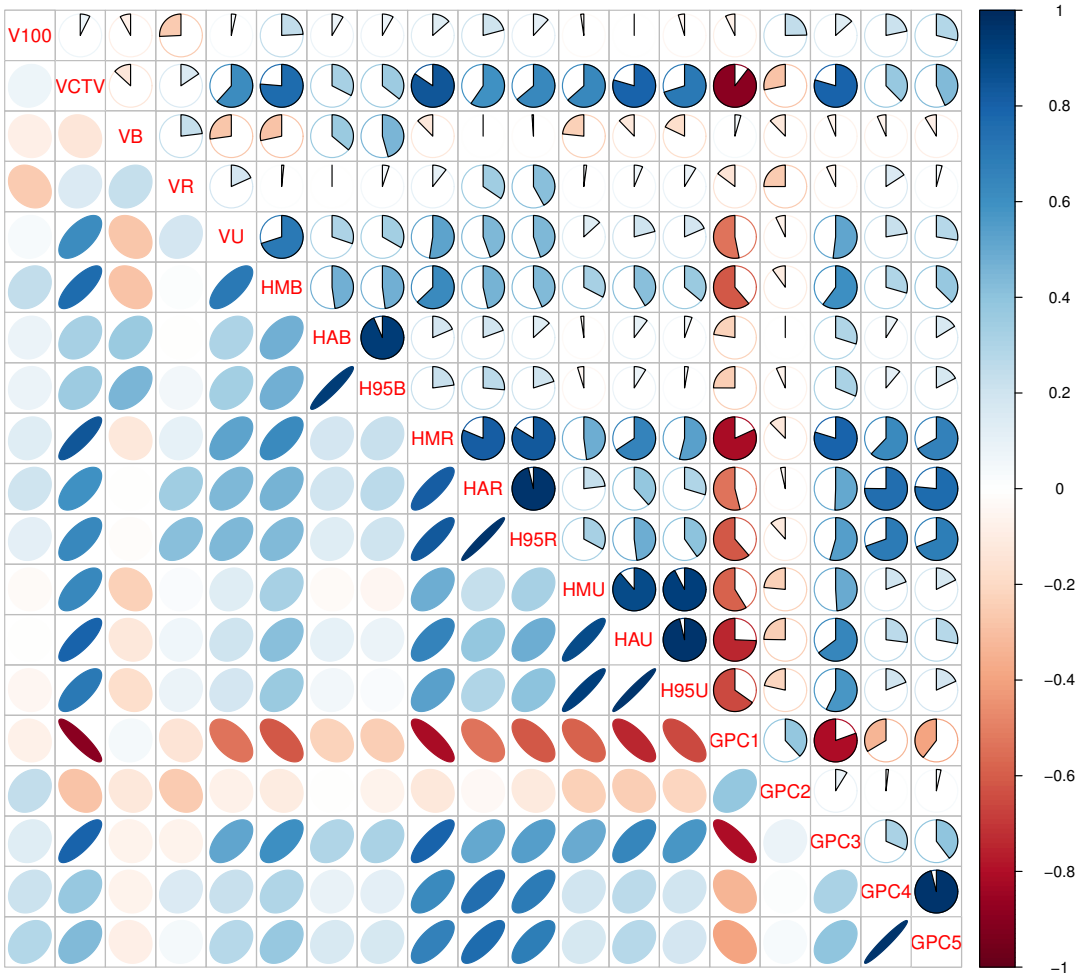

Figure A.2 – Two different visualizations of the relationships between pair parameters in a CTV PSF model obtained by the SCC method. The strength and direction of the correlation are illustrated by color code, dark blue depicting a strongly positive correlation and red being strongly negative. The arc length of a pie and the minor axis size of an ellipse show the strength of a correlation. The bigger the arc length of a pie (or equivalently the smaller the width of an ellipse), the stronger the correlation.

The same method, as discussed above, was applied to obtain the density plots as well as the histograms for the DP V75 and each of the 18 GPs of the bladder, which are shown in the diagonal of Fig. A.3. The values for the SCCs between all pairs of parameters of the bladder are indicated above the diagonal, and the scatter plots and their associated LOESS smoothed fits are exhibited below the diagonal. Furthermore, the Spearman correlation ellipses and pies associated to the bladder are shown in Fig. A.4.

In the case of the rectum, Fig. A.5 exhibits all the pairwise combinations of the DP V75 and the entire

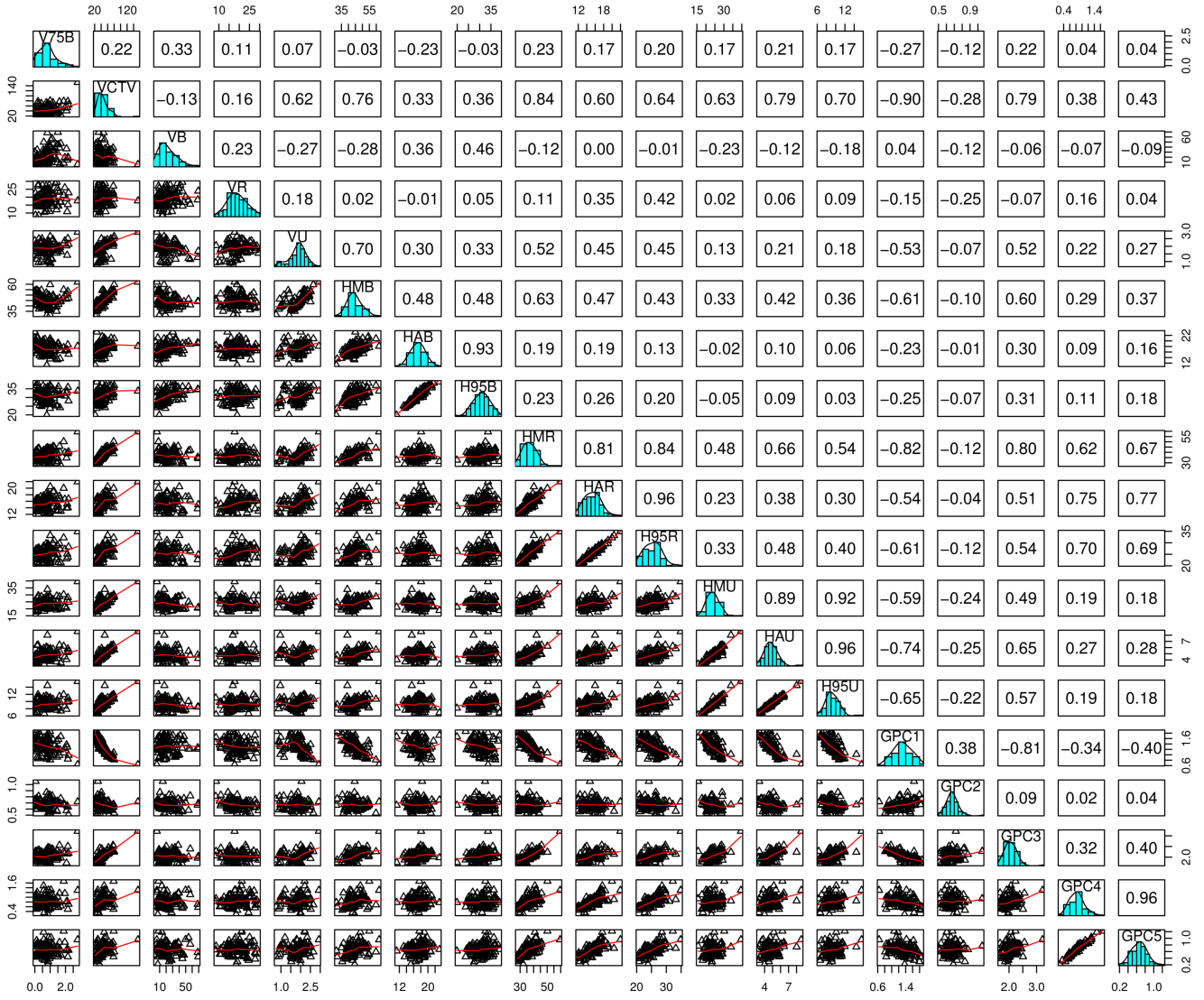

Figure A.3 – SCCs between all the pair parameters of the bladder CSF.

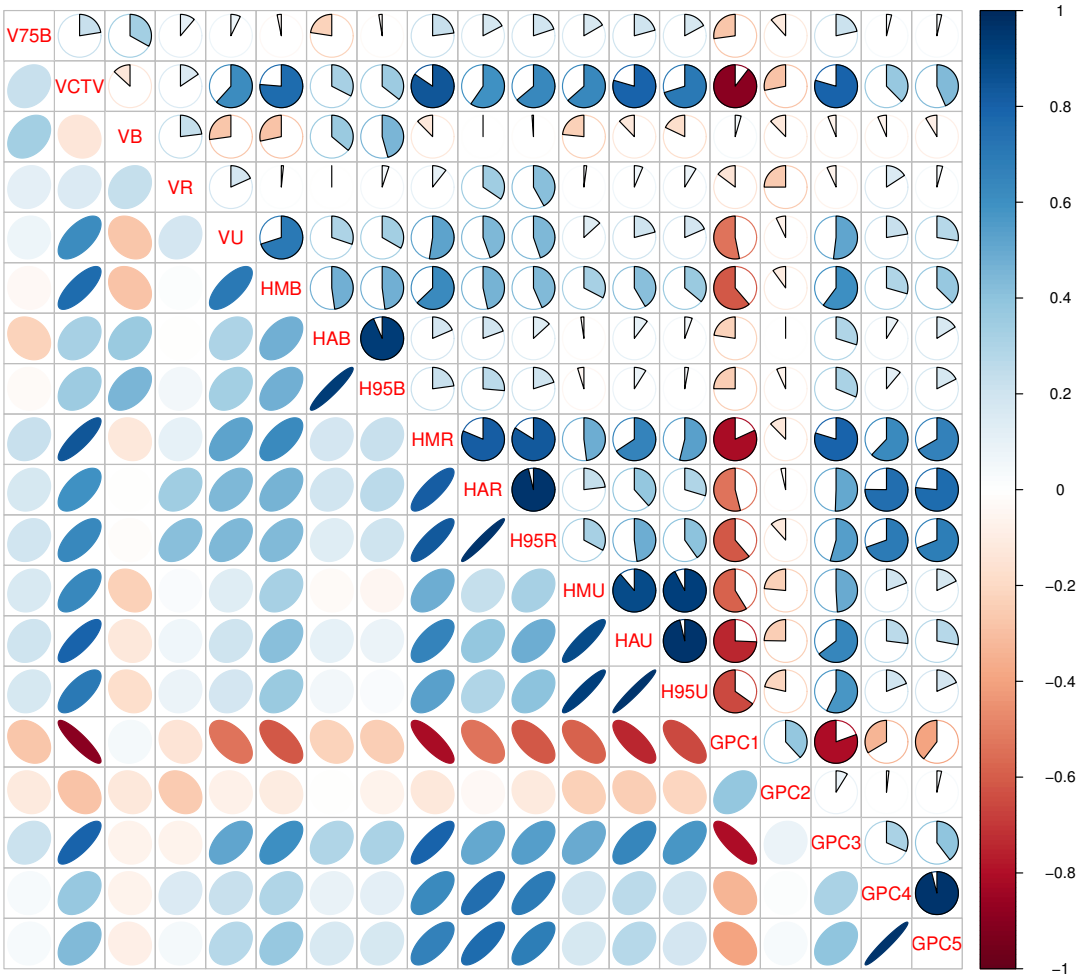

Figure A.4 – Graphical display of the correlation pies and ellipse associated to the SCCs for the bladder.

18 GPs in scatter plots. Additionally, the histograms were shown on the diagonal, the SCCs above the diagonal, and scatter plots and the corresponding LOESS regression fits below the diagonal.

Fig. A.6 represents the ellipses and pies corresponding to the SCCs between all the parameter pairs of the bladder.

In the case of the urethra, Fig. A.7 represents a scatter plot of D_{10} DP for the urethra and the total of the 18 GPs. The scatter plots are exhibited below the diagonal, histograms on the diagonal, and the SCCs above the diagonal. Furthermore, Fig. A.8 exhibits the correlation pies and ellipse related to the SCCs for the urethra.

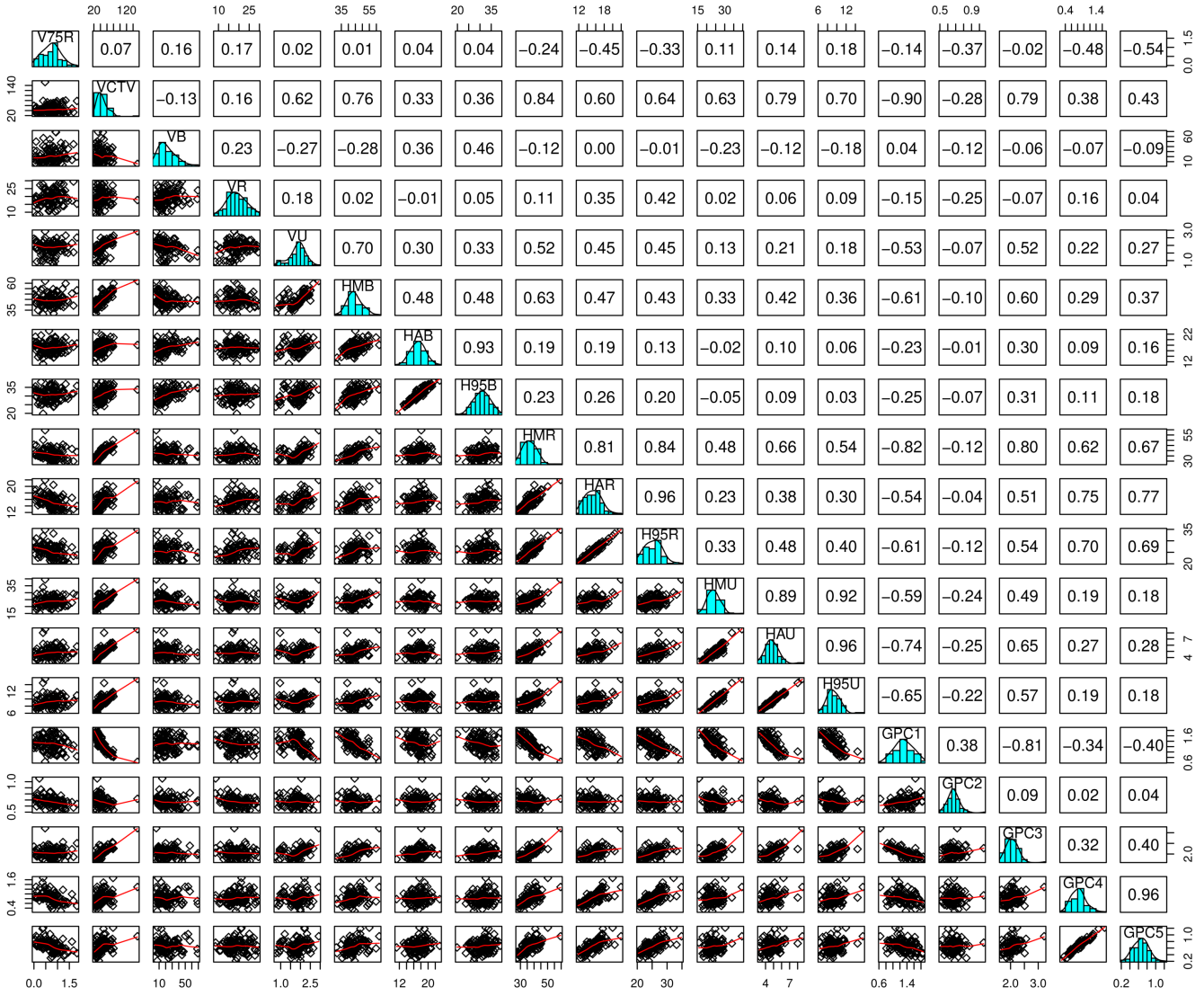

Figure A.5 – SCCs between all the pair parameters of the rectum CSF.

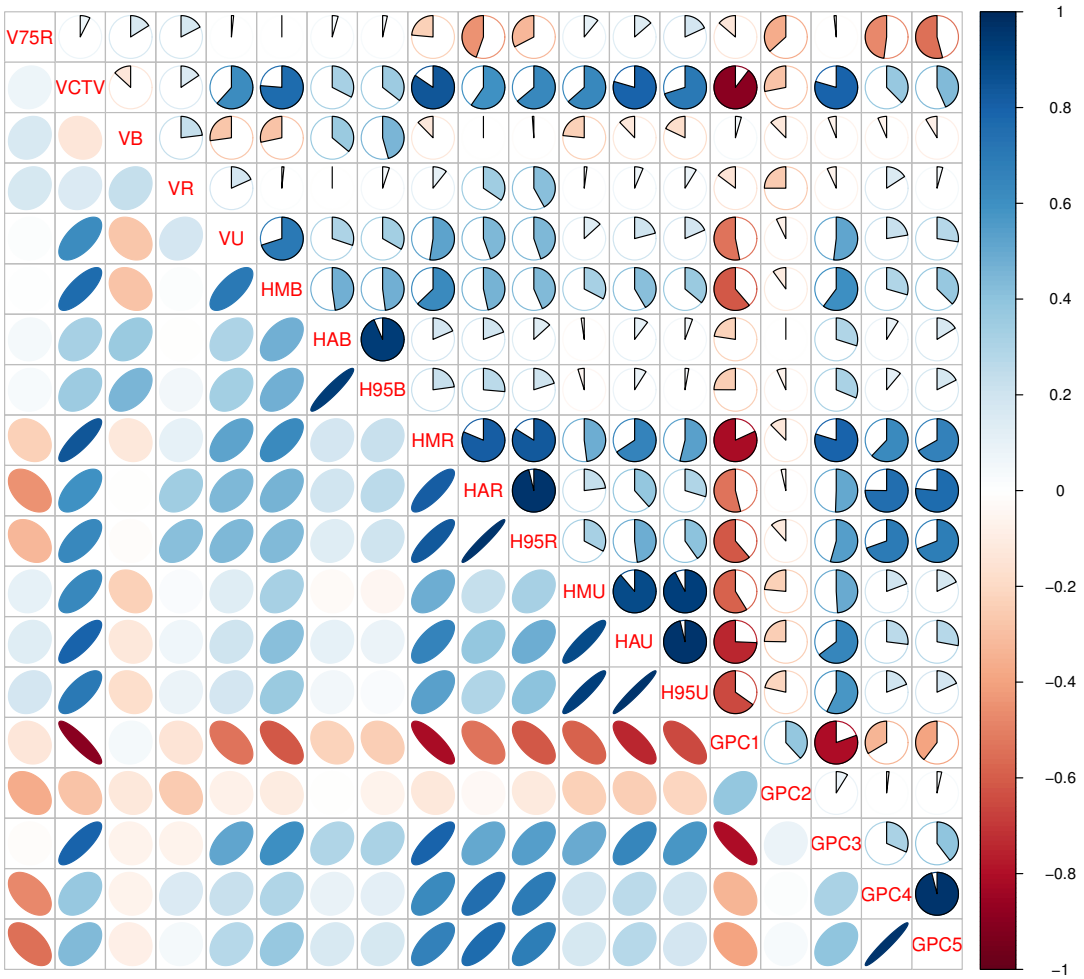

Figure A.6 – Graphical display of the correlation pies and ellipse corresponding to the SCCs for the rectum.

A.2 Degradation of a Plan with respect to an Optimal SF

A.2.1 TRUS-based Plans

As discussed in Eq.1.10, the marginal density function, $f(\varepsilon)$, of the CTV volume coverage is shown in Fig. A.9(a). ε is the difference between the values obtained by the IPSA optimization and the ones by the corresponding SF model. As we expected, according to our review in 1.2, a negatively skewed function is obtained for the PSF. Furthermore, in Fig. A.10(a), the distribution of the differences between the observations evaluated by IPSA and the values predicted by the CTV PSF model (ε) over all the plans considered in our data cohort are illustrated in the form of a histogram. Furthermore, in Fig. A.10(a), the distribution of the differences between the observations evaluated by IPSA and the values predicted by the CTV SF model over all the plans considered in our data cohort are illustrated

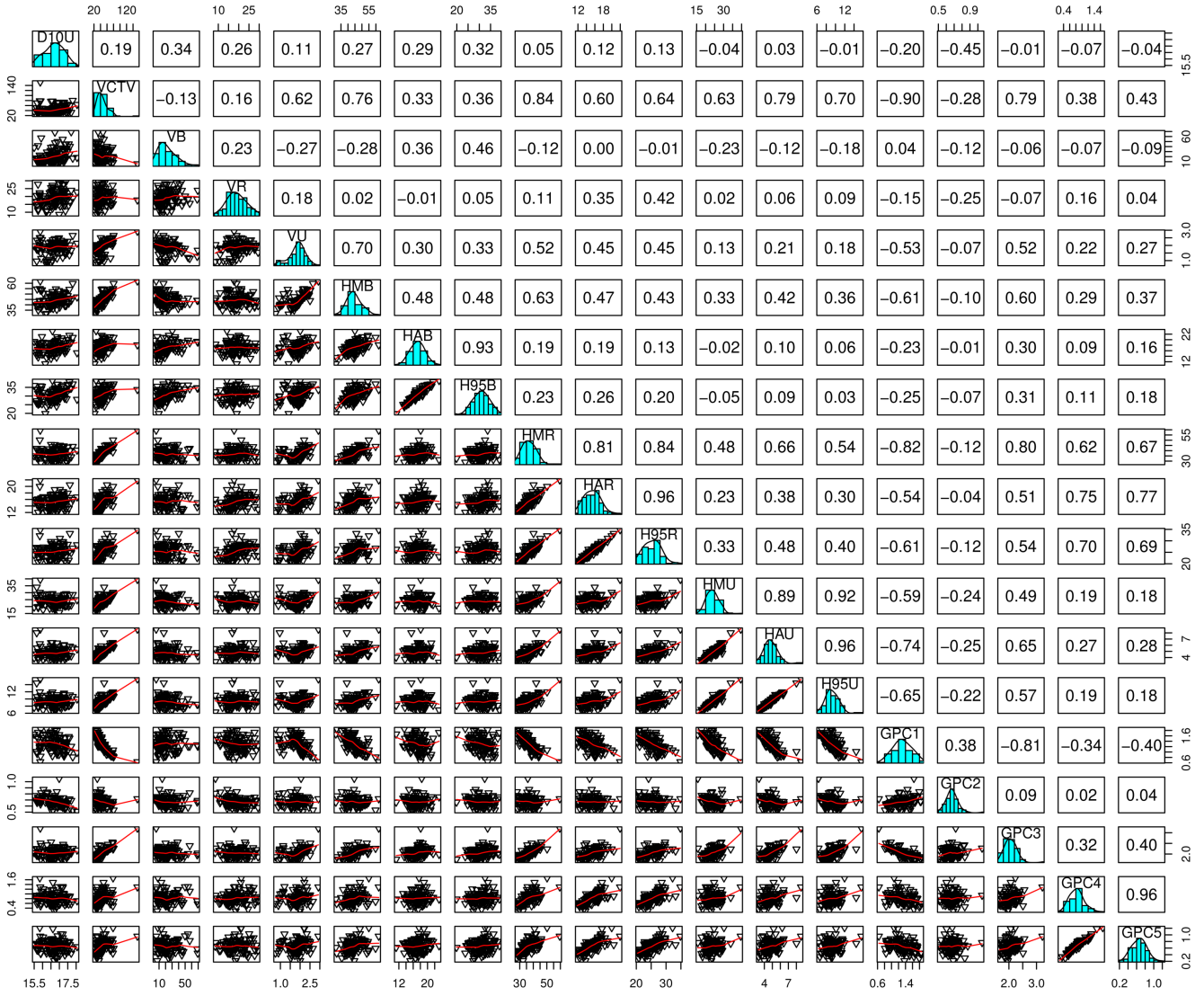

Figure A.7 – SCCs between all the pair parameters of the urethra CSF.

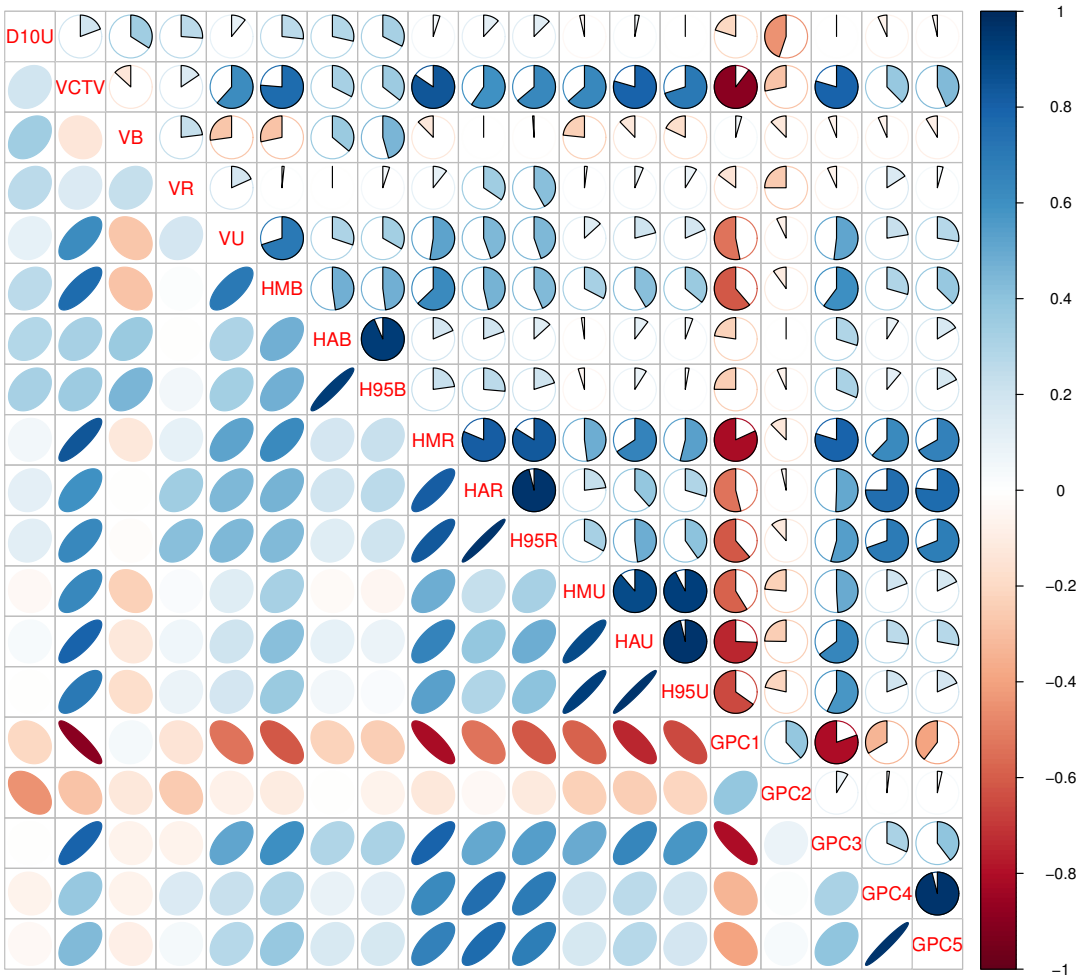

Figure A.8 – Graphical display of the correlation pies and ellipse related to the SCCs for the urethra.

in the form of a boxplot and a histogram, respectively.

Fig. A.9(b) illustrates a positively skewed marginal density function, $f(\varepsilon)$, for the bladder volume coverage. Additionally, the differences between the IPSA evaluated values and the dose values obtained using the bladder CSF model (ε) are demonstrated by a histogram in Fig. A.10(b). Furthermore, the differences between the IPSA evaluated values and the ones in the bladder CSF model were demonstrated by Fig. A.9(c) shows a positively skewed marginal density function for the rectum volume coverage.

Moreover, Fig. A.10(c) exhibits the histograms of the evaluated differences between the IPSA computed optimized values and the values predicted by the rectum CSF model (ε).

Fig. A.9(d) shows the resulted marginal density function for the urethra model developed for TRUS-based HDR-BT plans. Due to having an equal number of the plans above and below the urethra model line, the density function is symmetric around zero. Furthermore, Fig. A.10(d) shows the histogram

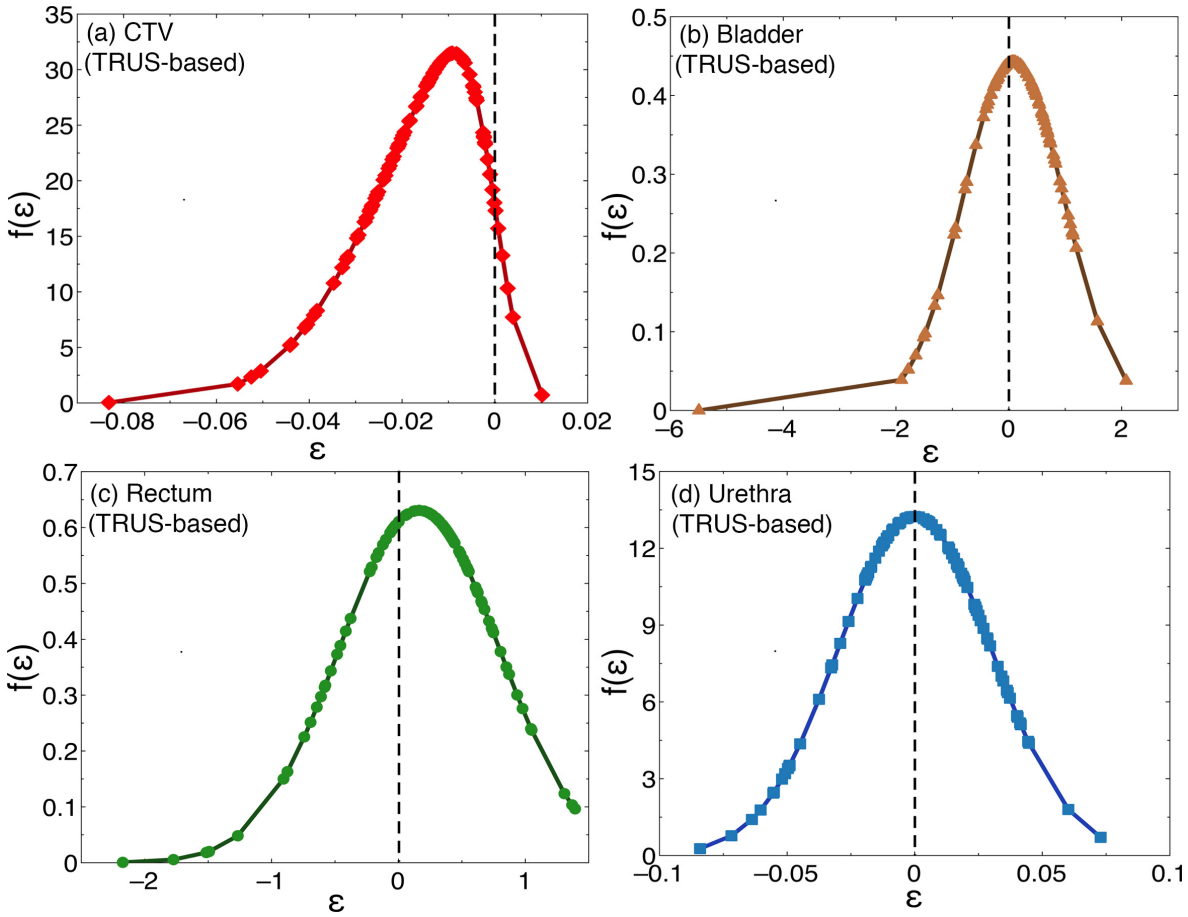

Figure A.9 – Marginal density function, $f(\varepsilon)$, of the CTV (a), bladder (b), rectum (c), and urethra (d) volume coverage for the TRUS-based plans. ε is the difference between the values optimized by IPSA and by the corresponding SF model for the TRUS-based imaging HDR-BT.

associated with the differences between the values obtained by IPSA and the urethra model.

A.2.2 CT-based Plans

Fig. A.11(a) shows the marginal density function, $f(\varepsilon)$, of the CTV volume coverage is illustrated, which is negatively skewed. Also, the histogram represented in Fig. A.12(a) illustrates the ε for the target CT-based PSF.

Fig. A.11(d) shows a positively skewed marginal density function related to the urethra volume coverage. Additionally, in Fig. A.12(d), ε is exhibited for the urethra CT-based CSF model.

Figs. A.11 (b) and (c) show the marginal density functions associated with the bladder and rectum volumes coverage respectively. Moreover, ε for the bladder and rectum CSFs are shown as the histograms in Figs. A.12 (b) and (c) respectively.

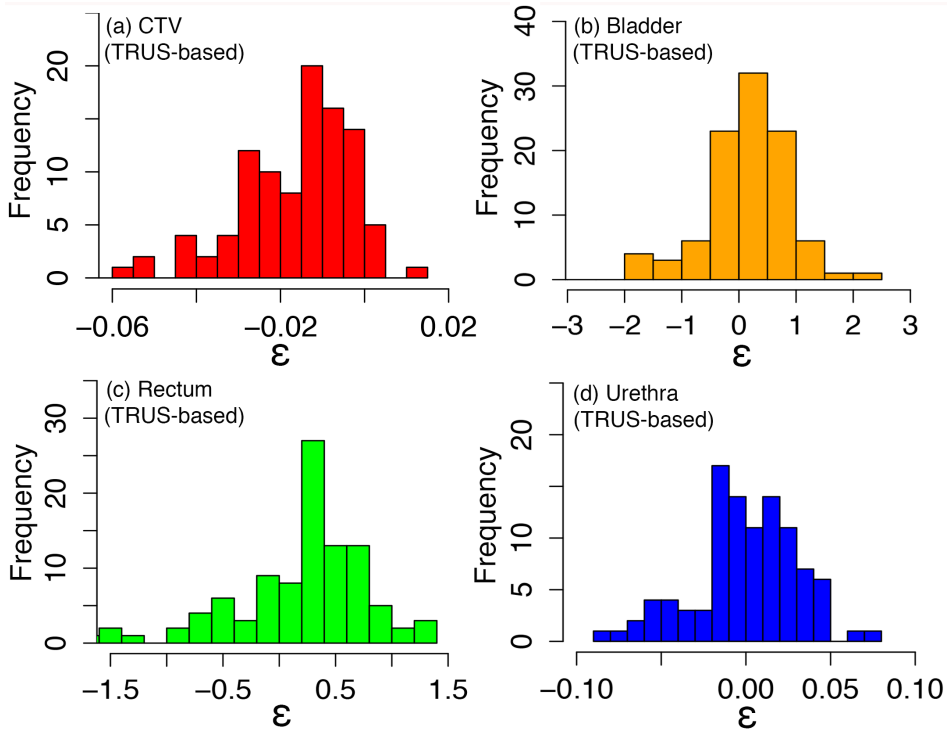

Figure A.10 – Histograms representing the difference between the IPSA optimized values and the values optimized by SF (ε) for the CTV (a), bladder (b), rectum (c), and urethra (d).

A.3 R built-in Functions in Rstudio

GenSA Function

The global minimum of a complex non-linear objective function including an extremely large number of optima can be obtained using the Generalized Simulated Annealing (*GenSA*) function. The application of the R built-in function corresponding to the *GenSA* function in Rstudio is given as

GenSA(*par*, *fn*, *lower*, *upper*, *control=list()*, ...),

where the first argument, *par*, is the vector of the initial values for the components to be optimized. In case the default value of this argument (i.e., NULL) is selected, hence the default values will be generated automatically. The next argument in the GenSA function, *fn*, is a function to be minimized. Note that the first argument of the *fn* function is the vector of parameters over which minimization is to carried out. The two following arguments in the GenSA function, *lower* and *upper*, are vectors with length of par. They are used to determine, respectively, the Lower and Upper bounds for components. Furthermore, the *control=list()* argument is used to control the behavior of the GenSA algorithm.

control=list() is a list including different arguments such as *temperature*, *nb.stop.improvement*, *maxit*, *max.time*, *max.call*, *simple.function*, and *verbose*.

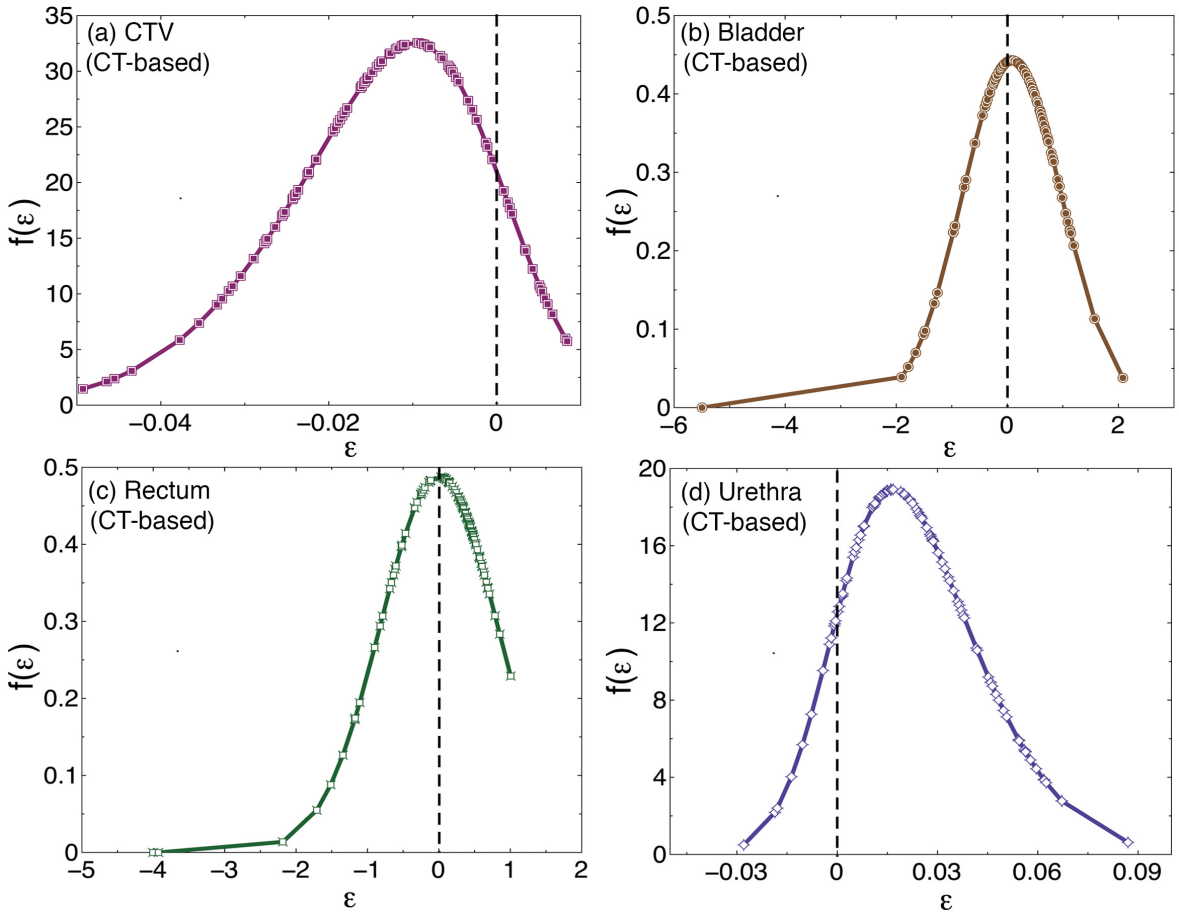

Figure A.11 – The marginal density function, $f(\varepsilon)$, of the CTV (a), bladder (b), rectum (c), and urethra (d) volume coverage for CT-based plans. ε is the difference between the values optimized by IPSA and by the corresponding SF model for the CT-based HDR-BT.

By providing a numeric value for *temperature*, the initial value for temperature in the GenSA algorithm can be chosen. Moreover, the *nb.stop.improvement* argument can be applied to stop the program when no improvement is observed in its corresponding steps. Also, the maximum number of iterations of the algorithm can be appointed using an integer value for *maxit*. The running time is selected in seconds employing *max.time*. Moreover, an integer value for *max.call* determines the maximum number of call of the objective function. Default is set to 1e7, however, in this research project, *max.call* was increased to 1e8. Additionally, in the course of our research project, the default (i.e., FALSE) was chosen for *simple.function* indicating that the objective function is complicated with many local minima. Besides, TRUE was selected for *verbose*, which enables messages from the algorithm to be represented.

MLL Method

As discussed in 2.4, Eq.2.9 yields the LL of a production function. This equation includes the built-in

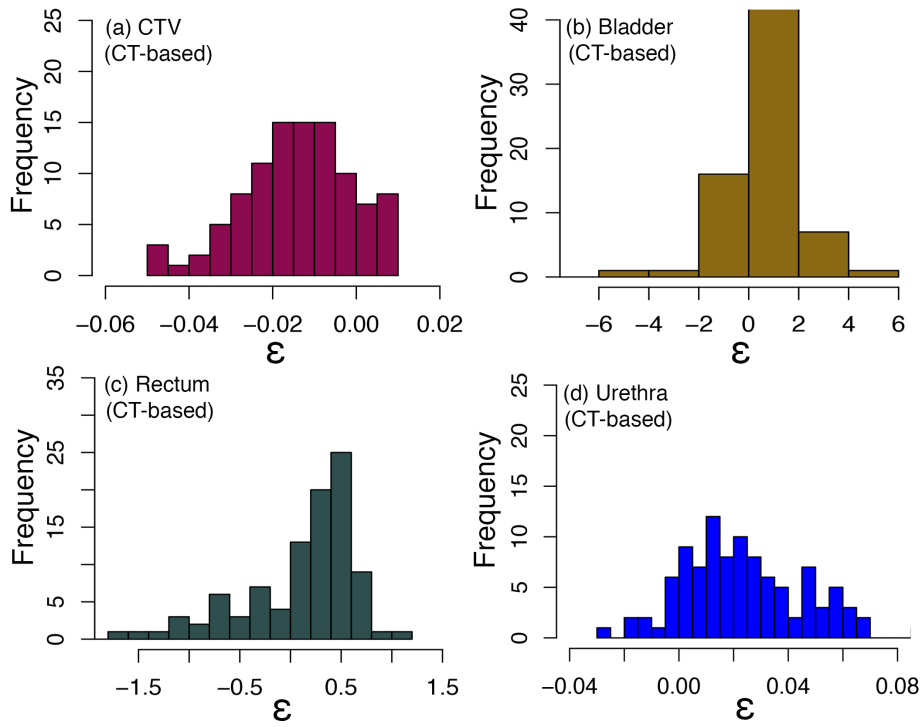

Figure A.12 – Histograms representing the difference between the IPSA optimized values and the values optimized by CTV PSF (a), bladder (b), rectum (c), and urethra (d) CSF models in the case of CT-based plans.

functions in Rstudio such as *dnorm* and *pnorm*. The density and distribution function for the normal distribution with mean given by *mean* and standard deviation given by *sd* are defined using *dnorm* and *pnorm*, respectively. These two R built-in functions are written as

dnorm(x, *mean* = 0, *sd* = 1, *log* = FALSE),

pnorm(q, *mean* = 0, *sd* = 1, *lower.tail* = TRUE, *log.p* = FALSE),

where x, q are the vector of quantiles. Moreover, *mean*=0, *sd*=1 were selected for *dnorm* and *pnorm*. If TRUE is selected for *log*, *log.p*, then probabilities p are given as log(p). Additionally, if the default (i.e., TRUE) is selected for the *lower.tail*, probabilities are P[X $\leqslant$ x], otherwise P[X $>$ x]. As discussed in 2.4, Eq.2.8 provides the PDF for the normal distribution. In Eq.2.8, *dnorm* function yields the value of the PDF for the normal distribution given parameters for x, μ, and σ. Therefore, *dnorm* function gives the density. Moreover, *pnorm* function gives the distribution function. *pnorm* function is the integral from $-\infty$ to q of the PDF of the normal distribution. In order to deal with the integral from q to ∞, the argument *lower.tail* of the *pnorm* function must be set to FALSE. Then, $1 - pnorm(q, lower.tail = FALSE)$ can be replaced by its equivalent, *pnorm(q)* (185). So, $pnorm(-\varepsilon\lambda/\sigma, 0, 1)$ was used in Eq.2.9 as an alternative to $1 - pnorm(-\varepsilon\lambda/\sigma, 0, 1)$. Note that GenSA algorithm provides the global minimum. Consequently, in order to maximize the LL function of a given SF model, a minus one (-1) needs to be inserted into the summation in Eq.2.9. As a result,

the MLL value is evaluated for the target PSF model. Please note that in order to evaluate the MLL value for each of the bladder, rectum, and urethra CSF models, the last term in Eq.2.9 was substituted with $pnorm(\varepsilon\lambda/\sigma, 0, 1)$.

LRT

Likelihood Ratio Test (LRT) and its corresponding p-value were used to verify if adding new GPs to a given SF model is statistically significant. Hence, LRT gives the optimal SF model between two competing SF models: the null and alternative models (154). The model with less number of the GPs is considered as the null model, and the one with more GPs is the alternative model. If the obtained p-value is less than the significance level of 0.05, the alternative model is chosen, and the null model is rejected. However, in case the corresponding p-value is equal to or larger than the significance level of 0.05, the null model is selected, and the alternative model is rejected.

In order to specify the optimal SF model for each of the target PSF as well as the bladder, rectum, and urethra CSF models, one must carry out LRTs and the corresponding p-values between all the competing null and alternative models. Thus, the test statistic given in Eq.1.18 is used. As discussed in 1.2.3, when the size of a sample increase towards infinity, the test statistic for a nested model will, asymptotically, take the form of a chi-squared distribution with df degrees of freedom. Note that the assumption that the null model is true is taken into account (155). df is the difference in the number of GPs between the null and alternative models considered in a given LRT. The *pchisq* function in R is utilized to carry out LRTs and to evaluate the corresponding p-values. In R, the distribution function for the chi-squared (χ^2) distribution with df degrees of freedom is given by *pchisq*(*q*, *df*, *lower.tail* = FALSE).

SCC Method

In order to evaluate the SCC and the corresponding p-value, R built-in functions in Rstudio, such as *corr*$*estimate* and *corr*$*p.value*, respectively, can be applied. Additionally, the SCC and the corresponding p-value can be obtained using

cor.test(*x*, *y*, *method* = "spearman", ...),

where *x* and *y* are numeric vectors of data values. In the case of this research project, *x* and *x* are the GP or DP of interest. The *method* is chosen as "spearman", hence Spearman correlation statistic is used as the method to estimate a rank-based measure of association.

Additionally, the correlation of x and y vectors can be computed using *cor* function. In the case that x and y are matrices, *cor* function provides the correlations between the columns of x and the columns of y are computed. The *cor* function in Rstudio is written as

cor(*x*, *y* = NULL, *method* = "spearman"),

Note that one has to either give a matrix or data frame given for x, or provide both x and y. The *method* was selected as "spearman" indicating the SCC statistics applied to compute the correlation coefficients. For more description regarding the R built-in functions for SCC, the interested reader is referred to the reference (186).

Brute-Force Search and Parallel Computation

R code needs to be executed several times in order to perform the brute-force test in R. Therefore, the *foreach* package was used, which offers a looping construct to carry out the R code repeatedly. Note that *foreach* is similar to the standard *for* loop, however *foreach* does not need the body of the *for* loop to become a function. Also, as opposed to the *for* loop, the return of a *foreach* is a list of values. That is an advantage of *foreach* when dealing with a loop that is meant to produce a data structure such as a list, a vector, or a matrix. Another advantage of using *foreach* is the parallel execution, as it provides us with the possibility of performing repeated R operations on many cores of a computer or many nodes of a cluster, and hence bringing down the overall runtime. Consequently, three steps of parallel computing can be performed by applying the *foreach* package: the complex problem is split into pieces by the iterators, the pieces are executed in parallel by the $\%dopar\%$ function, and finally the results are collected back together by the specified *.combine* (191).

Before carrying out a parallel computation, *doParallel* package is registered, which is a "parallel backend" for the *foreach* package. *doParallel* employs R's built-in a parallel package to perform *foreach* in parallel. Note that to execute an R code in parallel, the *foreach* has to be used together with the *doParallel* package, or else *foreach* will do the operations sequentially. Furthermore, to register *doParallel* to use with *foreach*, the *registerDoParallel* function is required. Here, an argument can be called to define a cluster, which is generated by the *makeCluster* function. Also, the number of cores to be used by the *doParallel* to execute tasks can be defined as "core" argument (192).

A.4 R codes

A.4.1 MLL

```
# Function

minimiser <- function(par){
  sigma_u = par[1]
  sigma_v = par[2]
  a0 = par[3]
  a1 = par[4]
  sigma = sqrt((sigma_u^2) + (sigma_v^2))
  lambda = sigma_u/sigma_v
  front_g = par[3] + par[4]*log(z1*par[5]+z2*par[6]+z3*par[7]+z4*par[8]+z5*par[9]+z6*par[10]+z7*par[11]+z8*par[12]+
                                z9*par[13]+z10*par[14]+z11*par[15]+z12*par[16]+z13*par[17]+z14*par[18]+z15*par[19]+
                                z16*par[20]+z17*par[21]+z18*par[22])


  epsilon = log(y) - (front_g)

  probg = (2/sigma) * dnorm(epsilon/sigma, mean=0, sd=1) * (pnorm((-epsilon*lambda)/sigma, mean=0, sd=1))


  lnprobg = log(probg)


  logd = -sum(lnprobg)

}



## SETTING THE LOWER AND UPPER BOUNDS OF THE PARAMETER VALUES.

lower=c(0, 0, -10000, -10000, -10000, -10000, -10000, -10000, -10000, -10000, -10000, -10000, -10000,
        -10000, -10000, -10000, -10000, -10000, -10000, -10000, -10000, -10000)

upper=c(1000, 1000, 10000, 10000, 10000, 10000, 10000, 10000, 10000, 10000, 10000, 10000, 10000, 10000,
        10000,10000,10000,10000,10000,10000,10000,10000,10000)

## CALLING THE FUNCTION WITH INITIAL RANDOM VALUES INSIDE THE BOUNDS

Output.GenSA <- GenSA(par = NULL, fn = minimiser,lower = lower, upper = upper,
                      control=list(nb.stop.improvement=200000000, temperature=5000000000, maxit=50000, max.time=3600,
                                   simple.function=FALSE, verbose=TRUE, max.call=1e8))

fn.call.GenSA = Output.GenSA$counts

beta <- Output.GenSA$par

cat("GenSA call functions", fn.call.GenSA, "times.\n")


## PRINTING THE RESULTS

Output.GenSA[c("value","par")]
```

A.4.2 LRT

```
## LRT:
p_value=pchisq(-2*log(exp(-(-291.2876)+(-289.7524))), 15, lower.tail = FALSE)
p_value
```

A.4.3 SCC

```
##Test for association between paired samples, using SCC
cor.test(VB, V100, method = "spearman")



## SCC
CorrCoeffSpearman <- cor(All18Par, method = "spearman")
```

A.4.4 Brute-Force Search and Parallel Computations

```
## Parallel calculations

cores=detectCores()

c1 = makeCluster(cores[1]-1)

registerDoParallel(c1)


## A vector including the GPs to be verified

geo = c('MeanMinDCathsFullR','VR','AreaCath/MaxSPros','HMaxVB','HMeanVR','HMaxVR','MeanDCaths')

## A vector including the DPs to be studied
dosi = c( 'V100')


## To create a list of all the possible combination of the GPs

combi = do.call(c, lapply(seq_along(geo), combn, x = geo, simplify = FALSE))


# The lower and upper bounds applicable for the GPs

bound_min <- c(-10000, -10000, -10000, -10000, -10000, -10000, -10000, -10000, -10000, -10000,
               -10000, -10000, -10000, -10000, -10000, -10000, -10000)

names(bound_min) <- c('VCTV','VB','VR','VU','HMaxVB','HMeanVB','H95%VB','HMaxVR','HMeanVR','H95%VR','HMaxVU',
                      'HMeanVU','H95%VU','NCath/MaxSPros','AreaCath/MaxSPros','MeanDCaths','MeanMinDCathsHalfR','MeanMinDCathsFullR'

bound_max <- c(10000, 10000, 10000, 10000, 10000, 10000, 10000, 10000, 10000, 10000, 10000,
               10000, 10000, 10000, 10000, 10000, 10000, 10000)

names(bound_max) <- c('VCTV','VB','VR','VU','HMaxVB','HMeanVB','H95%VB','HMaxVR','HMeanVR','H95%VR','HMaxVU',
                      'HMeanVU','H95%VU','NCath/MaxSPros','AreaCath/MaxSPros','MeanDCaths','MeanMinDCathsHalfR','MeanMinDCathsFullR'




## Iteration on all the possible combinations in parallel

for (dose in dosi) {

    x <- foreach(i = 1:length(combi), .packages=c('GenSA','dplyr','jsonlite'), .combine = bind_rows, .multicombine = T, .verbose = T) %dopar%


    ## The lower and upper bounds applicable for sigma_u, sigma_v, a0, and a1

    param_min = c(0,0,-10000,-10000)
    param_max = c(1000,1000,10000,10000)

    ## loop iterating over each GPs of a combination

    for (a in combi[[i]]){
      param_max = append(param_max, bound_max[[a]])
      param_min = append(param_min, bound_min[[a]])
    }
```

```
## In the case of having 18 GPs:

if (length(combi[[i]]) == 18) {
  front_g = a0 + a1*log(par[5]*data[combi[[i]][1]][complete.cases(data[dose]), ]
                        + par[6]*data[combi[[i]][2]][complete.cases(data[dose]), ]
                        + par[7]*data[combi[[i]][3]][complete.cases(data[dose]), ]
                        + par[8]*data[combi[[i]][4]][complete.cases(data[dose]), ]
                        + par[9]*data[combi[[i]][5]][complete.cases(data[dose]), ]
                        + par[10]*data[combi[[i]][6]][complete.cases(data[dose]), ]
                        + par[11]*data[combi[[i]][7]][complete.cases(data[dose]), ]
                        + par[12]*data[combi[[i]][8]][complete.cases(data[dose]), ]
                        + par[13]*data[combi[[i]][9]][complete.cases(data[dose]), ]
                        + par[14]*data[combi[[i]][10]][complete.cases(data[dose]), ]
                        + par[15]*data[combi[[i]][11]][complete.cases(data[dose]), ]
                        + par[16]*data[combi[[i]][12]][complete.cases(data[dose]), ]
                        + par[17]*data[combi[[i]][13]][complete.cases(data[dose]), ]
                        + par[18]*data[combi[[i]][14]][complete.cases(data[dose]), ]
                        + par[19]*data[combi[[i]][15]][complete.cases(data[dose]), ]
                        + par[20]*data[combi[[i]][16]][complete.cases(data[dose]), ]
                        + par[21]*data[combi[[i]][17]][complete.cases(data[dose]), ]
                        + par[22]*data[combi[[i]][18]][complete.cases(data[dose]), ]   )
}


## Note: the cases for 17 GPs, 16 GPs, ..., 2 GPs are omitted here for simplicity.



 ## 1 GPs:

 if (length(combi[[i]]) == 1) { # 1 paramgeo
   front_g = a0 + a1*log(par[5]*data[combi[[i]][[1]]][complete.cases(data[dose]), ] )
 }

 epsilon = log(data[dose][complete.cases(data[dose]), ]) - (front_g)


 probg = (2/sigma) * dnorm(epsilon/sigma, mean=0, sd=1) * (pnorm((-epsilon*lambda)/sigma, mean=0, sd=1))


 lnprobg = log(probg)


 logd = -sum(lnprobg)



ep <- GenSA(par = NULL, fn = minimiser,lower = param_min, upper = param_max,
            control=list(nb.stop.improvement=200000000, temperature=5000000000, maxit=50000, max.time=3600,
                         simple.function=FALSE, verbose=TRUE, max.call=1e8))
```

Bibliography

[1] C. C. Society, "Canadian Cancer Statistics, A 2018 special report," *Canadian Cancer Society*, 2018. [Online]. Available: http://www.cancer.ca/~/media/cancer.ca/CW/cancerinformation/cancer101/Canadiancancerstatistics/Canadian-Cancer-Statistics-2018-EN.pdf?la=en

[2] W. Y. Song, K. Tanderup, and B. Pieters, *Emerging Technologies in Brachytherapy*, ser. Series in Medical Physics and Biomedical Engineering. CRC Press, 2017. [Online]. Available: https://books.google.ca/books?id=HVkkDwAAQBAJ

[3] G. Koukourakis, N. Kelekis, V. Armonis, and V. Kouloulias, "Brachytherapy for {Prostate} {Cancer}: {A} {Systematic} {Review}," *Advances in Urology*, vol. 2009, pp. 1–11, 2009. [Online]. Available: http://www.hindawi.com/journals/au/2009/327945/

[4] A. Challapalli, E. Jones, C. Harvey, G. O. Hellawell, and S. A. Mangar, "High dose rate prostate brachytherapy: an overview of the rationale, experience and emerging applications in the treatment of prostate cancer," *The British Journal of Radiology*, vol. 85, no. special_issue_1, pp. S18–S27, 2012. [Online]. Available: https://doi.org/10.1259/bjr/15403217

[5] R. Banerjee and M. Kamrava, "Brachytherapy in the treatment of cervical cancer: a review," *International journal of women's health*, vol. 6, pp. 555–564, 2014. [Online]. Available: https://www.ncbi.nlm.nih.gov/pubmed/24920937

[6] X. Deng, H. Wu, F. Gao, Y. Su, Q. Li, S. Liu, and J. Cai, "Brachytherapy in the treatment of breast cancer," *International Journal of Clinical Oncology*, vol. 22, no. 4, pp. 641–650, 2017. [Online]. Available: https://doi.org/10.1007/s10147-017-1155-5

[7] R. Bhalavat, M. Chandra, V. Pareek, L. Nellore, K. George, N. P., and P. Bauskar, "High-dose-rate interstitial brachytherapy in head and neck cancer: do we need a look back into a forgotten art – a single institute experience," *Journal of Contemporary Brachytherapy*, vol. 9, no. 2, pp. 124–131, 2017. [Online]. Available: http://dx.doi.org/10.5114/jcb.2017.67147

[8] R. Walstam, "Remotely-controlled afterloading radiotherapy apparatus. (A preliminary report)," *Physics in Medicine and Biology*, vol. 7, pp. 225–228, 1962. [Online]. Available: https://eurekamag.com/research/050/169/050169291.php

[9] J. F. Williamson, "Brachytherapy technology and physics practice since 1950: a half-century of progress," *Physics in Medicine and Biology*, vol. 51, no. 13, p. R303, 2006. [Online]. Available: http://stacks.iop.org/0031-9155/51/i=13/a=R18

[10] B. R. Thomadsen, J. F. Williamson, M. J. Rivard, and A. S. Meigooni, "Anniversary Paper: Past and current issues, and trends in brachytherapy physics," *Medical Physics*, vol. 35, no. 10, pp. 4708–4723, 2008. [Online]. Available: https://aapm.onlinelibrary.wiley.com/doi/abs/10.1118/1.2981826

[11] M. J. Rivard, J. L. M. Venselaar, and L. Beaulieu, "The evolution of brachytherapy treatment planning," *Medical Physics*, vol. 36, no. 6Part1, pp. 2136–2153, 2009. [Online]. Available: https://aapm.onlinelibrary.wiley.com/doi/abs/10.1118/1.3125136

[12] P. Grimm and J. Sylvester, "Advances in brachytherapy." *Reviews in urology*, vol. 6 Suppl 4, no. Suppl 4, pp. 37–48, 2004. [Online]. Available: http://www.ncbi.nlm.nih.gov/pubmed/16985869http://www.ncbi.nlm.nih.gov/pubmed/16985869

[13] C. Haie-Meder, R. Potter, E. Van Limbergen, E. Briot, M. De Brabandere, J. Dimopoulos, I. Dumas, T. P. Hellebust, C. Kirisits, S. Lang, S. Muschitz, J. Nevinson, A. Nulens, P. Petrow, and N. Wachter-Gerstner, "Recommendations from Gynaecological (GYN) GEC-ESTRO Working Group (I): Concepts and terms in 3D image based 3D treatment planning in cervix cancer brachytherapy with emphasis on MRI assessment of GTV and CTV," *Radiotherapy and Oncology*, vol. 74, no. 3, pp. 235–245, 2005. [Online]. Available: http://www.sciencedirect.com/science/article/pii/S0167814004005791

[14] R. Potter, C. Haie-Meder, E. Van Limbergen, I. Barillot, M. De Brabandere, J. Dimopoulos, I. Dumas, B. Erickson, S. Lang, A. Nulens, P. Petrow, J. Rownd, and C. Kirisits, "Recommendations from gynaecological (GYN) GEC ESTRO working group (II): Concepts and terms in 3D image-based treatment planning in cervix cancer brachytherapy - 3D dose volume parameters and aspects of 3D image-based anatomy, radiation physics, radiobiolo," *Radiotherapy and Oncology*, vol. 78, no. 1, pp. 67–77, 2006. [Online]. Available: https://doi.org/10.1016/j.radonc.2005.11.014

[15] J. Venselaar, A. S. Meigooni, D. Baltas, and P. J. Hoskin, *Comprehensive Brachytherapy: Physical and Clinical Aspects*, ser. Comprehensive Brachytherapy: Physical and Clinical Aspects. Taylor & Francis, 2012. [Online]. Available: https://books.google.ca/books?id=ZeQ51ZlqQPkC

[16] P. Hoskin and C. Coyle, *Radiotherapy in Practice - Brachytherapy*, Oxford, UK, 2013. [Online]. Available: http://oxfordmedicine.com/view/10.1093/med/9780199600908.001.0001/med-9780199600908

[17] M. D. F. Phillip M. Devlin, *Brachytherapy, Second Edition: Applications and Techniques*. Springer Publishing Company, 2015. [Online]. Available: https://books.google.ca/books?id=MFfSCgAAQBAJ

[18] P. Montemaggi, M. Trombetta, and L. W. Brady, *Brachytherapy: An International Perspective*, ser. Medical Radiology. Springer International Publishing, 2016. [Online]. Available: https://books.google.ca/books?id=45sFDAAAQBAJ

[19] G. Ibbott, C.-M. Ma, D. W. O. Rogers, S. M. Seltzer, and J. F. Williamson, "Anniversary Paper: Fifty years of AAPM involvement in radiation dosimetry," *Medical Physics*, vol. 35, no. 4, pp. 1418–1427, 2008. [Online]. Available: https://aapm.onlinelibrary.wiley.com/doi/abs/10.1118/1.2868765

[20] K. Tanderup, P. J. Eifel, C. M. Yashar, R. Pötter, and P. W. Grigsby, "Curative radiation therapy for locally advanced cervical cancer: brachytherapy is NOT optional." *International journal of radiation oncology, biology, physics*, vol. 88, no. 3, pp. 537–9, 3 2014. [Online]. Available: http://www.ncbi.nlm.nih.gov/pubmed/24411631

[21] J. Skowronek, "Low-dose-rate or high-dose-rate brachytherapy in treatment of prostate cancer - Between options," *Journal of contemporary brachytherapy*, vol. 5, no. 1, pp. 33–41, 2013. [Online]. Available: http://dx.doi.org/10.5114/jcb.2013.34342

[22] J. J. Mazeron, P. Scalliet, E. V. Limbergen, and E. Lartigau, "Radiobiology of Brachytherapy and the Dose-Rate Effect," *GEC-ESTRO handbook*, pp. 1–10, 2003. [Online]. Available: http://estro-education.org/publications/Documents/GECESTROHandbookofBrachytherapy.html

[23] F. Giovanni and others, "Low dose rate brachytherapy (LDR-BT) as monotherapy for early stage prostate cancer in Italy: practice and outcome analysis in a series of 2237 patients from 11 institutions," *The British Journal of Radiology*, vol. 89, no. 1065, p. 20150981, 2016. [Online]. Available: https://doi.org/10.1259/bjr.20150981

[24] S. Zuber, S. Weiß, D. Baaske, M. Schöpe, S. Stevens, S. Bodis, and D. R. Zwahlen, "Iodine-125 seed brachytherapy for early stage prostate cancer: a single-institution review," *Radiation Oncology*, vol. 10, no. 1, p. 49, 2 2015. [Online]. Available: https://doi.org/10.1186/s13014-015-0349-0

[25] L. Potters, "Iodine-125 vs. Palladium-103: Long-term complications," *International Journal of Cancer*, vol. 90, no. 2, p. 110, 2000. [Online]. Available: https://onlinelibrary.wiley.com/doi/abs/10.1002/%28SICI%291097-0215%2820000420%2990%3A2%3C110%3A%3AAID-IJC7%3E3.0.CO%3B2-8

[26] R. Paul, R. Hofmann, J. U. Schwarzer, R. Stepan, H. J. Feldmann, P. Kneschaurek, M. Molls, and R. Hartung, "Iridium 192 high-dose-rate brachytherapy? a useful alternative therapy for

localized prostate cancer?" *World Journal of Urology*, vol. 15, no. 4, pp. 252–256, 8 1997. [Online]. Available: http://link.springer.com/10.1007/BF01367663

[27] T. P. Mate, J. E. Gottesman, J. Hatton, M. Gribble, and L. V. Hollebeke, "High dose-rate afterloading 192iridium prostate brachytherapy: feasibility report," *International Journal of Radiation Oncology*Biology*Physics*, vol. 41, no. 3, pp. 525–533, 1998. [Online]. Available: http://www.sciencedirect.com/science/article/pii/S0360301698000972

[28] M. Edgren, A. M. Ekelund, P. Albertsson, L. M. Lundberg, A. Ullen, S. Levitt, S. Nilsson, and B. Lennernäs, "High dose-rate brachytherapy of prostate cancer utilising Iridium-192 after-loading technique: technical and methodological aspects." *International journal of oncology*, vol. 29, no. 6, pp. 1517–24, 12 2006. [Online]. Available: http://www.ncbi.nlm.nih.gov/pubmed/17088991

[29] N. Zaorsky, B. Davis, P. Nguyen, T. Showalter, P. J. Hoskin, Y. Yoshioka, G. Morton, and E. Horwitz, "The evolution of brachytherapy for prostate cancer," *Nature Reviews Urology*, vol. 14, pp. 415–439, 2017. [Online]. Available: https://doi.org/10.1038/nrurol.2017.76

[30] D. Demanes, M. Gilhezan, L. Schour, G. Gustafson, D. Hill, K. Marvin, I. Bernstein, and A. Martinez, "High Dose Rate Brachytherapy (HDR-BT) as Monotherapy for Favorable Prostate Cancer: Excellent 5-Year Control Rates and Low Toxicity," *International Journal of Radiation Oncology*Biology*Physics*, vol. 69, no. 3, p. S83, 11 2007. [Online]. Available: https://linkinghub.elsevier.com/retrieve/pii/S0360301607013326

[31] M. Ghilezan, A. Martinez, G. Gustason, D. Krauss, J. V. Antonucci, P. Chen, J. Fontanesi, M. Wallace, H. Ye, A. Casey, E. Sebastian, L. Kim, and A. Limbacher, "High-Dose-Rate Brachytherapy as Monotherapy Delivered in Two Fractions Within One Day for Favorable/Intermediate-Risk Prostate Cancer: Preliminary Toxicity Data," *International Journal of Radiation Oncology*Biology*Physics*, vol. 83, no. 3, pp. 927–932, 2012. [Online]. Available: http://www.sciencedirect.com/science/article/pii/S0360301611006602

[32] T. Nohara, A. Mizokami, T. Kumano, K. Shigehara, H. Konaka, K. Yoshifumi, K. Yasuhide, K. Izumi, K. Narimoto, and M. Namiki, "Clinical Results of Iridium-192 High Dose Rate Brachytherapy with External Beam Radiotherapy," *Japanese Journal of Clinical Oncology*, vol. 40, no. 7, pp. 677–683, 2010. [Online]. Available: http://dx.doi.org/10.1093/jjco/hyq016

[33] N. G. Zaorsky, A. S. Harrison, E. J. Trabulsi, L. G. Gomella, T. N. Showalter, M. D. Hurwitz, A. P. Dicker, and R. B. Den, "Evolution of advanced technologies in prostate cancer radiotherapy," *Nature Reviews Urology*, vol. 10, no. 10, pp. 565–579, 10 2013. [Online]. Available: http://www.nature.com/articles/nrurol.2013.185

[34] S. B. Johnson, N. H. Lester-Coll, J. R. Kelly, B. H. Kann, J. B. Yu, and S. K. Nath, "Brachytherapy Boost Utilization and Survival in Unfavorable-risk Prostate Cancer,"

European Urology, vol. 72, no. 5, pp. 738–744, 11 2017. [Online]. Available: http://www.ncbi.nlm.nih.gov/pubmed/28688613http://www.ncbi.nlm.nih.gov/pubmed/28688613

[35] S. Lazarev, M. R. Thompson, N. N. Stone, and R. G. Stock, "Low-dose-rate brachytherapy for prostate cancer: outcomes at >10 years of follow-up," *BJU International*, vol. 121, no. 5, pp. 781–790, 2018. [Online]. Available: https://onlinelibrary.wiley.com/doi/abs/10.1111/bju.14122

[36] R. Chicas-Sett, D. Farga, M. J. Perez-Calatayud, F. Celada, S. Roldan, V. Fornes-Ferrer, B. Ibanez-Rosello, A. Tormo, J. M. Benlloch, and J. Perez-Calatayud, "High-dose-rate brachytherapy boost for prostate cancer: Analysis of dose-volume histogram parameters for predicting late rectal toxicity," *Brachytherapy*, vol. 16, no. 3, pp. 511–517, 2017. [Online]. Available: http://www.sciencedirect.com/science/article/pii/S1538472117300508

[37] A. T. Falk, S. Demontoy, E. Chamorey, M.-E. Chand, M. Gautier, D. Azria, S. Zaki, D. Chevallier, D. L. C. Kee, and J.-M. Hannoun-Lévi, "High-dose-rate brachytherapy boost for prostate cancer: Comparison of three different fractionation schemes," *Brachytherapy*, vol. 16, no. 5, pp. 993–999, 2017. [Online]. Available: http://www.sciencedirect.com/science/article/pii/S1538472117303999

[38] P. J. Hoskin, A. Colombo, A. Henry, P. Niehoff, T. Paulsen Hellebust, F.-A. Siebert, and G. Kovacs, "{GEC}{ESTRO} recommendations on high dose rate afterloading brachytherapy for localised prostate cancer: {An} update," *Radiotherapy and Oncology*, vol. 107, no. 3, pp. 325–332, 2013. [Online]. Available: http://linkinghub.elsevier.com/retrieve/pii/S0167814013002004

[39] S. Hoffelt, L. M. Marshall, M. Garzotto, A. Hung, J. Holland, and T. M. Beer, "A comparison of CT scan to transrectal ultrasound-measured prostate volume in untreated prostate cancer," *International Journal of Radiation Oncology*Biology*Physics*, vol. 57, no. 1, pp. 29–32, 2003. [Online]. Available: http://www.sciencedirect.com/science/article/pii/S0360301603005091

[40] W. L. Smith, C. Lewis, G. Bauman, G. Rodrigues, D. D'Souza, R. Ash, D. Ho, V. Venkatesan, D. Downey, and A. Fenster, "Prostate volume contouring: A 3D analysis of segmentation using 3DTRUS, CT, and MR," *International Journal of Radiation Oncology*Biology*Physics*, vol. 67, no. 4, pp. 1238–1247, 2007. [Online]. Available: http://www.sciencedirect.com/science/article/pii/S0360301606035115

[41] B. E. Weiss, A. J. Wein, S. B. Malkowicz, and T. J. Guzzo, "Comparison of prostate volume measured by transrectal ultrasound and magnetic resonance imaging: Is transrectal ultrasound suitable to determine which patients should undergo active surveillance?" *Urologic Oncology: Seminars and Original Investigations*, vol. 31, no. 8, pp. 1436–1440, 2013. [Online]. Available: http://www.sciencedirect.com/science/article/pii/S107814391200083X

[42] J. S. Lee and B. H. Chung, "Transrectal Ultrasound versus Magnetic Resonance Imaging in the Estimation of Prostate Volume as Compared with Radical Prostatectomy Specimens," *Urologia Internationalis*, vol. 78, no. 4, pp. 323–327, 2007. [Online]. Available: http://www.ncbi.nlm.nih.gov/pubmed/17495490https://www.karger.com/Article/FullText/100836

[43] P. W. McLaughlin, V. Narayana, D. G. Drake, B. M. Miller, L. Marsh, J. Chan, R. Gonda, R. J. Winfield, and P. L. Roberson, "Comparison of MRI pulse sequences in defining prostate volume after permanent implantation," *International Journal of Radiation Oncology*Biology*Physics*, vol. 54, no. 3, pp. 703–711, 2002. [Online]. Available: http://www.sciencedirect.com/science/article/pii/S0360301602029917

[44] M. Whitaker, G. Hruby, A. Lovett, and N. Patanjali, "Prostate cancer brachytherapy Prostate HDR brachytherapy catheter displacement between planning and treatment delivery," *Radiotherapy and Oncology*, vol. 101, pp. 490–494, 2011. [Online]. Available: https://ac-els-cdn-com.acces.bibl.ulaval.ca/S0167814011004452/1-s2.0-S0167814011004452-main.pdf?_tid=fc04b249-8ecc-4429-93a2-27c6a49926e8&acdnat=1548780711_244900102d63c6913f30f757f8b7b3a1

[45] S. Kawakami, H. Ishiyama, T. Terazaki, I. Soda, T. Satoh, M. Kitano, S. Kurosaka, A. Sekiguchi, S. Komori, M. Iwamura, and K. Hayakawa, "Catheter displacement prior to the delivery of high-dose-rate brachytherapy in the treatment of prostate cancer patients." *Journal of contemporary brachytherapy*, vol. 6, no. 2, pp. 161–6, 6 2014. [Online]. Available: http://www.ncbi.nlm.nih.gov/pubmed/25097556http://www.ncbi.nlm.nih.gov/pubmed/25097556

[46] S. J. Damore, A. M. Syed, A. A. Puthawala, and A. Sharma, "Needle displacement during HDR brachytherapy in the treatment of prostate cancer." *International journal of radiation oncology, biology, physics*, vol. 46, no. 5, pp. 1205–11, 3 2000. [Online]. Available: http://www.ncbi.nlm.nih.gov/pubmed/10725633

[47] W. Foster, J. A. M. Cunha, I.-C. Hsu, V. Weinberg, D. Krishnamurthy, and J. Pouliot, "Dosimetric Impact of Interfraction Catheter Movement in High-Dose Rate Prostate Brachytherapy," *International Journal of Radiation Oncology*Biology*Physics*, vol. 80, no. 1, pp. 85–90, 5 2011. [Online]. Available: http://www.ncbi.nlm.nih.gov/pubmed/20605353http://www.ncbi.nlm.nih.gov/pubmed/20605353

[48] P. J. Hoskin, P. J. Bownes, P. Ostler, K. Walker, and L. Bryant, "High dose rate afterloading brachytherapy for prostate cancer: catheter and gland movement between fractions." *Radiotherapy and oncology : journal of the European Society for Therapeutic Radiology and Oncology*, vol. 68, no. 3, pp. 285–8, 9 2003. [Online]. Available: http://www.ncbi.nlm.nih.gov/pubmed/13129636

[49] E. Mullokandov and G. Gejerman, "Analysis of serial CT scans to assess template and catheter movement in prostate HDR brachytherapy," *International Journal of Radiation*

*Oncology*Biology*Physics*, vol. 58, no. 4, pp. 1063–1071, 3 2004. [Online]. Available: http://www.ncbi.nlm.nih.gov/pubmed/15001246http://www.ncbi.nlm.nih.gov/pubmed/15001246

[50] G. C. Morton, "High-dose-rate brachytherapy boost for prostate cancer: rationale and technique," *Journal of Contemporary Brachytherapy*, vol. 6, no. 3, pp. 323–330, 2014. [Online]. Available: https://www.ncbi.nlm.nih.gov/pmc/articles/PMC4200189/pdf/JCB-6-23618.pdf

[51] "High Dose Rate Brachytherapy for Prostate Cancer, Radiation Oncology Consultants, Chicago Area Cancer Care," 2018. [Online]. Available: http://chicagocancer.com/our-expertise/treatments-and-technology/high-dose-rate-brachytherapy-for-prostate-cancer/

[52] R. Nath, L. L. Anderson, G. Luxton, K. A. Weaver, J. F. Williamson, and A. S. Meigooni, "Dosimetry of interstitial brachytherapy sources: Recommendations of the AAPM Radiation Therapy Committee Task Group No. 43," *Medical Physics*, vol. 22, no. 2, pp. 209–234, 1995. [Online]. Available: https://aapm.onlinelibrary.wiley.com/doi/abs/10.1118/1.597458

[53] M. J. Rivard, B. M. Coursey, L. A. DeWerd, W. F. Hanson, M. Saiful Huq, G. S. Ibbott, M. G. Mitch, R. Nath, and J. F. Williamson, "Update of AAPM Task Group No. 43 Report: A revised AAPM protocol for brachytherapy dose calculations," *Medical Physics*, vol. 31, no. 3, pp. 633–674, 2004. [Online]. Available: https://aapm.onlinelibrary.wiley.com/doi/abs/10.1118/1.1646040

[54] M. J. Rivard, W. M. Butler, L. A. DeWerd, M. S. Huq, G. S. Ibbott, A. S. Meigooni, C. S. Melhus, M. G. Mitch, R. Nath, and J. F. Williamson, "Supplement to the 2004 update of the AAPM Task Group No. 43 Report," *Medical Physics*, vol. 34, no. 6Part1, pp. 2187–2205, 2007. [Online]. Available: https://aapm.onlinelibrary.wiley.com/doi/abs/10.1118/1.2736790

[55] M. J. Rivard, F. Ballester, W. M. Butler, L. A. DeWerd, G. S. Ibbott, A. S. Meigooni, C. S. Melhus, M. G. Mitch, R. Nath, and P. Papagiannis, "Supplement 2 for the 2004 update of the AAPM Task Group No. 43 Report: Joint recommendations by the AAPM and GEC-ESTRO," *Medical Physics*, vol. 44, no. 9, pp. e297–e338, 9 2017. [Online]. Available: http://www.ncbi.nlm.nih.gov/pubmed/28644913http://www.ncbi.nlm.nih.gov/pubmed/28644913

[56] C. D. Lee, "Recent developments and best practice in brachytherapy treatment planning," *The British Journal of Radiology*, vol. 87, no. 1041, p. 20140146, 2014. [Online]. Available: https://doi.org/10.1259/bjr.20140146

[57] J. Zhou, L. Zamdborg, and E. Sebastian, "Review of advanced catheter technologies in radiation oncology brachytherapy procedures." *Cancer management and research*, vol. 7, pp. 199–211, 2015. [Online]. Available: http://www.ncbi.nlm.nih.gov/pubmed/26203277http://www.ncbi.nlm.nih.gov/pubmed/26203277

[58] M. S. Peach, D. M. Trifiletti, and B. Libby, "Systematic Review of Focal Prostate Brachytherapy and the Future Implementation of Image-Guided Prostate HDR Brachytherapy Using MR-Ultrasound Fusion," *Prostate Cancer*, vol. 2016, pp. 1–13, 2016. [Online]. Available: http://www.ncbi.nlm.nih.gov/pubmed/27293899http://www.ncbi.nlm.nih.gov/pubmed/27293899http://www.ncbi.nlm.nih.gov/pubmed/27293899

[59] S. Banerjee, T. Kataria, D. Gupta, S. Goyal, S. S. Bisht, T. Basu, and A. Abhishek, "Use of ultrasound in image-guided high-dose-rate brachytherapy: enumerations and arguments," *Journal of Contemporary Brachytherapy*, vol. 9, no. 2, pp. 146–150, 2017. [Online]. Available: http://dx.doi.org/10.5114/jcb.2017.67456

[60] Y. Yoshioka, J. Itami, M. Oguchi, and T. Nakano, *Brachytherapy: Techniques and Evidences*. Springer Singapore, 2018. [Online]. Available: https://books.google.ca/books?id=rBdnDwAAQBAJ

[61] A. A. Martinez, I. Pataki, G. Edmundson, E. Sebastian, D. Brabbins, and G. Gustafson, "Phase II prospective study of the use of conformal high-dose-rate brachytherapy as monotherapy for the treatment of favorable stage prostate cancer: A feasibility report," *International Journal of Radiation Oncology Biology Physics*, vol. 49, no. 1, pp. 61–69, 2001. [Online]. Available: http://www.sciencedirect.com/science/article/pii/S0360301600014632

[62] J. Z. Wang, X. Li, C. X. Yu, and S. J. DiBiase, "The low α/β ratio for prostate cancer: What does the clinical outcome of HDR brachytherapy tell us?" *International Journal of Radiation Oncology*Biology*Physics*, vol. 57, no. 4, pp. 1101–1108, 2003. [Online]. Available: http://www.sciencedirect.com/science/article/pii/S0360301603007478

[63] S. M. Bentzen and M. A. Ritter, "The α/β ratio for prostate cancer: What is it, really?" *Radiotherapy and Oncology*, vol. 76, no. 1, pp. 1–3, 2005. [Online]. Available: http://www.sciencedirect.com/science/article/pii/S0167814005002227

[64] G. I.S., M. A.A., H. M., H. R., G. K., C. P.Y., and G. G.S., "High dose rate brachytherapy as prostate cancer monotherapy reduces toxicity compared to low dose rate palladium seeds," *Journal of Urology*, vol. 171, no. 3, pp. 1098–1104, 2004. [Online]. Available: http://www.embase.com/search/results?subaction=viewrecord&from=export&id=L38327535%0Ahttp://dx.doi.org/10.1097/01.ju.0000113299.34404.22

[65] D. E. Spratt, Z. S. Zumsteg, P. Ghadjar, M. A. Kollmeier, X. Pei, G. Cohen, W. Polkinghorn, Y. Yamada, and M. J. Zelefsky, "Comparison of high-dose (86.4 Gy) IMRT vs combined brachytherapy plus IMRT for intermediate-risk prostate cancer," *BJU International*, vol. 114, no. 3, pp. 360–367, 2013. [Online]. Available: https://onlinelibrary.wiley.com/doi/abs/10.1111/bju.12514

[66] F. Vicini, C. Vargas, G. Gustafson, G. Edmundson, and A. Martinez, "High dose rate brachytherapy in the treatment of prostate cancer," *World Journal of Urology*, vol. 21, no. 4, pp. 220–228, 9 2003. [Online]. Available: https://doi.org/10.1007/s00345-003-0358-8

[67] D. Lee, T. Li, M. Hallman, D. Chen, Y. Dong, B. Leachman, I. Veltchev, R. Greenberg, M. Sobczak, and E. Horwitz, "Comparison of Toxicities in High Dose Rate Versus Low Dose Rate Brachytherapy as Monotherapy in Patients with Low to Favorable Intermediate Risk Prostate Cancer," *International Journal of Radiation Oncology*Biology*Physics*, vol. 99, no. 2, p. E252, 2017. [Online]. Available: https://linkinghub.elsevier.com/retrieve/pii/S0360301617322587

[68] I. C. Hsu, Y. Yamada, E. Vigneault, and J. Pouliot, "American Brachytherapy Society Prostate High-Dose-Rate Task Group," *American Brachytherapy Society Guidelines*, 2008. [Online]. Available: https://www.google.com/url?sa=t&rct=j&q=&esrc=s&source=web&cd=1&cad=rja&uact=8&ved=2ahUKEwjky77Z_ZDgAhUl5oMKHWO4DQMQFjAAegQICRAC&url=https%3A%2F%2Fwww.americanbrachytherapy.org%2FABS%2Fassets%2Ffile%2Fpublic%2Fguidelines%2FHDRTaskGroup.pdf&usg=AOvVaw37ci4

[69] Y. Yamada, L. Rogers, D. J. Demanes, G. Morton, B. R. Prestidge, J. Pouliot, G. N. Cohen, M. Zaider, M. Ghilezan, I.-C. Hsu, and American Brachytherapy Society, "American Brachytherapy Society consensus guidelines for high-dose-rate prostate brachytherapy," *Brachytherapy*, vol. 11, no. 1, pp. 20–32, 1 2012. [Online]. Available: http://www.ncbi.nlm.nih.gov/pubmed/22265435https://linkinghub.elsevier.com/retrieve/pii/S1538472111004004

[70] D. Jones, "ICRU Report 50—Prescribing, Recording and Reporting Photon Beam Therapy," *Medical Physics*, vol. 21, no. 6, pp. 833–834. [Online]. Available: https://aapm.onlinelibrary.wiley.com/doi/abs/10.1118/1.597396

[71] N. G. Zaorsky, T. N. Showalter, G. A. Ezzell, P. L. Nguyen, D. G. Assimos, A. V. D'Amico, A. R. Gottschalk, G. S. Gustafson, S. R. Keole, S. L. Liauw, S. Lloyd, P. W. McLaughlin, B. Movsas, B. R. Prestidge, A. V. Taira, N. Vapiwala, and B. J. Davis, "ACR Appropriateness Criteria® external beam radiation therapy treatment planning for clinically localized prostate cancer, part I of II," *Advances in Radiation Oncology*, vol. 2, no. 1, pp. 62–84, 2017. [Online]. Available: http://www.sciencedirect.com/science/article/pii/S2452109416300562

[72] R. Banerjee, S.-J. Park, E. Anderson, D. J. Demanes, J. Wang, and M. Kamrava, "From whole gland to hemigland to ultra-focal high-dose-rate prostate brachytherapy: A dosimetric analysis," *Brachytherapy*, vol. 14, no. 3, pp. 366–372, 2015. [Online]. Available: http://www.sciencedirect.com/science/article/pii/S1538472115000021

[73] A. Lovett, M. Whitaker, G. Hruby, N. Patanjali, A. Dunning, and R. Ko, "Poster Discussion Abstract," *International Journal of Radiation Oncology, Biology, Physics*, vol. 75, no. 3 Supplement, pp. S156–S157, 2009.

[74] "RADIOTHERAPY RISK PROFILE Technical Manual," Tech. Rep., 2008. [Online]. Available: https://www.who.int/patientsafety/activities/technical/radiotherapy_risk_profile.pdf

[75] CPQR, "Quality Assurance Guidelines for Canadian Radiation Treatment Programs," 12 2015. [Online]. Available: http://www.cpqr.ca/wp-content/uploads/2013/09/QRT2015-12-03.pdf

[76] P. Dunscombe, H. Johnson, C. Arsenault, G. Mawko, J.-P. Bissonnette, and J. Seuntjens, "Development of quality control standards for radiation therapy equipment in Canada," *Journal of Applied Clinical Medical Physics*, vol. 8, no. 1, pp. 108–118, 2007. [Online]. Available: https://aapm.onlinelibrary.wiley.com/doi/abs/10.1120/jacmp.v8i1.2380

[77] K. L. Moore, R. S. Brame, D. A. Low, and S. Mutic, "Quantitative Metrics for Assessing Plan Quality," *Seminars in Radiation Oncology*, vol. 22, no. 1, pp. 62–69, 2012. [Online]. Available: http://www.sciencedirect.com/science/article/pii/S1053429611000968

[78] M. KL, B. RS, L. DA, and M. S, "Experience-Based Quality Control of Clinical Intensity-Modulated Radiotherapy Planning." *International Journal of Radiation Oncology, Biology, Physics*, vol. 81, no. 2, pp. 545–551, 2011. [Online]. Available: https://doi.org/10.1016/j.ijrobp.2010.11.030

[79] S. L. Berry, A. Boczkowski, R. Ma, J. G. Mechalakos, and M. A. Hunt, "Evaluating Interobserver Variability in Treatment Plan Output: Results of a Single-Institution Study," *International Journal of Radiation Oncology*Biology*Physics*, vol. 93, no. 3, Supplement, p. E572, 2015. [Online]. Available: http://www.sciencedirect.com/science/article/pii/S0360301615027522

[80] "ABS guidelines." [Online]. Available: https://www.americanbrachytherapy.org/guidelines/

[81] W. C. Schlegel, L. W. Brady, H. P. Heilmann, T. Bortfeld, M. Molls, and A. L. Grosu, *New Technologies in Radiation Oncology*, ser. Medical Radiology. Springer Berlin Heidelberg, 2006. [Online]. Available: https://books.google.ca/books?id=tdpDAAAAQBAJ

[82] "Intensity-modulated radiotherapy: current status and issues of interest," *International Journal of Radiation Oncology*Biology*Physics*, vol. 51, no. 4, pp. 880–914, 2001. [Online]. Available: http://www.sciencedirect.com/science/article/pii/S0360301601017497

[83] L. Veldeman, I. Madani, F. Hulstaert, G. D. Meerleer, M. Mareel, and W. D. Neve, "Evidence behind use of intensity-modulated radiotherapy: a systematic review of comparative clinical studies," *The Lancet Oncology*, vol. 9, no. 4, pp. 367–375, 2008. [Online]. Available: http://www.sciencedirect.com/science/article/pii/S1470204508700986

[84] R. Pötter, C. Kirisits, E. F. Fidarova, J. C. A. Dimopoulos, D. Berger, K. Tanderup, and J. C. Lindegaard, "Present status and future of high-precision image guided adaptive brachytherapy for cervix carcinoma," *Acta Oncologica*, vol. 47, no. 7, pp. 1325–1336, 2008. [Online]. Available: https://doi.org/10.1080/02841860802282794

[85] E. Lessard and J. Pouliot, "Inverse planning anatomy-based dose optimization for HDR-brachytherapy of the prostate using fast simulated annealing algorithm and dedicated objective function," *Medical Physics*, vol. 28, no. 5, pp. 773–779, 2001. [Online]. Available: https://aapm.onlinelibrary.wiley.com/doi/abs/10.1118/1.1368127

[86] V. Panettieri, R. L. Smith, N. J. Mason, and J. L. Millar, "Comparison of IPSA and HIPO inverse planning optimization algorithms for prostate HDR brachytherapy," *Journal of Applied Clinical Medical Physics*, vol. 15, no. 6, pp. 256–266, 11 2014. [Online]. Available: http://www.ncbi.nlm.nih.gov/pubmed/25493531http://www.ncbi.nlm.nih.gov/pubmed/25493531http://www.ncbi.nlm.nih.gov/pubmed/25493531

[87] C. H. Choi, S.-Y. Park, J. M. Park, H.-G. Wu, J.-H. Kim, and J.-i. Kim, "Comparison of the IPSA and HIPO algorithms for interstitial tongue high-dose-rate brachytherapy," *PLOS ONE*, vol. 13, no. 10, p. e0205229, 10 2018. [Online]. Available: http://www.ncbi.nlm.nih.gov/pubmed/30286187http://www.ncbi.nlm.nih.gov/pubmed/30286187http://www.ncbi.nlm.nih.gov/pubmed/30286187

[88] W. Meeusen and J. van den Broeck, "Efficiency Estimation from Cobb-Douglas Production Functions with Composed Error," *International Economic Review*, vol. 18, no. 2, pp. 435–444, 1977. [Online]. Available: https://econpapers.repec.org/RePEc:ier:iecrev:v:18:y:1977:i:2:p:435-44

[89] D. Aigner, C. Lovell, and P. Schmidt, "Formulation and estimation of stochastic frontier production function models," *Journal of Econometrics*, vol. 6, no. 1, pp. 21–37, 1977. [Online]. Available: http://www.sciencedirect.com/science/article/pii/0304407677900525

[90] T. P. Hellebust, C. Kirisits, D. Berger, J. Perez-Calatayud, M. De Brabandere, A. De Leeuw, I. Dumas, R. Hudej, G. Lowe, R. Wills, and K. Tanderup, "Recommendations from Gynaecological (GYN) GEC-ESTRO working group: Considerations and pitfalls in commissioning and applicator reconstruction in 3D image-based treatment planning of cervix cancer brachytherapy," *Radiotherapy and Oncology*, vol. 96, no. 2, pp. 153–160, 2010. [Online]. Available: https://doi.org/10.1016/j.radonc.2010.06.004

[91] C. Kolotas, D. Baltas, and N. Zamboglou, "CT-Based Interstitial HDR Brachytherapy," *Strahlentherapie und Onkologie*, vol. 175, no. 9, pp. 419–427, 9 1999. [Online]. Available: http://link.springer.com/10.1007/s000660050031

[92] C. Ménard, R. C. Susil, P. Choyke, G. S. Gustafson, W. Kammerer, H. Ning, R. W. Miller, K. L. Ullman, N. Sears Crouse, S. Smith, E. Lessard, J. Pouliot, V. Wright, E. McVeigh, C. N. Coleman, and K. Camphausen, "MRI-guided HDR prostate brachytherapy in standard 1.5T scanner." *International journal of radiation oncology, biology, physics*, vol. 59, no. 5, pp. 1414–23, 8 2004. [Online]. Available: http://www.ncbi.nlm.nih.gov/pubmed/15275727http://www.ncbi.nlm.nih.gov/pubmed/15275727

[93] I.-C. J. Hsu, A. R. Cabrera, V. Weinberg, J. Speight, A. R. Gottschalk, M. Roach, and K. Shinohara, "Combined modality treatment with high-dose-rate brachytherapy boost for locally advanced prostate cancer." *Brachytherapy*, vol. 4, no. 3, pp. 202–6, 1 2005. [Online]. Available: http://www.ncbi.nlm.nih.gov/pubmed/16182220

[94] R. Holly, G. C. Morton, R. Sankreacha, N. Law, T. Cisecki, D. A. Loblaw, and H. T. Chung, "Use of cone-beam imaging to correct for catheter displacement in high dose-rate prostate brachytherapy." *Brachytherapy*, vol. 10, no. 4, pp. 299–305, 7 2011. [Online]. Available: http://www.ncbi.nlm.nih.gov/pubmed/21190903

[95] A. J. G. Even, T. T. Nuver, H. Westendorp, C. J. Hoekstra, C. H. Slump, and A. W. Minken, "High-dose-rate prostate brachytherapy based on registered transrectal ultrasound and in-room cone-beam CT images." *Brachytherapy*, vol. 13, no. 2, pp. 128–36, 3 2014. [Online]. Available: http://www.ncbi.nlm.nih.gov/pubmed/24041955

[96] P. Blanchard, C. Ménard, and S. J. Frank, "Clinical use of magnetic resonance imaging across the prostate brachytherapy workflow," *Brachytherapy*, vol. 16, no. 4, pp. 734–742, 7 2017. [Online]. Available: http://www.ncbi.nlm.nih.gov/pubmed/28153700

[97] B. M. Carey, "Imaging for Post-implant Dosimetry," in *Interstitial Prostate Brachytherapy*. Berlin, Heidelberg: Springer Berlin Heidelberg, 2013, pp. 119–140. [Online]. Available: http://link.springer.com/10.1007/978-3-642-36499-0_9

[98] R. R. Upreti, S. Dayananda, R. L. Bhalawat, G. N. Bedre, and D. D. Deshpande, "Evaluation of radiograph-based interstitial implant dosimetry on computed tomography images using dose volume indices for head and neck cancer." *Journal of medical physics*, vol. 32, no. 2, pp. 60–4, 4 2007. [Online]. Available: http://www.ncbi.nlm.nih.gov/pubmed/21157536http://www.ncbi.nlm.nih.gov/pubmed/21157536

[99] R. K. Das, R. Patel, H. Shah, H. Odau, and R. R. Kuske, "3D CT–based high-dose-rate breast brachytherapy implants: treatment planning and quality assurance," *International Journal of Radiation Oncology*Biology*Physics*, vol. 59, no. 4, pp. 1224–1228, 7 2004. [Online]. Available: http://www.ncbi.nlm.nih.gov/pubmed/15234059http://www.ncbi.nlm.nih.gov/pubmed/15234059

[100] T. O. Henkel and F. Kahmann, "Permanent brachytherapy: prostate seed implants as an out-patient treatment." *Archivio italiano di urologia, andrologia : organo ufficiale [di] Societa italiana di ecografia urologica e nefrologica*, vol. 72, no. 4, pp. 295–301, 12 2000. [Online]. Available: http://www.ncbi.nlm.nih.gov/pubmed/11221059

[101] X. Yang, P. Rossi, T. Ogunleye, D. M. Marcus, A. B. Jani, H. Mao, W. J. Curran, and T. Liu, "Prostate CT segmentation method based on nonrigid registration in ultrasound-guided CT-based HDR prostate brachytherapy," *Medical Physics*, vol. 41, no. 11, p. 111915, 10 2014. [Online]. Available: http://doi.wiley.com/10.1118/1.4897615

[102] D. F. Dubois, B. R. Prestidge, L. A. Hotchkiss, J. J. Prete, and W. S. Bice, "Intraobserver and interobserver variability of MR imaging- and CT-derived prostate volumes after transperineal interstitial permanent prostate brachytherapy." *Radiology*, vol. 207, no. 3, pp. 785–9, 6 1998. [Online]. Available: http://www.ncbi.nlm.nih.gov/pubmed/9609905

[103] M. Roach, P. Faillace-Akazawa, C. Malfatti, J. Holland, and H. Hricak, "Prostate volumes defined by magnetic resonance imaging and computerized tomographic scans for three-dimensional conformal radiotherapy." *International journal of radiation oncology, biology, physics*, vol. 35, no. 5, pp. 1011–8, 7 1996. [Online]. Available: http://www.ncbi.nlm.nih.gov/pubmed/8751410

[104] M. Foskey, B. Davis, L. Goyal, S. Chang, E. Chaney, N. Strehl, S. Tomei, J. Rosenman, and S. Joshi, "Large deformation three-dimensional image registration in image-guided radiation therapy," *Physics in Medicine and Biology*, vol. 50, no. 24, pp. 5869–5892, 12 2005. [Online]. Available: http://stacks.iop.org/0031-9155/50/i=24/a=008?key=crossref.fb58193cebfdef3f784c24df1b9eed45

[105] W. Li, S. Liao, Q. Feng, W. Chen, and D. Shen, "Learning image context for segmentation of the prostate in CT-guided radiotherapy," *Physics in Medicine and Biology*, vol. 57, no. 5, pp. 1283–1308, 3 2012. [Online]. Available: http://stacks.iop.org/0031-9155/57/i=5/a=1283?key=crossref.2110f3cdaafd214bf42455816319df9a

[106] Shu Liao and Dinggang Shen, "A Feature-Based Learning Framework for Accurate Prostate Localization in CT Images," *IEEE Transactions on Image Processing*, vol. 21, no. 8, pp. 3546–3559, 8 2012. [Online]. Available: http://ieeexplore.ieee.org/document/6179993/

[107] S. Liao, Y. Gao, J. Lian, and D. Shen, "Sparse Patch-Based Label Propagation for Accurate Prostate Localization in CT Images," *IEEE Transactions on Medical Imaging*, vol. 32, no. 2, pp. 419–434, 2 2013. [Online]. Available: http://ieeexplore.ieee.org/document/6362228/

[108] Q. Feng, M. Foskey, W. Chen, and D. Shen, "Segmenting CT prostate images using population and patient-specific statistics for radiotherapy," *Medical Physics*, vol. 37, no. 8, pp. 4121–4132, 7 2010. [Online]. Available: http://doi.wiley.com/10.1118/1.3464799

[109] S. Chen, D. M. Lovelock, and R. J. Radke, "Segmenting the prostate and rectum in CT imagery using anatomical constraints." *Medical image analysis*, vol. 15, no. 1, pp. 1–11, 2 2011. [Online]. Available: http://www.ncbi.nlm.nih.gov/pubmed/20634121

[110] O. Acosta, J. Dowling, G. Drean, A. Simon, R. de Crevoisier, and P. Haigron, "Multi-Atlas-Based Segmentation of Pelvic Structures from CT Scans for Planning in Prostate Cancer Radiotherapy," in *Abdomen and Thoracic Imaging*. Boston, MA: Springer US, 2014, pp. 623–656. [Online]. Available: http://link.springer.com/10.1007/978-1-4614-8498-1_24

[111] N. R. Paterson, L. T. Lavallée, L. N. Nguyen, K. Witiuk, J. Ross, R. Mallick, W. Shabana, B. MacDonald, N. Scheida, D. Fergusson, F. Momoli, S. Cnossen, C. Morash, I. Cagiannos, and R. H. Breau, "Prostate volume estimations using magnetic resonance imaging and transrectal ultrasound compared to radical prostatectomy specimens," *Canadian Urological Association Journal*, vol. 10, no. 7-8, p. 264, 8 2016. [Online]. Available: http://www.ncbi.nlm.nih.gov/pubmed/27878049http://www.ncbi.nlm.nih.gov/pubmed/27878049http://www.ncbi.nlm.nih.gov/pubmed/27878049

[112] J. Sylvester, J. Blasko, and P. Grimm, "Transrectal Ultrasound-Guided Prostate Brachytherapy," in *Image-Guided Diagnosis and Treatment of Cancer*. Totowa, NJ: Humana Press, 2003, pp. 119–154. [Online]. Available: http://link.springer.com/10.1007/978-1-59259-422-1_6

[113] P. Niehoff and G. Kovács, "HDR brachytherapy for anal cancer." *Journal of gastrointestinal oncology*, vol. 5, no. 3, pp. 218–22, 6 2014. [Online]. Available: http://www.ncbi.nlm.nih.gov/pubmed/24982770http://www.ncbi.nlm.nih.gov/pubmed/24982770

[114] K. Narayan, S. van Dyk, D. Bernshaw, P. Khaw, L. Mileshkin, and S. Kondalsamy-Chennakesavan, "Ultrasound guided conformal brachytherapy of cervix cancer: survival, patterns of failure, and late complications." *Journal of gynecologic oncology*, vol. 25, no. 3, pp. 206–13, 7 2014. [Online]. Available: http://www.ncbi.nlm.nih.gov/pubmed/25045433http://www.ncbi.nlm.nih.gov/pubmed/25045433

[115] P. De Jean, L. Beaulieu, and A. Fenster, "Three-dimensional ultrasound system for guided breast brachytherapy," *Medical Physics*, vol. 36, no. 11, pp. 5099–5106, 10 2009. [Online]. Available: http://www.ncbi.nlm.nih.gov/pubmed/19994520http://www.ncbi.nlm.nih.gov/pubmed/19994520

[116] W. Maier, K. Henne, A. Krebs, and J. Schipper, "Endoscopic ultrasound-guided brachytherapy of head and neck tumours. A new procedure for controlled application." *The Journal of laryngology and otology*, vol. 113, no. 1, pp. 41–8, 1 1999. [Online]. Available: http://www.ncbi.nlm.nih.gov/pubmed/10341918

[117] U. Goyal, Y. Kim, H. A. Tiwari, R. Witte, and B. Stea, "A pilot study of ultrasound-guided electronic brachytherapy for skin cancer." *Journal of contemporary brachytherapy*, vol. 7, no. 5, pp. 374–80, 10 2015. [Online]. Available: http://www.ncbi.nlm.nih.gov/pubmed/26622244http://www.ncbi.nlm.nih.gov/pubmed/26622244

[118] T. Hellebust, "Place of modern imaging in brachytherapy planning," *Cancer/Radiothérapie*, vol. 22, no. 4, pp. 326–333, 6 2018. [Online]. Available: https://www.sciencedirect.com/science/article/pii/S1278321818300866?via%3Dihub

[119] R. M. G. et al., "Long-term outcome after elective irradiation of the pelvic lymphatics and local dose escalation using high-dose-rate brachytherapy for locally advanced prostate cancer,"

International Journal of Radiation Oncology, Biology, Physics, vol. 52, no. 1, pp. 81–90, 2002. [Online]. Available: https://doi.org/10.1016/S0360-3016(01)01758-8

[120] R. Alterovitz, E. Lessard, J. Pouliot, I.-C. J. Hsu, J. F. O'Brien, and K. Goldberg, "Optimization of HDR brachytherapy dose distributions using linear programming with penalty costs," *Medical Physics*, vol. 33, no. 11, pp. 4012–4019, 10 2006. [Online]. Available: http://www.ncbi.nlm.nih.gov/pubmed/17153381http://www.ncbi.nlm.nih.gov/pubmed/17153381

[121] L. C. Mendez and G. C. Morton, "High dose-rate brachytherapy in the treatment of prostate cancer." *Translational andrology and urology*, vol. 7, no. 3, pp. 357–370, 6 2018. [Online]. Available: http://www.ncbi.nlm.nih.gov/pubmed/30050796http://www.ncbi.nlm.nih.gov/pubmed/30050796

[122] Z. DD. and T. DA, "A novel method for accurate needle-tip identification in trans-rectal ultrasound-based high-dose-rate prostate brachytherapy." vol. 10, no. 6, pp. 466–473, 2011.

[123] M. Schmid, J. M. Crook, D. Batchelar, C. Araujo, D. Petrik, D. Kim, and R. Halperin, "A phantom study to assess accuracy of needle identification in real-time planning of ultrasound-guided high-dose-rate prostate implants," vol. 12, no. 1, pp. 56–64, 2013. [Online]. Available: https://doi.org/10.1016/j.brachy.2012.03.002

[124] W. M. Butler, W. S. Bice Jr., L. A. DeWerd, J. M. Hevezi, M. S. Huq, G. S. Ibbott, J. R. Palta, M. J. Rivard, J. P. Seuntjens, and B. R. Thomadsen, "Third-party brachytherapy source calibrations and physicist responsibilities: Report of the AAPM Low Energy Brachytherapy Source Calibration Working Group," *Medical Physics*, vol. 35, no. 9, pp. 3860–3865, 2008. [Online]. Available: https://aapm.onlinelibrary.wiley.com/doi/abs/10.1118/1.2959723

[125] S. M. Seltzer, P. J. Lamperti, R. Loevinger, M. G. Mitch, J. T. Weaver, and B. M. Coursey, "New National Air-Kerma-Strength Standards for (125)I and (103)Pd Brachytherapy Seeds." *Journal of research of the National Institute of Standards and Technology*, vol. 108, no. 5, pp. 337–358, 2003. [Online]. Available: http://www.ncbi.nlm.nih.gov/pubmed/27413614http://www.pubmedcentral.nih.gov/articlerender.fcgi?artid=PMC4847582

[126] L. Beaulieu, A. Carlsson Tedgren, J. F. Carrier, S. D. Davis, F. Mourtada, M. J. Rivard, R. M. Thomson, F. Verhaegen, T. A. Wareing, and J. F. Williamson, "Report of the Task Group 186 on model-based dose calculation methods in brachytherapy beyond the TG-43 formalism: Current status and recommendations for clinical implementation," *Medical Physics*, vol. 39, no. 10, pp. 6208–6236, 9 2012. [Online]. Available: http://doi.wiley.com/10.1118/1.4747264

[127] Y. Ma, F. Lacroix, M.-C. Lavallée, and L. Beaulieu, "Validation of the Oncentra Brachy Advanced Collapsed cone Engine for a commercial 192Ir source using heterogeneous geometries," *Brachytherapy*, vol. 14, no. 6, pp. 939–952, 2015. [Online]. Available: http://www.sciencedirect.com/science/article/pii/S1538472115005310

[128] J. Yang, "Oncentra brachytherapy planning system," *Medical Dosimetry*, vol. 43, pp. 141–149, 2018. [Online]. Available: https://doi.org/10.1016/j.meddos.2018.02.011

[129] A. M. Dinkla, R. van der Laarse, E. Kaljouw, B. R. Pieters, K. Koedooder, N. van Wieringen, and A. Bel, "A comparison of inverse optimization algorithms for HDR/PDR prostate brachytherapy treatment planning," *Brachytherapy*, vol. 14, no. 2, pp. 279–288, 3 2015. [Online]. Available: http://www.ncbi.nlm.nih.gov/pubmed/25447341http://www.ncbi.nlm.nih.gov/pubmed/25447341

[130] A. Karabis, P. Belotti, and D. Baltas, "Optimization of Catheter Position and Dwell Time in Prostate HDR Brachytherapy using HIPO and Linear Programming." Springer, Berlin, Heidelberg, 2009, pp. 612–615. [Online]. Available: http://link.springer.com/10.1007/978-3-642-03474-9_172

[131] A. Holm, T. Larsson, and A. Carlsson Tedgren, "Impact of using linear optimization models in dose planning for HDR brachytherapy," *Medical Physics*, vol. 39, no. 2, pp. 1021–1028, 2 2012. [Online]. Available: http://www.ncbi.nlm.nih.gov/pubmed/22320812

[132] E. Poulin, N. Varfalvy, S. Aubin, and L. Beaulieu, "Comparison of dose and catheter optimization algorithms in prostate high-dose-rate brachytherapy," *Brachytherapy*, vol. 15, no. 1, pp. 102–111, 1 2016. [Online]. Available: http://www.ncbi.nlm.nih.gov/pubmed/26561276http://www.ncbi.nlm.nih.gov/pubmed/26561276

[133] B. Lachance, D. Beliveau-Nadeau, E. Lessard, M. Chretien, I. C. J. Hsu, J. Pouliot, L. Beaulieu, and E. Vigneault, "Early clinical experience with anatomy-based inverse planning dose optimization for high-dose-rate boost of the prostate," *International Journal of Radiation Oncology Biology Physics*, vol. 54, no. 1, pp. 86–100, 9 2002. [Online]. Available: https://www.sciencedirect.com/science/article/pii/S0360301602028973

[134] I.-C. J. Hsu, E. Lessard, V. Weinberg, and J. Pouliot, "Comparison of inverse planning simulated annealing and geometrical optimization for prostate high-dose-rate brachytherapy," *Brachytherapy*, vol. 3, no. 3, pp. 147–152, 1 2004. [Online]. Available: https://www.sciencedirect.com/science/article/pii/S1538472104001308

[135] D. Jacob, A. Raben, A. Sarkar, J. Grimm, and L. Simpson, "Anatomy-Based Inverse Planning Simulated Annealing Optimization in High-Dose-Rate Prostate Brachytherapy: Significant Dosimetric Advantage Over Other Optimization Techniques," *International Journal of Radiation Oncology*Biology*Physics*, vol. 72, no. 3, pp. 820–827, 11 2008. [Online]. Available: https://www.sciencedirect.com/science/article/pii/S0360301608002836

[136] S. Kirkpatrick, C. D. Gelatt, and M. P. Vecchi, "Optimization by Simulated Annealing," *Science*, vol. 220, no. 4598, pp. 671–680, 5 1983. [Online]. Available: http://www.ncbi.nlm.nih.gov/pubmed/17813860http://www.ncbi.nlm.nih.gov/pubmed/17813860

[137] K. D Dewitt, I.-C. Hsu, J. Speight, V. Weinberg, E. Lessard, and J. Pouliot, "3D inverse treatment planning for the tandem and ovoid applicator in cervical cancer," *International journal of radiation oncology, biology, physics*, vol. 63, pp. 1270–1274, 2005.

[138] M.-C. L. et Frédéric Lacroix, "Dosimétries 3D et évaluation de plans de traitement Dosimétries 3D et évaluation de plans de traitement Dosim," 2016.

[139] S. F. O'Rourke, H. McAneney, and T. Hillen, "Linear quadratic and tumour control probability modelling in external beam radiotherapy," pp. 799–817, 4 2009. [Online]. Available: http://link.springer.com/10.1007/s00285-008-0222-y

[140] E. D. Podgorsak and International Atomic Energy Agency., *Radiation oncology physics : a handbook for teachers and students.* International Atomic Energy Agency, 2005.

[141] T. S. Kehwar, S. F. Akber, and K. Passi, "Qualitative Dosimetric and Radiobiological Evaluation of High-Dose-Rate Interstitial brachytherapy Implants," Tech. Rep. 1, 2008. [Online]. Available: www.medsci.org

[142] C. B. Saw and N. Suntharalingam, "CONCEPT OF DOSE NONUNIFORMITY IN INTERSTITIAL BRACHYTHERAPY," Tech. Rep., 1993. [Online]. Available: https://ac-els-cdn-com.acces.bibl.ulaval.ca/036030169390971W/1-s2.0-036030169390971W-main.pdf?_tid=044d5615-fad1-4989-bde4-0b810256544e&acdnat=1548015072_7299f77a82be8a7b2cc8168b6f4758c0

[143] "Androgen-Deprivation Therapy and Radiation Therapy in Treating Patients With Prostate Cancer - Full Text View - ClinicalTrials.gov." [Online]. Available: https://clinicaltrials.gov/ct2/show/NCT01368588

[144] Y. Yu, J. B. Zhang, G. Cheng, M. C. Schell, and P. Okunieff, "Multi-objective optimization in radiotherapy: applications to stereotactic radiosurgery and prostate brachytherapy," *Artificial Intelligence in Medicine*, vol. 19, no. 1, pp. 39–51, 2000. [Online]. Available: http://www.sciencedirect.com/science/article/pii/S0933365799000494

[145] N. Milickovic, M. Lahanas, M. Papagiannopoulou, N. Zamboglou, and D. Baltas, "Multiobjective anatomy-based dose optimization for {HDR}-brachytherapy with constraint free deterministic algorithms," *Physics in Medicine and Biology*, vol. 47, no. 13, pp. 2263–2280, 6 2002. [Online]. Available: https://doi.org/10.1088%2F0031-9155%2F47%2F13%2F306

[146] S. C. Kumbhakar and C. A. K. Lovell, *Stochastic Frontier Analysis*, ser. Stochastic Frontier Analysis. Cambridge University Press, 2003. [Online]. Available: https://books.google.ca/books?id=wrKDztxLWZ8C

[147] F. Sufian, "The efficiency of Islamic banking industry in Malaysia," *Humanomics: The International Journal of Systems and Ethics*, vol. 23, pp. 174–192, 2007.

[148] N. A. NA, S. N. Durlauf, and L. E. Blume, *The New Palgrave Dictionary of Economics*. Palgrave Macmillan UK, 2016. [Online]. Available: https://books.google.ca/books?id=EO40DAAAQBAJ

[149] F. R. Førsund, C. Lovell, and P. Schmidt, "A survey of frontier production functions and of their relationship to efficiency measurement," *Journal of Econometrics*, vol. 13, no. 1, pp. 5–25, 1980. [Online]. Available: http://www.sciencedirect.com/science/article/pii/0304407680900408

[150] A. Kroshko, O. Morin, and L. Archambault, "Stochastic frontier analysis as knowledge-based model to improve sparing of organs-at-risk for {VMAT}-treated prostate cancer," *Physics in Medicine & Biology*, vol. 64, no. 8, p. 85007, 4 2019. [Online]. Available: https://doi.org/10.1088%2F1361-6560%2Fab0b4d

[151] P. Edimo, A. Kroshko, L. Beaulieu, and L. Archambault, "A stochastic frontier analysis for enhanced treatment quality of high-dose-rate brachytherapy plans," *Physics in Medicine & Biology*, vol. 64, no. 6, p. 65012, 3 2019. [Online]. Available: https://doi.org/10.1088%2F1361-6560%2Fab0522

[152] R Core Team, "R: A Language and Environment for Statistical Computing," Vienna, Austria, 2013. [Online]. Available: http://www.r-project.org/

[153] Yang Xiang, S. Gubian, B. Suomela, and J. Hoeng, "Generalized Simulated Annealing for Efficient Global Optimization: the {GenSA} Package for {R}." *The R Journal Volume 5/1, June 2013*, 2013. [Online]. Available: https://journal.r-project.org/archive/2013/RJ-2013-002/index.html

[154] E. Zivot, *Statistics and Finance: An Introduction*, ser. Springer Texts in Statistics. Springer, 2006, vol. 101, no. 474. [Online]. Available: https://books.google.ca/books?id=DFJg_3PJ5ToC

[155] S. S. Wilks, "The Large-Sample Distribution of the Likelihood Ratio for Testing Composite Hypotheses," *Ann. Math. Statist.*, vol. 9, no. 1, pp. 60–62, 1938. [Online]. Available: https://doi.org/10.1214/aoms/1177732360

[156] J. Hauke and T. Kossowski, "Comparison of Values of Pearson's and Spearman's Correlation Coefficients on the Same Sets of Data," *Quaestiones Geographicae*, vol. 30, no. 2, 2011. [Online]. Available: https://doi.org/10.2478/v10117-011-0021-1

[157] J. L. Myers and A. A. Well, *Research design and statistical analysis*. Lawrence Erlbaum Associates, 2003. [Online]. Available: https://trove.nla.gov.au/work/6731146?selectedversion=NBD24120857

[158] N. R. Council, *Review of the Environmental Protection Agency 039, State-of-the-Science Evaluation of Nonmonotonic Dose Response Relationships as they Apply to Endocrine Disruptors*. Washington, DC: The National Academies Press, 2014.

[159] "3D Slicer." [Online]. Available: https://www.slicer.org/

[160] Y. Yamada, L. Rogers, D. Jeffrey Demanes, G. Morton, B. Prestidge, J. Pouliot, G. Cohen, M. Zaider, M. Ghilezan, and I.-C. Hsu, "American Brachytherapy Society consensus guidelines for high-dose-rate prostate brachytherapy," *Brachytherapy*, vol. 11, pp. 20–32, 2012.

[161] D. Huttenlocher, W. Rucklidge, and G. Klanderman, "Comparing images using the Hausdorff distance under translation," in *Proceedings 1992 IEEE Computer Society Conference on Computer Vision and Pattern Recognition*, 1992, pp. 654–656. [Online]. Available: http://ieeexplore.ieee.org/document/223209/

[162] D. G. Sim, O. K. Kwon, and R. H. Park, "Object matching algorithms using robust Hausdorff distance measures," *IEEE Transactions on Image Processing*, vol. 8, no. 3, pp. 425–429, 1999. [Online]. Available: http://ieeexplore.ieee.org/document/748897/

[163] F. Uccheddu, M. Servi, R. Furferi, and L. Governi, "Comparison of Mesh Simplification Tools in a 3D Watermarking Framework," 2018, pp. 60–69. [Online]. Available: https://www.researchgate.net/publication/318132863

[164] J. A. M. Cunha, I.-C. Hsu, and J. Pouliot, "Dosimetric equivalence of nonstandard HDR brachytherapy catheter patterns," *Medical Physics*, vol. 36, no. 1, pp. 233–239, 12 2008. [Online]. Available: http://www.ncbi.nlm.nih.gov/pubmed/19235391http://www.ncbi.nlm.nih.gov/pubmed/19235391

[165] A. Holm, "Mathematical Optimization of HDR Brachytherapy," Ph.D. dissertation, 2013. [Online]. Available: www.mai.liu.se

[166] Y. Shiraishi, A. Yorozu, T. Ohashi, K. Toya, S. Seki, K. Yoshida, T. Kaneda, S. Saito, T. Nishiyama, T. Hanada, and N. Shigematsu, "Dose Constraint for Minimizing Grade 2 Rectal Bleeding Following Brachytherapy Combined With External Beam Radiotherapy for Localized Prostate Cancer: Rectal Dose-Volume Histogram Analysis of 457 Patients," *International Journal of Radiation Oncology*Biology*Physics*, vol. 81, no. 3, pp. e127–e133, 11 2011. [Online]. Available: https://www.sciencedirect.com/science/article/pii/S0360301611000630

[167] B. Kragelj, J. Zlatic, and L. Zaletel-Kragelj, "Avoidance of late rectal toxicity after high-dose-rate brachytherapy boost treatment for prostate cancer," *Brachytherapy*, vol. 16, no. 1, pp. 193–200, 1 2017. [Online]. Available: http://www.ncbi.nlm.nih.gov/pubmed/27908678http://www.ncbi.nlm.nih.gov/pubmed/27908678

[168] P. Serra, A. F. Stanton, S. Kais, and R. E. Bleil, "Comparison study of pivot methods for global optimization," *The Journal of Chemical Physics*, vol. 106, no. 17, pp. 7170–7177, 5 1997. [Online]. Available: http://aip.scitation.org/doi/10.1063/1.473678

[169] A. H. Hartmann and H. Rieger, *Optimization Algorithms in Physics*. Weinheim, FRG: Wiley-VCH Verlag GmbH & Co. KGaA, 11 2001. [Online]. Available: http://doi.wiley.com/10.1002/3527600876

[170] G. B. L. Carlos A. Coello Coello, *Applications of Multi-objective Evolutionary Algorithms*, ser. Advances in natural computation. World Scientific, 2004. [Online]. Available: http://link.springer.com/10.1134/S0020441212020042

[171] P. M. Pardalos and H. E. Romeijn, *Handbook of Optimization in Medicine*, ser. Springer Optimization and Its Applications. Springer US, 2009, vol. 26. [Online]. Available: http://link.springer.com/10.1007/b100322

[172] C. Cotrutz, M. Lahanas, C. Kappas, and D. Baltas, "A multiobjective gradient-based dose optimization algorithm for external beam conformal radiotherapy," *Physics in Medicine and Biology*, vol. 46, no. 8, pp. 2161–2175, 8 2001. [Online]. Available: http://stacks.iop.org/0031-9155/46/i=8/a=309?key=crossref.826e2da847d2dbb407a03bdaa7c0d8c3

[173] C. M. Fonseca and P. J. Fleming, "An Overview of Evolutionary Algorithms in Multiobjective Optimization," *Evolutionary Computation*, vol. 3, no. 1, pp. 1–16, 3 1995. [Online]. Available: http://www.mitpressjournals.org/doi/10.1162/evco.1995.3.1.1

[174] R. Storn and K. Price, "Differential Evolution - A Simple and Efficient Heuristic for Global Optimization over Continuous Spaces," *Journal of Global Optimization*, vol. 11, no. 4, pp. 341–359, 1997.

[175] J. H. Holland, *Adaptation in natural and artificial systems: an introductory analysis*. Cambridge, MA, USA: MIT Press, 1975.

[176] C. M. Anderson-Cook, "Practical Genetic Algorithms," *Journal of the American Statistical Association*, vol. 100, no. 471, p. 1099, 2005. [Online]. Available: https://doi.org/10.1198/jasa.2005.s45

[177] P. J. M. van Laarhoven and E. H. L. Aarts, "Simulated annealing," in *Simulated Annealing: Theory and Applications*. Dordrecht: Springer Netherlands, 1987, pp. 7–15. [Online]. Available: http://link.springer.com/10.1007/978-94-015-7744-1_2

[178] A. SUPPAPITNARM, K. A. SEFFEN, G. T. PARKS, and P. J. CLARKSON, "A SIMULATED ANNEALING ALGORITHM FOR MULTIOBJECTIVE OPTIMIZATION," *Engineering Optimization*, vol. 33, no. 1, pp. 59–85, 11 2000. [Online]. Available: http://www.tandfonline.com/doi/abs/10.1080/03052150008940911

[179] B. Suman and P. Kumar, "A survey of simulated annealing as a tool for single and multiobjective optimization," *Journal of the Operational Research Society*, vol. 57, no. 10, pp. 1143–1160, 10 2006. [Online]. Available: https://www.tandfonline.com/doi/full/10.1057/palgrave.jors.2602068

[180] C. Tsallis and D. A. Stariolo, "Generalized simulated annealing," *Physica A: Statistical Mechanics and its Applications*, vol. 233, no. 1, pp. 395–406, 1996. [Online]. Available: http://www.sciencedirect.com/science/article/pii/S0378437196002713

[181] R Core Team, "R: A Language and Environment for Statistical Computing," Vienna, Austria, 2013. [Online]. Available: http://www.r-project.org/

[182] Xiang and Gong, "Efficiency of generalized simulated annealing," *Physical review. E, Statistical physics, plasmas, fluids, and related interdisciplinary topics*, vol. 62, no. 3 Pt B, pp. 4473–6, 9 2000. [Online]. Available: http://www.ncbi.nlm.nih.gov/pubmed/11088992

[183] Y. Xiang, D. Y. Sun, and X. G. Gong, "Generalized Simulated Annealing Studies on Structures and Properties of Nin (n = 255) Clusters," *The Journal of Physical Chemistry A*, vol. 104, no. 12, pp. 2746–2751, 2000. [Online]. Available: https://doi.org/10.1021/jp992923q

[184] RStudio Team, "RStudio: Integrated Development Environment for R," Boston, MA, 2015. [Online]. Available: http://www.rstudio.com/

[185] "Introduction to dnorm, pnorm, qnorm, and rnorm for new biostatisticians," 2018. [Online]. Available: http://seankross.com/notes/dpqr/

[186] "Spearman Rank Correlation," 2018. [Online]. Available: https://rpubs.com/aaronsc32/spearman-rank-correlation

[187] S. Katayama, "Power of Brute-force Search in Strongly-typed Inductive Functional Programming Automation," in *Proceedings of the 8th Pacific Rim International Conference on Trends in Artificial Intelligence*, ser. PRICAI'04. Berlin, Heidelberg: Springer-Verlag, 2004, pp. 75–84. [Online]. Available: https://doi.org/10.1007/978-3-540-28633-2_10

[188] S. Weston and R. Calaway, "Getting Started with doParallel and foreach," Tech. Rep., 2018. [Online]. Available: https://cran.r-project.org/web/packages/doParallel/vignettes/gettingstartedParallel.pdf

[189] S. Rylander, S. Buus, L. Bentzen, E. M. Pedersen, and K. Tanderup, "The influence of a rectal ultrasound probe on the separation between prostate and rectum in high-dose-rate brachytherapy," *Brachytherapy*, vol. 14, no. 5, pp. 711–717, 9 2015. [Online]. Available: http://www.ncbi.nlm.nih.gov/pubmed/26164752http://www.ncbi.nlm.nih.gov/pubmed/26164752

[190] "Automated parameter selection for {LOESS} regression," 2016. [Online]. Available: https://www.r-bloggers.com/automated-parameter-selection-for-loess-regression/

[191] S. Weston, "Using The foreach Package," 2017.

[192] S. Weston and R. Calaway, "Getting Started with doParallel and foreach," 2017.